

PITTING CORROSION OF AA1050 SHEETS PRODUCED BY DC CASTING AND
TWIN-ROLL CASTING TECHNIQUES



by
Berk Hakkı Gazioğlu

Submitted to Graduate School of Natural and Applied Sciences
in Partial Fulfillment of the Requirements
for the Degree of Master of Science in
Chemical Engineering

Yeditepe University
2019

PITTING CORROSION OF AA1050 SHEETS PRODUCED BY DC CASTING AND
TWIN-ROLL CASTING TECHNIQUES

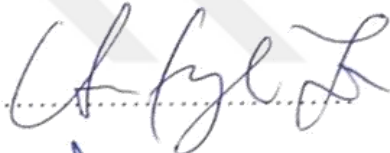
APPROVED BY:

Assist. Prof. Dr. Levent Organ
(Thesis Supervisor)
(Yeditepe University)



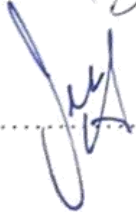
.....

Assoc. Prof. Dr. Ahmet Yilmaz
(Yalova University)



.....

Assist. Prof. Dr. Cem Levent Altan
(Yeditepe University)



.....

DATE OF APPROVAL:/...../2019

ACKNOWLEDGEMENTS

Firstly, I would like to introduce my sincere gratitude to my advisor Assist. Prof. Levent Organ. The door to Assist. Prof. Levent Organ office was always open whenever I ran into a trouble spot or had a question about my research or writing. I feel so lucky to have an opportunity to study with him and with his project. It is a pleasure to being a part of his team was a pleasure for me.

Also, I would like to thank to my instructors in Yeditepe University, Assoc. Prof. Dr. Tuğba Davran Candan, Assist. Prof. Dr. Cem Levent Altan, Assist. Prof. Dr . Oluş Özbek and Assoc. Prof. Dr. Erde Can for their guidance throughout my education.

I would like to thank The Scientific and Technical Council of Turkey (TUBITAK) for their support of this study under the research grant no: 315M232. The help of TUBITAK Marmara Research Center (TUBITAK-MAM) in examination of microstructures and examination of surfaces after immersion tests is acknowledged. The help of Erzurum Technical University in optical profilometry examinations is acknowledged.

In addition, I would like to thank my colleague and best friend precious Öykü Gizem Zaloğlu for her friendship and helping during the process. Besides, I'm deeply thankful to İlayda Acaroğlu Degitz, Sera Erkeçoğlu, Şelale Gülyuva and Nur Çınar for their friendship during this period. I have been so lucky to have them by my side during the whole period.

Finally, I must express my very profound gratitude to my parents and to my best friends Cansu Ünal, Akgül Öneri and Nazlı Deniz Ayyıldız for providing me with unfailing support and continuous encouragement throughout my years of study and through the process of researching and writing this thesis. This accomplishment would not have been possible without them.

ABSTRACT

PITTING CORROSION OF AA1050 SHEETS PRODUCED BY DC CASTING AND TWIN-ROLL CASTING TECHNIQUES

Aluminum alloy 1050 (AA1050) sheets produced by direct-chill casting (DCC) and hot-rolling process and the same alloy produced by the twin-roll casting (TRC) are compared for their susceptibility to pitting corrosion in this study. To determine any differences between the pitting susceptibility of the DCC and TRC alloys, electrochemical experiments were conducted in deaerated and naturally aerated NaCl solutions with different concentrations (1 M to 0.001 M). The experiments were cyclic potential polarization (CPP) measurements, potentiostatic tests for the repassivation potential determination (E_{repass}), galvanostatic cyclic polarization (GSCP) measurements, metastable pitting measurements under potentiostatic conditions and electrochemical noise measurements. Furthermore, immersion tests were performed in 0.01 M NaCl for 7 days.

The microstructure investigations showed that larger intermetallics were present in the DCC alloy, while the number of intermetallics in the TRC alloy was larger. The particles contained Al, Fe and Si in both alloys. The pitting potentials (E_{pit}) from the CPP experiments were generally more positive for the DCC alloy sheets than TRC alloy sheet. However, the differences between the two production techniques were found to be less than 30 mV. The results from E_{repass} potentials determined under potentiostatic condition revealed that the highest difference between the two production techniques was 50 mV and the DCC alloys have more positive potentials. Breakdown (E_b) potentials as well as the protection potentials (E_{prot}) for the DCC and TRC alloys were found to be close to each other according to the GSCP technique. At 0.01 M concentration, the formation rate of metastable pits in the AA1050 sheet produced by the DCC was found to be higher than that of the AA1050 sheet produced by the TRC. The change in localized corrosion activity of the alloys over time was measured by electrochemical noise measurements. The SEM and optic profilometry investigations after immersion tests showed that pits of larger diameter formed in the AA1050 DCC alloy.

ÖZET

DC DÖKÜMÜ VE İKİZ MERDANE DÖKÜM TEKNİKLERİ İLE ÜRETİLEN AA1050 LEVHASININ ÇUKURLAŞMA KOROZYONU

Bu çalışmada, direk soğuk döküm (DCC) ve sıcak haddeleme işlemi ile üretilen alüminyum alaşımlı 1050 (AA1050) levhaları ve ikiz merdane döküm (TRC) tarafından üretilen aynı alaşım çukur korozyonuna karşı duyarlılıkları açısından karşılaştırılmıştır. DCC ve TRC alaşımlarının çukurcuk korozyonuna karşı duyarlılığı belirlemek için, farklı konsantrasyonlarda (1 M ila 0.001 M) havalandırılmış ve doğal olarak havalandırılmış NaCl çözeltilerinde elektrokimyasal deneyler yapıldı. Levhaların çukurlaşma korozyon dirençlerini ölçmek için, çevrimsel potansiyel polarizasyon (CPP) ölçümlerini, yeniden pasivasyon potansiyelinin belirlenmesi için potansiyostatik (E_{repas}) testler, çevrimsel galvanostatik polarizasyonu (GSCP) ölçümleri, potansiyostatik koşullar altında yarı kararlı çukurcuk ölçümleri ve elektrokimyasal gürültü ölçümleridir. Ayrıca, daldırma testleri 7 gün boyunca 0.01 M NaCl içerisinde gerçekleştirildi.

Mikroyapı araştırmaları, DCC alaşımında daha büyük intermetaliklerin bulunduğunu, TRC alaşımında intermetaliklerin sayısının daha büyük olduğunu gösterdi. Parçacıklar her iki alaşımında Al, Fe ve Si içermektedir. CPP deneylerinden elde edilen çukurluk potansiyelleri (E_{pit}), DCC alaşımlı levhalar için genellikle TRC alaşımlı levhadan daha pozitif olarak bulunmuştur. Ancak, iki üretim tekniği arasındaki farkın 30 mV'den az olduğu bulundu. Potansiyostatik şartlar altında belirlenen E_{repas} potansiyellerinden elde edilen sonuçlar, iki üretim tekniği arasındaki en yüksek farkın 50 mV olduğunu ve DCC alaşımlarının daha pozitif potansiyellere sahip olduğunu ortaya koymaktadır. Arıza (E_b) potansiyellerinin yanı sıra DCC ve TRC alaşımları için koruma potansiyellerinin (E_{prot}) GSCP tekniğine göre birbirine yakın olduğu bulunmuştur. 0.01 M konsantrasyonunda, DCC tarafından üretilen AA1050 levhalarında yarı kararlı çukurcukların oluşum oranının TRC tarafından üretilen AA1050 levhalarına göre daha yüksek olduğu bulunmuştur. Alaşımların lokal korozyon aktivitesindeki zamana karşı değişimi elektrokimyasal gürültü ölçümleri ile ölçülmüştür. Daldırma testlerinden sonra SEM ve optik profilometri incelemeleri, AA1050 DCC alaşımında daha büyük çaplı çukurların oluştuğunu göstermiştir.

TABLE OF CONTENTS

ACKNOWLEDGEMENTS.....	iii
ABSTRACT.....	iv
ÖZET	v
LIST OF FIGURES	ix
LIST OF TABLES.....	xiii
LIST OF SYMBOLS AND ABBREVIATIONS	xv
1. INTRODUCTION.....	1
2. THEORETICAL BACKGROUND	2
2.1. CORROSION BASICS.....	2
2.1.1. Reactions of Corrosion	2
2.2. THERMODYNAMICS OF CORROSION	4
2.2.1. Gibbs Free Energy	4
2.2.2. Standard Electrode Potential.....	4
2.2.3. Nernst Equation	5
2.2.4. Reference Electrode	6
2.2.5. Potential / pH (Pourbaix) Diagrams.....	6
2.3. KINETICS OF CORROSION	9
2.3.1. Electrochemical Polarization	9
2.3.2. Solution Resistance (R_u)	11
2.4. TYPES OF CORROSION	13
2.5. PASSIVITY AND LOCALIZED CORROSION	14
2.5.1. Passivity	14
2.5.2. Localized Corrosion.....	15
2.6. PITTING CORROSION	16
2.7. ALUMINUM AND ITS ALLOYS	17
2.8. PRODUCTION METHODS OF ALUMINUM AND ITS ALLOYS.....	18
2.8.1. Direct Chill Casting (DCC)	18
2.8.2. Twin Roll Casting (TRC)	20
2.8.3. Differences between DCC and TRC Sheet Production Techniques.....	20

2.9. LITERATURE SURVEY OF PITTING CORROSION OF ALUMINUM ALLOYS	22
3. MATERIALS AND CHEMICALS	27
3.1. MATERIALS	27
3.2. CHEMICALS	29
4. METHODOLOGY	30
4.1. ELECTROCHEMICAL SYSTEM	30
4.1.1. Working Electrode	30
4.1.1.1. Sample Preparation and Polishing Procedure	31
4.1.2. Counter Electrode	32
4.1.3. Reference Electrode	33
4.2. ELECTROCHEMICAL TEST	34
4.2.1. Microstructure Investigations	36
4.2.2. Open Circuit Potential (OCP)	36
4.2.3. Cyclic Potential Polarization Measurements	37
4.2.4. Potentiostatic Determination of the Repassivation Potential (E_{repass})	37
4.2.5. Galvanostaircase Cyclic Polarization (GSCP)	38
4.2.6. Metastable Pitting	39
4.2.7. Electrochemical Noise Measurement (ECN)	39
4.2.8. Immersion Tests	40
5. RESULTS AND DISCUSSION	42
5.1. RESULTS OF MICROSTRUCTURE INVESTIGATIONS	42
5.2. RESULTS OF OPEN CIRCUIT POTENTIAL MEASUREMENTS (OCP)	44
5.3. RESULTS OF CYCLIC POTENTIAL POLARIZATION MEASUREMENTS	47
5.4. RESULTS OF POTENTIOSTATIC DETERMINATION OF THE REPASSIVATION POTENTIAL MEASUREMENTS	61
5.5. RESULTS OF GALVANOSTAIRCASE CYCLIC POLARIZATION MEASUREMENT	73
5.6. RESULTS OF METASTABLE PITTING MEASUREMENTS	79
5.7. RESULTS OF ELECTROCHEMICAL NOISE MEASUREMENT	90
5.8. RESULTS OF IMMERSION TESTS	99

6. CONCLUSION 103

REFERENCES 106

APPENDIX A 115

APPENDIX B 119

APPENDIX C 129



LIST OF FIGURES

Figure 2.1. Representative schema of the corrosion of specific metal in a acid medium.....	2
Figure 2.2. Schematic Pourbaix diagram for the aluminium-water system.....	7
Figure 2.3. Schematic Pourbaix diagram of aluminum with four concentrations of soluble species (25°C) [6].....	8
Figure 2.4. Evans diagrams for metal oxidation and hydrogen ion reduction.....	10
Figure 2.5. A schematic polarization experiment.....	11
Figure 2.6. Three electrode polarization cell.....	12
Figure 2.7. Anodic polarization curve of a metal with passivation property. The abbreviations in the graph represents the E_{cor} - corrosion potential, i_p - passive current density, i_{cc} - critical current density and E_{pp} - passivation potential.....	14
Figure 2.8. The cross-sectional views of the different types of pits [2].....	16
Figure 2.9. Schematic representation of pitting event.....	17
Figure 2.10. Direct-chill ingot casting.....	19
Figure 2.11. Schematic representation of Twin roll casting.....	20
Figure 4.1. The representative image of AA in a mold and image of working electrode....	31
Figure 4.2. Working electrodes with different surface areas. A hole was punched on the electroplating tape to obtain the desired test surface area.	32
Figure 4.3. Pt mesh counter electrode and SCE Reference electrode that are used in electrochemical experiments.....	33
Figure 4. 4. Electrochemical polarization cell (Biologic Flat Cell).....	34
Figure 4. 5. Electrochemical polarization cell for noise measurement. One of the working electrodes.....	35

Figure 4.6. Representative Biologic potentiostat/galvanostat device	35
Figure 5.1. Microscope images of AA1050 alloys after etching with HF	42
Figure 5.2. SEM images of AA1050 alloys after etching with HF	43
Figure 5.3. EDS analysis of intermetallics for AA1050	44
Figure 5.4. Open circuit potential results.....	46
Figure 5.5. Representative pitting potential, repassivation potential and passive current determination for AA1050 TRC in 0.1 M NaCl	49
Figure 5.6. Cyclic polarization measurement results for 4 samples of AA1050 in 1 M NaCl solution. The arrows show the sweep direction.	50
Figure 5.7. Cyclic polarization measurement results for 4 samples of AA1050 in 0.1 M NaCl solution. The arrows show the sweep direction.	51
Figure 5.8. Cyclic polarization measurement results for 4 samples of AA1050 in 0.01 M NaCl solution. The arrows show the sweep direction.	52
Figure 5.9. Cyclic polarization measurement results for 4 samples for AA1050 in 0.001 M NaCl solution. The arrows show the sweep direction	53
Figure 5.10. Normal distribution graph of E_{pit} data for AA1050 in 1 M, 0.1 M, 0.01 M and 0.001 M NaCl Solution.....	56
Figure 5.11. Relationship between the pitting potentials and the Cl^- concentration	57
Figure 5.12. Optic microscope images after CPP experiments in 1 M solution.....	59
Figure 5.13. The tape boundary images at 50x and white corrosion product after full CPP experiments at 500x	60
Figure 5.14. The tape boundry images at 50x and surface images after CPP cut experiments at 500x.....	60
Figure 5.15. Optical examination of pits at the activation potential for AA1050 DCC alloys at 1 M (Magnification X1000).....	62

Figure 5.16. Potentiostatic determination of E_{repas} plots for DCC alloy in 1 M NaCl (Potential is corrected for potential drop in solution).....	63
Figure 5.17. Potentiostatic determination of E_{repas} current density versus time plots for AA1050 DCC alloy in 1 M NaCl solution	65
Figure 5.18. Potentiostatic determination of E_{repas} current density versus time plots in 1 M NaCl solution	66
Figure 5.19. Potentiostatic determination of E_{repas} current density versus time plots in 0.1 M NaCl solution.....	67
Figure 5.20. Potentiostatic determination of E_{repas} current density versus time plots in 0.01 M NaCl solution.....	68
Figure 5.21. Current density versus potential graphs for DCC and TRC alloys at various concentration.....	71
Figure 5.22. GSCP graphs for the DCC alloy and the TRC alloy in 1 M NaCl solution	74
Figure 5.23. GSCP graphs for the DCC alloy and the TRC alloy in 0.1 M NaCl solution .	75
Figure 5.24. GSCP graphs for the DCC alloy and the TRC alloy in 0.01 M NaCl solution	76
Figure 5.25. Comparison of critical potential determined by the different method	78
Figure 5.26. Metastable pitting graphs for DCC alloys at 0.01M NaCl test solution.....	82
Figure 5.27. Metastable pitting graphs for TRC alloys at 0.01M NaCl test solution	84
Figure 5.28. Metastable pitting graphs for DCC alloys at 0.001M NaCl test solution.....	85
Figure 5. 29. Metastable pitting graphs for TRC alloys at 0.001M NaCl test solution	87
Figure 5.30. Metastable pitting rate for DCC and TRC alloys as a function of potential below E_{pit}	88
Figure 5.31. Average total charge for DCC and TRC alloys as a function of potential below E_{pit}	90

Figure 5.32. Current and potential results of 3 h ZRA measurement 10 minutes after immersion at 0.1 M NaCl solution DCC and TRC respectively	92
Figure 5.33. Current and potential results of 24 h OCP + 30 min. ZRA measurement at 0.1 M for DCC and TRC respectively	93
Figure 5.34. Current and potential results of 3 h. ZRA measurement 10 minutes after immersion at 0.01 M NaCl solution DCC and TRC respectively	94
Figure 5.35. Current and potential results of 24 h. OCP + 30 min. ZRA measurement at 0.01 M for DCC and TRC respectively	95
Figure 5.36. Current PSD results at 5000-6000 sec for DCC alloy and 9800-10800 sec for TRC alloy at 0.1 M for 3 sec. OCP + 3 h. ZRA measurement	98
Figure 5.37. Current PSD results at 5000-6000 sec for DCC alloy and 9800-10800 sec for TRC alloy at 0.01 M for 3 sec. OCP + 3 h. ZRA measurement	98
Figure 5.38. SEM images of the surfaces of AA1050 which have been immersed for 7 days in 0.01 M NaCl solution.	101
Figure 5.39. Optic profilometer images of the surfaces of AA1050 which have been immersed for 7 days in 0.01 M NaCl solution.....	102

LIST OF TABLES

Table 1.1. Aluminum alloy naming chart [11]	18
Table 3.1. Detailed specifications of materials that are used in this study	27
Table 3.2. Detailed specifications of devices that are used in this study.....	28
Table 3.3. Name, molecular formula, and supplier of each chemical and solvent used in this study.....	29
Table 4.1. Elemental composition of AA1050 DCC and TRC samples in wt percent.....	30
Table 5.1. Size and number of intermetallic in alloys obtained from the analysis of optical photographs.....	43
Table 5.2. Calculated average pitting potential and standard deviation value for AA1050 DCC/TRC	54
Table 5.3. Calculated repassivation potentials for AA1050 DCC and TRC alloys.....	57
Table 5.4. Calculated passive current density and standard deviation value for AA1050 DCC/TRC	58
Table 5.5. Activation potentials for experiments for determination of repassivation potentials in different NaCl solutions.....	63
Table 5.6. Repassivation potential range over concentration data for AA1050 DCC and TRC samples.....	69
Table 5.7. Result table for analysis of controlled alloys after repassivation measurements	72
Table 5.8. Breakdown (E_b) and protection (E_{prot}) potentials for DCC and TRC alloys from GSCP experiments with different NaCl concentrations	77
Table 5.9. Result table for analysis of controlled alloys after CPP measurements	79
Table 5.10. The pitting potential and the applied potential for metastable pitting experiments	80

Table 5.11. Average metastable pitting rate results for DCC and TRC alloys..... 88

Table 5.12. Average total charge results for DCC and TRC alloys..... 89

Table 5.13. The slope of the current PSD graphs at 0.1 M and 0.01 M test solution..... 99



LIST OF SYMBOLS/ABBREVIATIONS

a	Activity of the substance
AA	Aluminum alloy
CE	Counter electrode
CPP	Cyclic potential polarization
DCC	Direct chill casting
E_{act}	Actual potential
E°_{anode}	Anodic standard cell potential
E_b	Breakdown potential
$E^{\circ}_{\text{cathode}}$	Cathodic standard cell potential
E_{cell}	Cell potential
E°_{cell}	Standard cell potential
ECN	Electrochemical noise
E_{cor}	Corrosion potential
E_{pit}	Pitting potential
E_{prot}	Protection potential
E_{ptp}	Pit transition potential
E_{repass}	Repassivation potential
E_{soln}	Solution potential
F	Faraday constant
FFT	Fast fourier transform
GSCP	Galvanostaircase polarization
i	Current density
i_{app}	Applied current
i_{corr}	Corrosion current density
i_{pas}	Passive current density
MEM	Maximum entropy method
n	The numbers of electrons exchanged
n	The number of moles
OCP	Open circuit potential

PSD	Power spectral density
Q	Reaction quotient
R	Ideal gas constant
RE	Reference electrode
R_{soln}	Solution resistance
SCE	Saturated calomel electrode
SEM	Scanning electron microscopy
SEM EDS	Scanning electron microscopy-energy dispersive spectroscopy
SHE	Standard hydrogen electrode
T	Temperature
TRC	Twin-roll casting
WE	Working electrode
ZRA	Zero resistance ammeter
ΔG	Gibbs free energy change

1. INTRODUCTION

The demand for metals and alloys which are lightweight and have high mechanical properties is always high. Aluminum and its alloys are one of these metals, which are gaining increasing importance in engineering materials. This is mainly due to their low density, light weight, easy formability, high strength/weight ratio and corrosion resistance. It has one third of the density of steel and, when used instead of steel, could provide a reduction in weight of about 50 percent. Thus, aluminum alloys are widely used in different sectors including the chemical industry.

Conventionally, the aluminum alloys sheets are produced by the so called direct chill casting (DCC) followed by hot rolling. An alternative way of aluminum alloy sheet production that has become popular is the twin roll casting (TRC) technique. It offers the lower capital investment, lower space requirement. However, not all alloys of the DCC route can be produced by the TRC technique. Only alloys with lower solidification range can be produced by the TRC technique.

It is also know that the microstructures of the aluminum alloy sheets produced by the two techniques are different. But microstructure can affect the susceptibility of an alloy to localized corrosion. Thus, the aim of this study is to compare the susceptibility to pitting corrosion of AA1050 sheet produced by the DCC route with that produced with the TRC route.

This thesis is organized as follows. First, a theoretical background is presented. In this section, corrosion, its thermodynamics and kinetics, passivity and localized corrosion are briefly explained. Also, the aluminum alloys and the two production techniques are explained. This is followed by a literature survey of the pitting corrosion of the aluminum alloys. In the next section, experimental details are presented. Results of the experiments and their discussions are then presented. Finally, conclusions and future work are given.

2. THEORETICAL BACKGROUND

2.1. CORROSION BASICS

Corrosion is the loss of the useful properties of a material as a result of chemical or electrochemical reaction with its environment. In other words, the corrosion is destructive and unintentional degradation of a material caused by its environment. The reason for corrosion being so common can be seen from the chemistry of metals. Most metals are more stable as compounds than as a pure metal. They have a driving force to move from a higher energy state to a lower energy state [1].

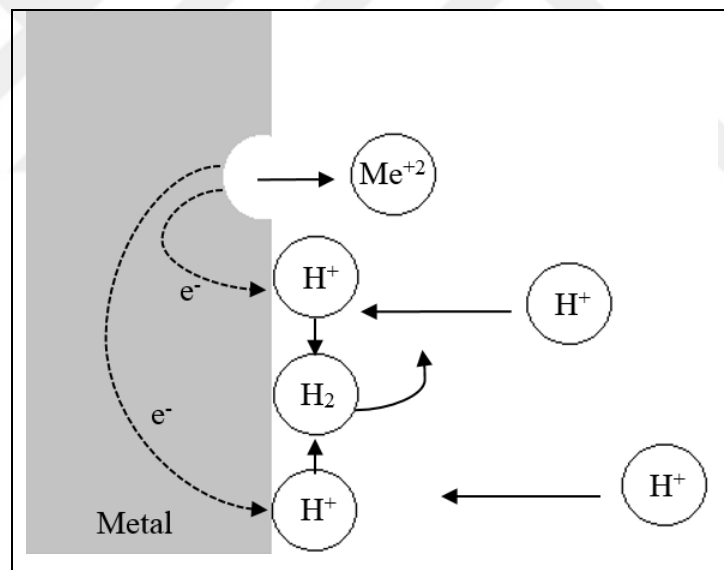
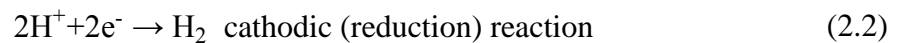
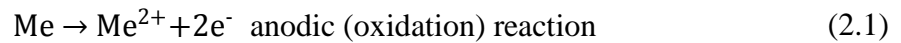


Figure 2.1. Representative schema of the corrosion of specific metal in an acid medium

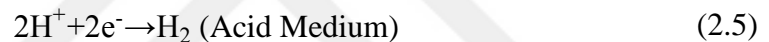
2.1.1. Reactions of Corrosion

During corrosion in an aqueous medium, an anodic (electron loss) reaction and a cathodic (electron gain) reaction occur at the same time. A simple example is shown in Figure 2.1. Metal is being dissolved in the acidic medium through the anodic reaction. Hydrogen ions are being reduced through the cathodic reaction at the same time, and, hence, consuming the

electrons produced by the anodic reaction. In the anodic reaction, the oxidation state of the metal increases. Anodic reactions are, thus, also called oxidation reactions. Cathodic reactions are also called reduction reactions since the oxidation state of the reactant is reduced [2].



The common reduction reactions of corrosion are the oxygen reduction reaction and the hydrogen evolution reaction. Depending on the aqueous medium, these are written as;



For aluminum corroding in an oxygen containing neutral medium, the anodic and cathodic reactions can be written as follows;



The reaction 2.7 is the anodic reaction and the reaction 2.4 is the cathodic reaction. In absence of oxygen in a neutral medium, the reaction 2.6 can take place instead of the reaction 2.4. The reaction of the aluminum takes place in the form of the oxidation state of aluminum with a zero metal state, the conversion to aluminum with an oxidation state of +3. Electrochemical thermodynamics and kinetics are used to determine the possibility of corrosion and the corrosion rate, respectively. Thermodynamics can be used to understand whether the metal or alloy will corrode under the conditions considered. If corrosion is

possible, kinetics principles can be used to calculate the corrosion rate such as mm per year. Thermodynamics and kinetics of corrosion will be explained briefly in the next sections.

2.2. THERMODYNAMICS OF CORROSION

2.2.1. Gibbs Free Energy

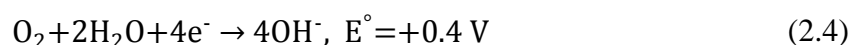
Gibbs free energy is a thermodynamic quantity that predicts whether a process occurs spontaneously at constant pressure and temperature. A chemical reaction can occur spontaneously only when the Gibbs free energy change is negative for the reaction ($\Delta G < 0$). In electrochemistry, Gibbs free energy change for a cell can be expressed as;

$$\Delta G = -nFE_{\text{cell}} \quad (2.8)$$

where ΔG is the Gibbs free energy change, n is the number of electrons exchanged in the reaction, F is the Faraday's constant (96400 C/mol e^-) and E_{cell} is the cell potential. The cell potential is calculated from the half-cell potentials of the anodic and cathodic reactions. If the Gibbs free energy change is less than zero, corrosion reactions (the oxidation of metal and the reduction reaction) will proceed spontaneously. However, the corrosion event cannot occur when the Gibbs free energy change is greater than the zero ($\Delta G > 0$).

2.2.2. Standard Electrode Potential

The standard electrode potential (also called the standard half-cell potential) of a reaction, E° , is the potential that is measured at 25 °C when all the reactants and products are at unit activity. For example,



The standard electrode potential of aluminum oxidation is -1.66 V (reaction 2.7) and the standard electrode potential of oxygen reduction (reaction 2.4) is +0.40 V. The potential can only be measured with respect to a reference. The values above are with respect to the

standard hydrogen electrode (SHE). The standard cell potentials of an electrochemical cell is equal to the difference between the half-cell potentials of cathode and anode [2] [3];

$$E_{\text{Cell}}^{\circ} = E_{\text{cathode}}^{\circ} - E_{\text{anode}}^{\circ} \quad (2.9)$$

The standard reversible cell potential the anodic reaction 2.7 and the cathodic reaction 2.4 is then;

$$E_{\text{Cell}}^{\circ} = +0.40 \text{ V} - (-1.66 \text{ V}) = 2.06 \text{ V vs SHE} \quad (2.10)$$

From Equation 2.8, it can be seen that ΔG° is negative and, therefore, aluminum will dissolve to form Al^{+3} , while O_2 is being reduced, both reactions proceeding spontaneously.

2.2.3. Nernst Equation

Nernst equation is used to calculate the voltage of an electrochemical cell or to find the concentration of any component of the cell. Standard half-cell potentials and the standard cell potentials obtained from these potentials are valid for solutions at 25 °C and unit activities. Nernst equation describes the relationship between the electrode potential and the concentration of medium. If the cell has features other than the non-standard conditions, the Nernst equation is used. An electrochemical reaction can be expressed by the following equation in a general form.



Where l, m, q and r are the stoichiometric coefficient of reaction species L, M, Q and R. Then, the Nernst equation is

$$E_r = E^{\circ} - \frac{RT}{nF} \ln Q \quad (2.12)$$

where E_r is the reversible cell potential under specific conditions (non-standard conditions), E° is reversible cell potential under standard conditions, R is ideal gas constant, T is

temperature, n is number of moles of electrons, F is Faraday constant and Q is the reaction quotient. It is written in terms of activities of the species as follows;

$$Q = \frac{[\text{Oxidation}]}{[\text{Reduction}]} = \frac{a_Q^q \cdot a_R^r}{a_L^l \cdot a_M^m} \quad (2.13)$$

Then;

$$E_r = E^\circ - \frac{RT}{nF} \ln \frac{a_Q^q \cdot a_R^r}{a_L^l \cdot a_M^m} \quad (2.14)$$

All in all, it is not possible to determine the corrosion rate using thermodynamic aspects. Corrosion rate can be determined by examining the reaction kinetics.

2.2.4. Reference Electrode

An ideal reference electrode has a known and constant potential and also it must be completely insensitive to the composition of the solution under study. It should be sturdy and easy to attach to the cell. Therewithal this electrode must maintain a constant potential even if there is a net current in the experimental setup [4]. Reference electrodes can be categorized as calomel, aqueous, non-aqueous and self-constructed [5]. In this study only, a saturated calomel electrode was used. The calomel reference electrode is the electrode which is based on a chemical reactions of the elemental mercury with calomel which is mercury (I) chloride. This reaction occurs in saturated potassium chloride solution. The reference electrode is the key component of an electrochemical cells because it is the only way to measure the potential difference. Calomel reference electrode is more preferable than SHE because it is an electrode type which is easier to use and control.

2.2.5. Potential / pH (Pourbaix) Diagrams

The Pourbaix diagram is a graphical representation of the thermodynamic equilibrium condition of a metal-electrolyte system. In the Pourbaix diagram, the electrode potential of

the metal is shown against the pH of the electrolyte. The oxidation conditions are found by the tops of the diagram and the reduction conditions are depicted by the bottom of the Pourbaix diagram. In the Pourbaix diagram of aluminum, four different elements should be considered.

- 2 solid types: Al and Al_2O_3 and,
- 2 ionic types: Al^{3+} and AlO_2^- that are shown in Figure 2.2.

The stability of the water is given with dash lines in Figure 2.2. Above the dash line “a” the water is decomposed and the oxygen gas is formed. On the other hand, the water is decomposed and hydrogen gas is formed below the dash line “b”. The region between these two lines is called as stability region for water.

The Pourbaix diagram, describe the stable and unstable regions of the metal or its compounds in terms of thermodynamics as a function of the electrode potential and pH value. The first vertical line shows the separating Al^{3+} and AlO_2^- ions at the end of the pH scale at low pH in Figure 2.2.

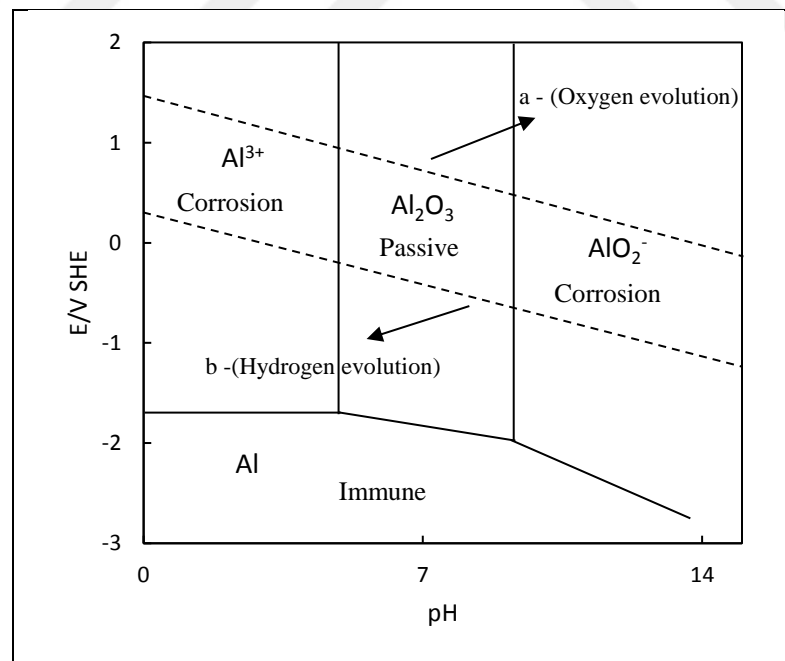


Figure 2.2. Schematic Pourbaix diagram for the Aluminium-water system

Three possible states which are passive region, immune region, and corrosion regions are given for aluminum in Figure 2.2.

- a- Passive Region: The filled areas on the center of the diagram and upper part of the Al_2O_3 is the passive region for aluminum. At this passive region Aluminium surface is coated with oxide film layer which protect the surface of the metal.
- b- Immune Region: At this region, aluminum is corrosion resistant. This is also considered to be completely insensitive to corrosion attack and is reliable to use.
- c- Corrosion Region: The aluminum is stable as an ionic product and therefore it is susceptible to corrosion attack. Aluminium can dissolved and corrosion can occur at this region.

However, the corrosion rate cannot be estimated by using Pourbaix diagram. Because of that the kinetics of corrosion should be used to calculate the rate of corrosion.

A more complete Pourbaix diagram for aluminum is presented in Figure 2.3.

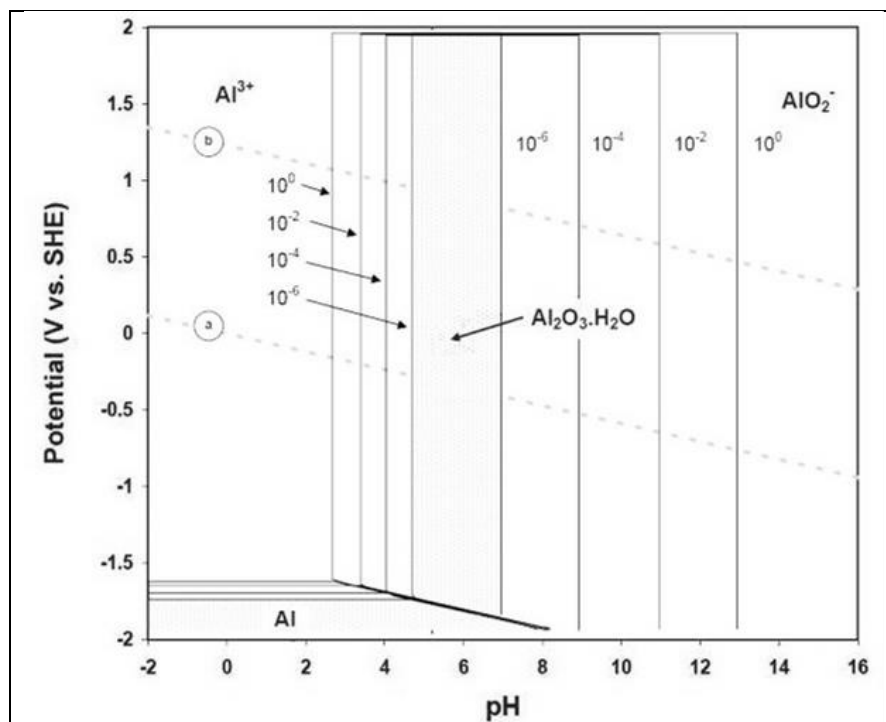


Figure 2.3. Schematic Pourbaix diagram of aluminum with four concentrations of soluble species (25°C) [6]

2.3. KINETICS OF CORROSION

In order to compare the resistance of metals and alloys against corrosion, the corrosion rate of each must be quantified. The uniform corrosion rate can be defined as the rate of dissolution of a substance per unit time. Various methods are used to measure the corrosion rate. These methods can be listed as;

- Mass reduction method
- Electrochemical methods (Tafel Extrapolation Method, Electrochemical Impedance Spectroscopy)

2.3.1. Electrochemical Polarization

Polarization is the potential change $E - E_r$. It is caused by a net surface reaction rate for the half-cell reaction. It is shown as;

$$\eta = E - E_r \quad (2.15)$$

For cathodic polarization, η_c , electrons are supplied to the surface, and a buildup in the metal due to the slow reaction rate causes the surface potential, E , to become negative to E_r . Hence, η_c is negative by definition. For anodic polarization, electrons are removed from the metal, a deficiency results in a positive potential change due to the slow liberation of electrons by the surface reaction, and η_a is positive. Figure 2.4. Under the activation control (that is, charge transfer control), the anodic and cathodic polarizations (or overpotentials) can be expressed as

$$\eta_a = E - E_r = \beta_a \log \frac{i_a}{i_0} \quad (2.16)$$

And

$$\eta_c = E - E_r = \beta_c \log \frac{i_c}{i_0} \quad (2.17)$$

Here, β_a and β_c are anodic and cathodic Tafel slopes, i_a and i_c are anodic and cathodic current densities (that is, reaction rates), and i_o is called the exchange current density. On a semilog graph, an E versus log of current density plot looks as a straight line. Such a kinetic plot is called an Evans diagram. An example is shown in Figure 2.4. In the figure, the anodic polarization line for the metal dissolution and cathodic polarization line for the hydrogen reduction are shown. This would correspond, for instance, a metal corroding in an acidic aqueous solution. According to the mixed potential theory, since both the oxidation and cathodic reactions occur on the metal surface, the metal will acquire a potential called the corrosion potential E_{corr} . The dissolution rate of the metal is given by i_{corr} . i_{corr} can then be used to calculate the uniform corrosion rate with the use of Faraday's law. On the other hand, the kinetic parameters such as exchange current densities and Tafel slopes necessary to plot an Evans diagram and hence calculate the corrosion rate is rarely known with confidence. Thus, electrochemical polarization experiments are commonly performed. An example is shown in Figure 2.5. While an Evans diagram shows the reaction rates as current densities, a polarization curve shows applied current densities ($i_{\text{app}} = i_a - |i_c|$). By extrapolating the linear regions at high and low overpotentials (that is Tafel extrapolation), i_{corr} can be determined.

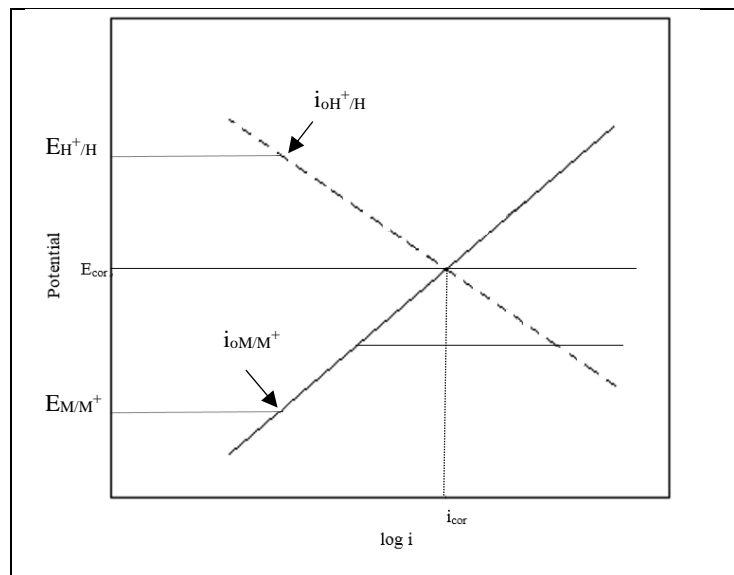


Figure 2.4. Evans diagrams for metal oxidation and hydrogen ion reduction

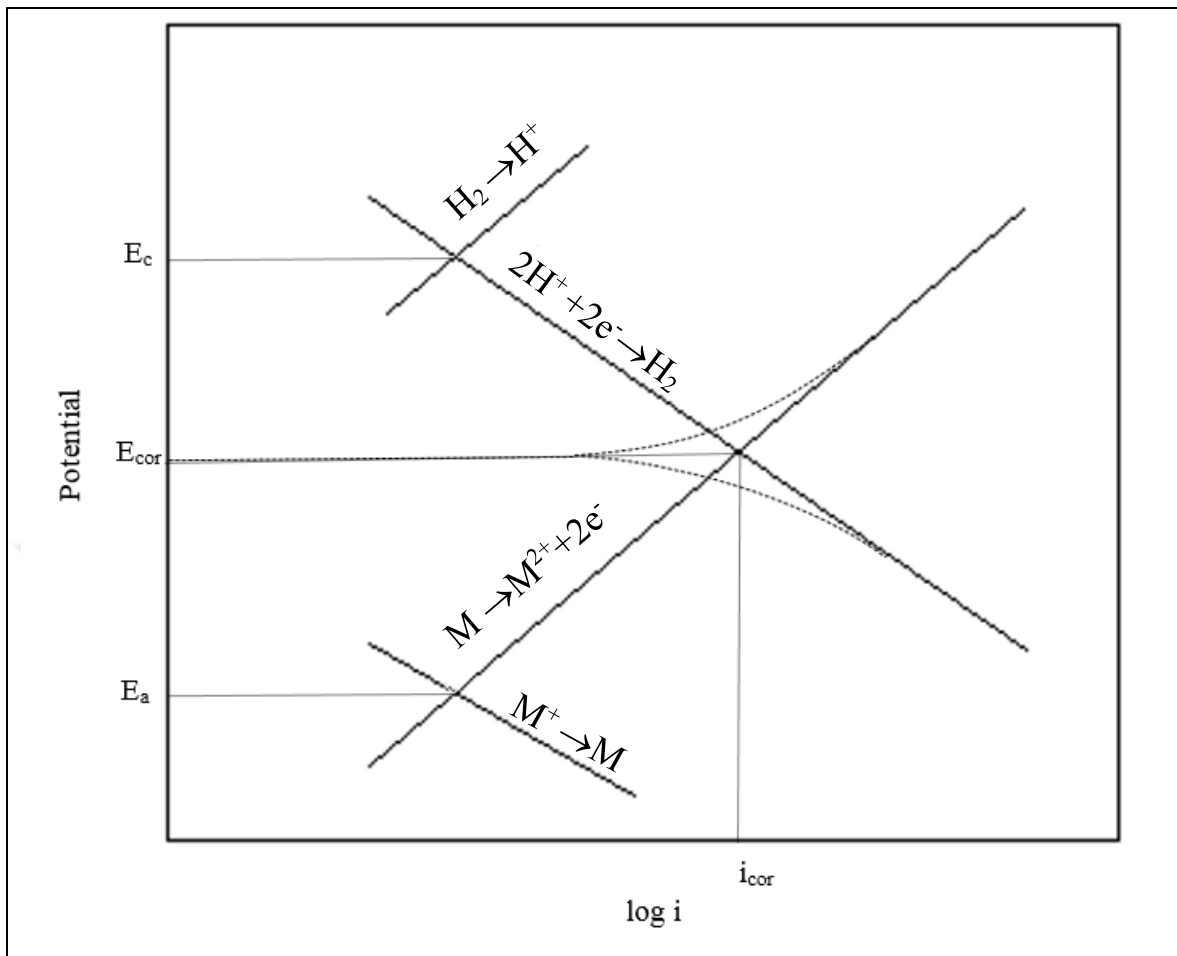


Figure 2.5. A schematic polarization experiment

2.3.2. Solution Resistance (R_u)

An ohmic drop gradient occurs through the electrolyte between the working electrode and the auxiliary electrode (counter electrode) when applied current is passed inside the electrochemical polarization cell. The schematic representation of an electrochemical polarization cell is shown in Figure 2.6.

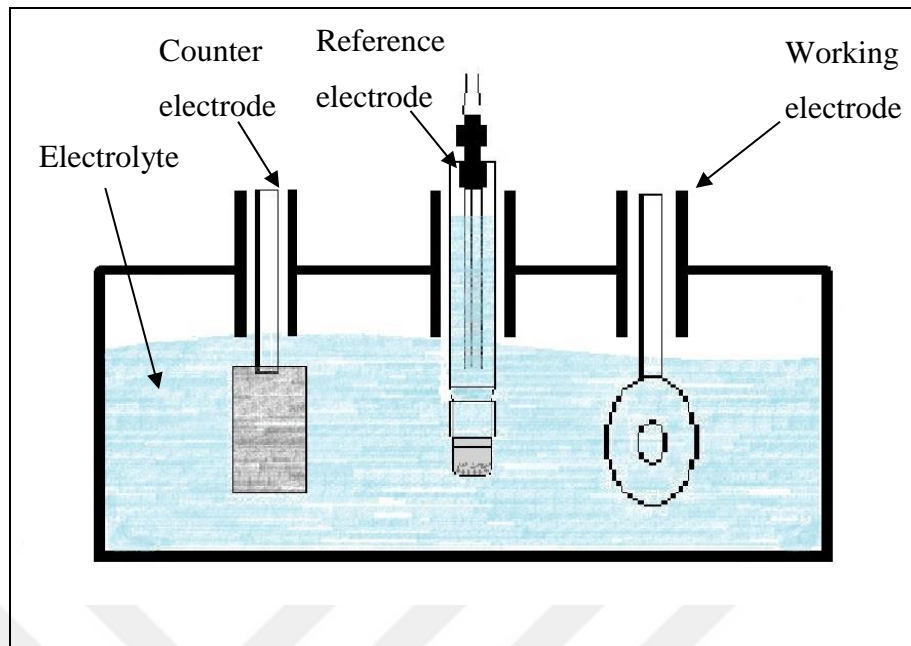


Figure 2.6. Three electrode polarization cell

The magnitude of the ohmic potential drop in solution depends on the concentration and mobility of the dissolved ionic species. The ohmic potential drop between the working electrode and the reference electrode can be calculated as;

$$E_{\text{soln}} = I R_{\text{soln}} \quad (2.18)$$

where R_{soln} is the solution resistance between the working electrode and the reference electrode, I is the current. The potential drop causes the applied potential to be measured differently from the actual potential. This actual potential of the working electrode can be calculated as;

$$E_{\text{act}} = E_{\text{app}} - E_{\text{soln}} \quad (2.19)$$

$$E_{\text{act}} = E_{\text{app}} - I R_{\text{soln}} \quad (2.20)$$

2.4. TYPES OF CORROSION

Various mechanisms may result in different types or forms of corrosion. These corrosion types are listed below;

- Pitting Corrosion
- Uniform Corrosion
- Crevice Corrosion
- Galvanic Corrosion
- Environmentally Induced Cracking
- Hydrogen Damage
- Intergranular Corrosion
- Erosion Corrosion

Pitting corrosion is characterized by the localized loss of metal. In cases where this corrosion is excessive, deep pits are observed. Uniform corrosion is that the metal loss on the surface exposed to the corrosive environment is at the same speed. Crevice corrosion is a regional type corrosion occurring in or near narrow gaps or openings resulting from contact with metal-metal or non-metal-metallic materials. Galvanic corrosion occurs when two different metallic materials are in electrical contact in a conductive solution medium (electrolyte). Then, an electrical potential difference occurs and this difference causes an increase in the corrosion rate of the more active metal. Hydrogen damage is defined as the degradation of the mechanical and physical properties of an alloy due to the entry and movement of hydrogen into the structure. Intergranular corrosion is a special type of corrosion in grain boundaries in the crystal structure of a metal. Erosion corrosion is usually caused by high velocity flow of a corrosive fluid. Pitting corrosion, crevice corrosion and galvanic corrosion are localized corrosion forms and the pitting corrosion is fundamental subject of this study. Therefore, it is explained in more detail in the next part of this theory section.

2.5. PASSIVITY AND LOCALIZED CORROSION

2.5.1. Passivity

Passivity is the loss of chemical activity of metals and alloys in some environmental conditions. Passivity is a phenomenon observed during the corrosion of some metals and alloys, and also it can be defined as the loss of the ability of the metal to react chemically under specific environmental conditions. The corrosion rate of a metal in the passive state is generally very low. The corrosion rate of a metal from the active state to the passive state often decreases in the 2 orders of magnitude. Passivity is due to the formation of a protective film on the surface of the metal under oxidizing conditions at high anodic potentials. An example polarization diagram for a passivating metal is seen in Figure 2.7.

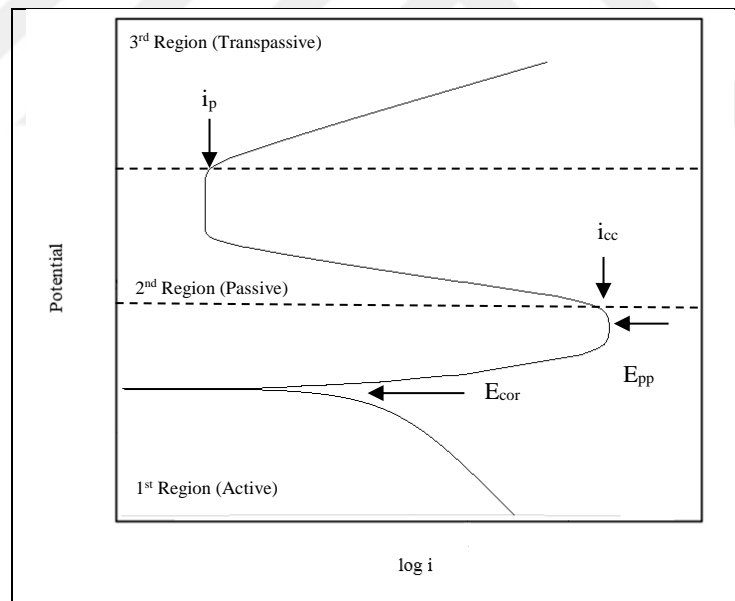


Figure 2.7. Anodic polarization curve of a metal with passivation property. The abbreviations in the graph represents the E_{cor} - corrosion potential, i_p - passive current density, i_{cc} - critical current density and E_{pp} - passivation potential.

Figure 2.7 has three areas of potential.

- First region: In this region where the potential is more negative than the E_{pp} value, the metal is corroding actively.
- Second region: In this region, the metal is passive. As long as the metal potential can be kept within this range, the corrosion rate remains at a minimum.
- Third region: In this region where the passive film is broken, the corrosion rate increases again. Corrosion is in the form of pit formation at the points where the passivating film is distorted.

The anodic current initially rises with the potential (active behavior), then decreases to a small fixed value (passive behavior), and finally rises again (transpassive). This behavior is not a feature of an alloy due to its internal structure, it is the result of the interaction of the alloy in a particular environment. The potential of a metal in an environment is influenced by the balance of oxidation-reduction events at the metal-solution interface. Since a metal does not form a net current when it is immersed in the solution, the potential of the metal refers to the potential corresponding to where the anodic and cathodic lines intersect each other. The higher the oxidizing power of the solution when the cathodic line is higher. In other words, a more oxidizing solution increases the potential of metal. Many commonly used engineering materials such as stainless steels and aluminum alloys are passivating alloys. On the other hand, these alloys are susceptible to localized corrosion such as pitting corrosion.

2.5.2. Localized Corrosion

In contrast to general corrosion (or uniform corrosion), localized corrosion specifically targets a region of the metal structure. Localized corrosion is classified into three different types. These types can be listed as; pitting corrosion, crevice corrosion and filiform corrosion. Pitting corrosion occurs as a result of loss of passivation of a small area. Usually a small hole or cavity is formed. Pitting corrosion in aluminum alloys are frequently associated with intermetallics that are more or less noble with respect to the alloy matrix. Crevice corrosion is often associated with a clogged microenvironment; such environments occur in shielded areas (crevices) such as found under gaskets, washers and clamps. Acidic conditions or oxygen depletion may cause enhanced dissolution of the metal within the

crevice. Filiform corrosion starts from minor defects in the coatings and may cause structural weaknesses [7][8].

2.6. PITTING CORROSION

Pitting corrosion is generally observed in aluminum alloys and stainless steels which are often considered passive alloys. Pits are seen in different shapes and deep grooves (Figure 2.8). Mostly the pits are too small to be seen and the depths are generally same size with its diameter. Pitting corrosion starts with an anodic reaction at a weak point in the metal surface (such as an inclusion or a weak spot on the oxide layer). If metal and environmental conditions are appropriate, this anodic reaction continues rapidly with a series of autocatalytic reactions that give rise to facilitated dissolution. The rapid dissolution occurs in the cavity on the metal surface. When the metal begins to dissolve in an anodic zone (inside the pit), oxygen reduction occurs on the surrounding surfaces simultaneously. Hence, the anode is the pit surface, while the cathode is a very large area around the pit [2] [9]. The excessive positive charges inside the cavity increases when the rapid dissolution of the metal occurs. At that stage, the Cl^- ions are migrated inside the cavity for preserving the electro-neutrality. This Cl^- migrations a further increase in the rate of pitting. As it is known, H^+ and Cl^- ions accelerate the corrosion rate of many metals and alloys. The schematic representation of a growing pit in aluminum is shown in Figure 2.9.

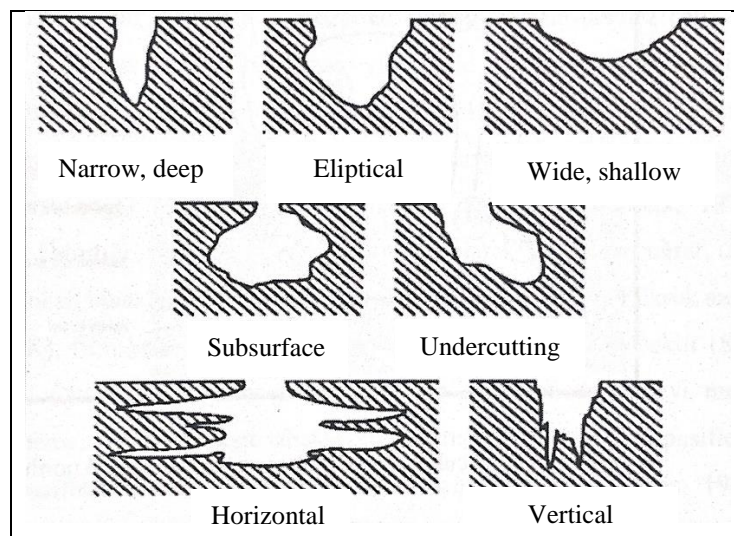


Figure 2.8. The cross-sectional views of the different types of pits [2]

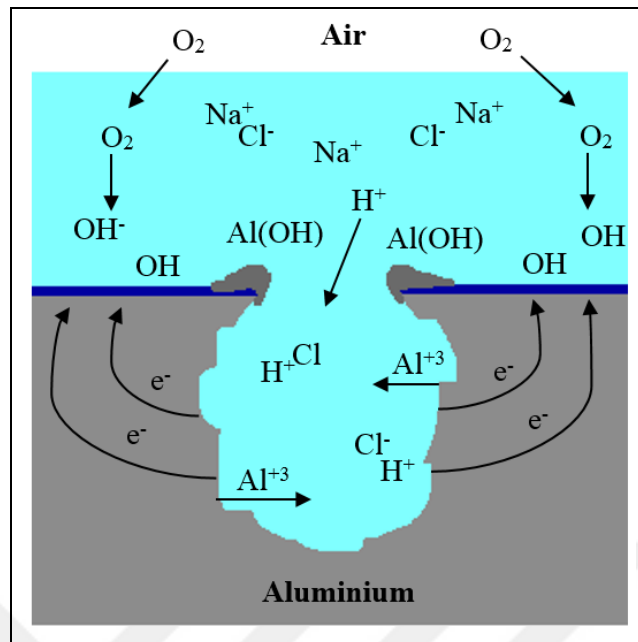


Figure 2.9. Schematic representation of pitting event

2.7. ALUMINUM AND ITS ALLOYS

Pure aluminum is structurally soft and flexible. Thus, it is alloyed with other metals in order to improve its physical and mechanical properties. Many metallic elements are alloyed with pure aluminum for commercial use. The most widely used alloying elements are Cu, Si, Mg, Zn and Mn. Aluminium alloys are designated according to the elements that they contain. The first digit (XXXX) represents the main alloying metal. For instance, 4000 series contains silicon as the main alloying element while 2XXX series contain mainly copper. 1000 series is the commercially pure aluminum. The main alloying metal description is given in Table 2.1 [10].

Table 2.1. Aluminum alloy naming chart [10]

Alloy Series	Main Alloying Metal
1XXX	99.000 percent Minimum Aluminium
2XXX	Copper
3XXX	Manganese
4XXX	Silicon
5XXX	Magnesium
6XXX	Magnesium and Silicon
7XXX	Zinc
8XXX	Other Elements

In this study, AA1050 sheets (at least 99.5 percent Al) were used.

2.8. PRODUCTION METHODS OF ALUMINUM AND ITS ALLOYS

Aluminum sheet production is realized in 3 different methods. The first one is the direct chill casting (traditional method) with hot and cold rolling stages. The second one is the Hazelett method (or known as Alusuisse method) which is continues thin slab casting. The third method used in the production of aluminum sheets consists of twin-roll casting with cold rolling stages. As mentioned above only two of the production methods are compared in this study which are Direct Chill Casting (DCC) and Twin-Roll Casting (TRC) [1].

2.8.1. Direct Chill Casting (DCC)

Direct chill casting constitutes the start of traditional aluminum plate production. The metal which has been melted in the previous process is taken to an area after the furnace exit in order to filter and degas the melted metal. After this unit, the liquid metal enters into water-cooled mold where solid shell is formed and it becomes ingot (Figure 2.10). The size of an ingot can be as large as 9 m long, 2300 mm wide and 760 mm thick [11]. This production technique provides that the properties such as grain size, chemical composition and

mechanical strength remain constant throughout the entire ingot [1]. The continuity of the casting is limited to the casting mold, thus, this method is semi-continuous. The process is stopped to remove the solidified ingot from the casting mold when the limit height is reached. The ingot is then sent to scalping to remove the enrichment zone formed on its surfaces. The scalped ingot is then preheated for hot rolling. The preheating is done also to homogenize the ingot, that is, putting all soluble alloy constituents into a more complete and uniform solid solution [11]. After the hot rolling, the plate is cold rolled and annealed to produce the sheet with the desired properties.

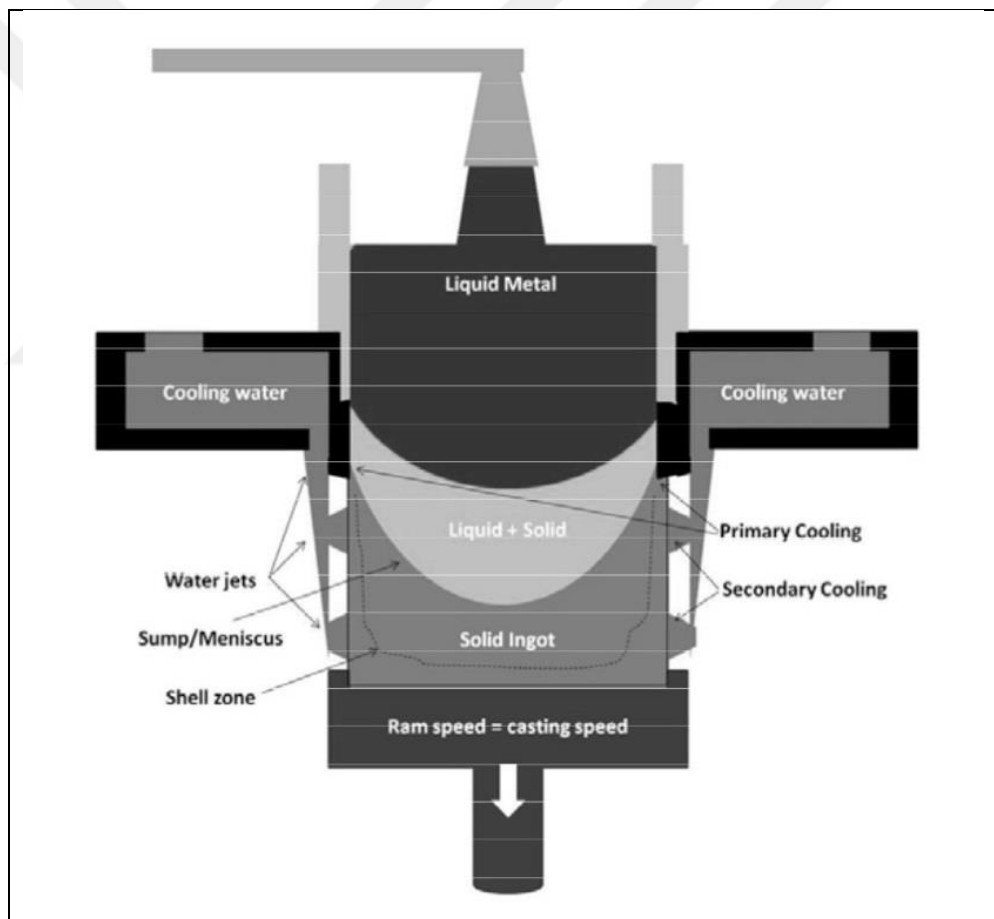


Figure 2.10. Direct-chill ingot casting

2.8.2. Twin Roll Casting (TRC)

Twin roll casting (TRC) is used in aluminum industry for 50 years. Figure 2.11 shows the general representation of the rollers of TRC casting [12].

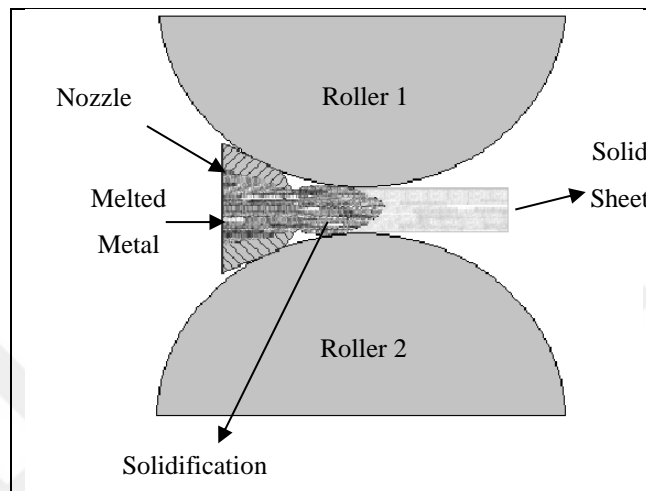


Figure 2.11. Schematic representation of Twin roll casting

The aluminum is melted in furnace and then sent to a holding furnace. The molten metal, after degassing and filtering, enters the rollers from the nozzle (Figure 2.11). The rollers are water-cooled and counter-rotating. The molten metal is solidified quickly between the rollers. Casting thickness is determined by a hydraulic system that moves the rollers. Water based graphite or boron nitrate solution is given to the rollers to prevent sticking of the plate to the rollers [13] [12]. The thickness of the plate from the twin rollers is about 5-10 mm. The plate thus produced is then cold rolled to the desired thickness. Depending on the desired mechanical properties and hardness, annealing can also be performed. In both the DCC and TRC, the final product can be cut into rectangular sheets and or can be rolled as a bobbin.

2.8.3. Differences between DCC and TRC Sheet Production Techniques

Direct chill casting (DCC) technique is a more common technique used for producing aluminum alloy [14]. The main reason for this, DCC is an older technique and all aluminum alloy series can be produced with this technique. The twin roll technique can only be used to produce alloys with a narrow solidification temperature range. However, twin roll casting

is rapidly becoming widespread among manufacturers [15]. The main reasons for this widespread use are less energy consumption in production and lower investment cost. The alloy production method in DC casting technique is subjected to ingot formation with the slow cooling speed, homogenization as a result of hot rolling, and hot rolling high plastic deformation. In TRC technique, these processes are not available. For this reason, DCC and TRC techniques differ to each other in terms of applied thermal-mechanical process parameters. So, there were structural differences between the DCC and TRC production techniques [14,16,17]. The alloys that produced by DCC technique have desirable properties like uniform structure for many alloys generally [18,19]. Furthermore, the surface of the TRC sheets may be defected because of the production technique. These defects can be surface stains and centerline segregation. Lockyer et al. and Yun et al. reported that surface bleeds are formed due to sudden cooling of the melt and roller pressure between the twin rolls, and these contain a large number of intermetallic particles [20,21]. Lockyer et al. reported that AA1100 is very suitable for the formation of the surface bleeds but they did not see the formation of surface bleeds in AA3003 [20]. Gras et al. AA3105 after casting measured the composition of both surface bleeds and centerline segregation [22]. It was observed that the surface bleeds could be up to 1-2 mm in length and up to 150 μm in depth. When the surface analysis was done, they found that surface bleeds were richer in Mn, Mg, Fe, and Cu elements than aluminum (Al) matrix. Birol examined the structures formed in the central plane of the plate by DSC (Differential scanning calorimetry) technique for AA1050, AA3003, AA5754 and AA6016 alloys produced by TRC technique. They concluded that defects on the surface were more easily formed in AA3003 and AA5754 alloys. Intermetallic particles are generally smaller in TRC alloys than those produced by the DC casting method [23]. The authors explained the reason for this difference as slow cooling in the DC casting technique and consequently lower solid solution saturation. Comparing AA1050 alloys prepared by two techniques before cold rolling, it is reported that the undissolved particles (such as Al-Fe) in the TRC sample are smaller than DC [24]. Sanders compared the structures of AA3003 alloys produced with TRC and DCC techniques. When the cross-sections of these alloys were compared, it was seen that the intermetallic particles were smaller in the TRC alloy and concentrated in the near-surface regions.

2.9. LITERATURE SURVEY OF PITTING CORROSION OF ALUMINUM ALLOYS

Trueba et al. studied the corrosion behavior of the Aluminium alloys by using the cyclic polarization technique at a 0.6 M of NaCl solution. Tests were conducted in both naturally aerated and deaerated solutions. Using the cyclic polarization measurements pitting potential, repassivation potential and pit transition potentials were determined for various aluminum alloys [25]. There were five different alloys tested in the study. The alloys were AA1050, AA5083, AA5754 and AA6082 and AA2024. The alloys surface were not polished the metals were used as received. [25]. The cyclic polarization measurements were carried out after 10 minutes of open circuit potential measurements. The scan rate was 10 mV/min. According to the results of cyclic polarization measurements, the resistance of the alloys to corrosion was discussed. They determined the pitting potential, the protection potential and the so called the pit transition potential for the alloys. E_{pit} for AA1050 was -742 mV in the deaerated solution and -700 mV in the naturally aerated solutions. They ordered the alloys in increasing tendency for the localized corrosion as AA1050, AA2024, AA5083, AA6082 and AA5754. The alloys surfaces were investigated with optical microscopy and AA1050 have open and irregularly shaped pits in the deaerated solution.

Speckert and Burstein observed the initiation and growth of metastable pitting in microelectrodes of pure aluminum, titanium and iron binary aluminum alloys as well as in AA1050. Small surface area was used to detect the small current transients These small current transients have been detected in picoampere ranges. To minimize and neglect the external noise the electrochemical experiments had been carried out inside the Faraday cage. The authors tried to observe the anodic and cathodic current transient during the metastable pitting. Under potentiostatic conditions, pure aluminum and the titanium-aluminum alloy exhibited only anodic peaks while AA1050 and the iron-aluminum binary alloy exhibited both anodic and cathodic peaks. The cathodic peaks were suggested to be related to the hydrogen evolution at the iron-rich intermetallic phases [26].

Krakoviak and Darowicki studied the pitting corrosion of 1050A with two different methods which were potentiodynamic measurements and acoustic emission measurements. Electrochemical experiments were done in a three electrode cell. Both electrochemical and emission measurements were performed simultaneously. The cyclic polarization

measurement is widely used to detect the pitting corrosion of aluminum. On the other hand, acoustic emission method was also used to investigate the pitting corrosion in the study. The experiments were performed with the 0.002 M of sodium chloride solution. The scan rate for the cyclic polarization measurement was 1 mV/s. The authors measured similar cumulative distribution functions of pitting by the two methods. They stated that the acoustic emission method is able to detect the pitting even before the metastable pitting initiation [27].

In the study of Comotti et al., the corrosion behavior of commonly used aluminum alloys (1050, 6082, 2024 and 7075) were investigated in 0.6 M NaCl solution. They determined pitting potentials, protection potentials, potentials at the inflection point and the current densities at that inflection point. The inflection point was seen after the scan reversal. For all other alloys that used in the study except 1050, the inflection point was found. Surface morphology analysis were also done in the study. Before using the alloys, the surface was polished up to 3 μ m cloth. The scan rate of the cyclic polarization measurement was 10 mV/min. Open circuit potential was measured for 10 minutes until the equilibrium before each experiment. After the electrochemical test, the surface was investigated and concluded that the AA1050 surface contains elongated particles that formed mostly Fe and Si. The electrochemical measurements results showed that the stable pits are formed when the potential is positive than -700 mV for AA1050 according to Comotti et al. study [28].

Abdulstaar et al. examined the corrosion behavior of the ultra-fine grained AA1050 and coarse grained AA1050 by using the weight loss technique and potentiodynamic polarization measurements. They used 3.5 percent NaCl solutions are used for both corrosion tests. For the electrochemical experiments, a three compartment cell was used, where the working electrode is the aluminum alloy, a saturated calomel electrode and a platinum mesh as a reference electrode and counter electrode respectively. Specimens were polished with SiC paper up to 4000 grit and then polished with diamond paste up to 1 μ m for electrochemical experiments. The potential scan was carried out from -1.5 V vs SCE to 1.5 V vs SCE with a scan rate 0.2 mV/s. On the other hand, immersion tests also carried out for investigating the weight loss of alloys. The polishing procedure for immersion test was partly different from the electrochemical experiments. As described above alloys surfaces were polished with SiC paper up to 4000 grit and immersed to the concentrated NaCl solution for a various time intervals up to 70 days. After both corrosion tests the surface was analyzed with scanning

electron microscopy. After weight loss experiments the corrosion rate was calculated in terms of mils per year. As mentioned before the main purpose of the study of Abdulstaar et al. is to compare the two different AA1050 that produced with different grain size. The results of cyclic polarization measurements showed that the ultrafine grained alloy is more resistant to the corrosion than the as received alloy. Therewithal, the SEM analysis of the results after cyclic polarization measurement revealed that the pits on the surface are smaller on the ultrafine-grained specimens. On the other hand, weight loss immersion tests also revealed that the smaller grained alloys are more durable to corrosion attacks [29].

Gheem et al. studied pitting corrosion in the aqueous solutions that contain perchlorate, sulfate and chloride anions for AA1050 and pure aluminum. They used open circuit potential measurement and polarization scans as electrochemical tests for comparing the corrosion behavior of specimens. All electrochemical tests has been carried out in a 0.5 M different aqueous anion solutions. The specimens surfaces were etched with NaOH before experiments and rinsed with water because of that, they did not polished the surface. The test area was fixed at 1.13 cm². They used three compartment cell same as the Abdulstaar et al. study. Gheem et al. also tested the electrolyte in terms of the oxygen concentration of the solutions. The solution has been purged with oxygen and nitrogen for 30 minutes before the corrosion tests and also continue to purging during the experiments with a lower flow rate. Open circuit potential (OCP) measurements were done for 8000 seconds until the reaching the constant potential value. The results of OCP are -0.95 V -1.41 V versus SCE for AA1050 and high purity Al respectively at deaerated 0.5M NaCl solution. On the other hand, open circuit potential measurements also were done before the cyclic polarization measurements. The forward and reversed scan was carried out from -1.4 V vs SCE to 1.4 V vs SCE with a scan rate 0.5 mV/s. The results from polarization experiments shows that the pitting potential for both AA1050 and pure aluminum are similar in aerated 0.5 M NaCl solution. All in all, perchlorate, sulfate and chloride anions affect the corrosion on the surface of the AA1050 when the alloys contact with these anions. The other aim of this study is to show the pH and the oxygen concentration effect of the electrolyte. For instance, it was stated that the corrosion potential of the AA1050 is a more positive value in a deaerated acidic medium than the deaerated neutral medium. They stated parameters such as pH and oxygen concentration need to be controlled accurately to study the effect different anions on the corrosion of the aluminum [30].

Slamova et al compare the microstructural differences of some 5000 series aluminum alloys produced by DCC and TRC in this article. According to their researches, the direct chill casting (DCC) method is generally be used for producing the aluminum alloys. However, DCC method has a high cost and longer production procedure. Because of that, the new method was developed and the twin-roll casting (TRC) method has emerged. In TRC method alloys have 2nd phase particles and small finer intermetallic. There is no any great difference between DCC and TRC alloys in terms of their grain structures. AA5052 and AA5182 alloys were used in this study. X-ray diffraction, scanning electron microscopy and electron backscatter diffraction methods were used to determine the surface inclusions. The etching process with a 0.5 percent HF solution was done for observing the second phase particles. As a result, they reveal that different production methods are affected the surface grain sizes. They also stated that the alloying material has differed the solidification rate and this is directly affected the crystallographic structure of the alloys [16].

Kurt et al. compared the corrosion events in AA6026 and AA6082 that produced by the direct chill casting and twin roll casting in their study. For comparing these production methods, pitting potentials and micro galvanic potentials were determined by using the electrochemical tests. Cyclic polarization measurements and salt spray test were applied to the specimen for comparing the alloys. The alloys were polished with SiC paper and diamond paste up to 3 μm and deaerated 5 percent NaCl solution was used as an electrolyte. Cyclic polarization measurements were performed in the electrochemical cell that graphite and saturated calomel electrode was used as a counter electrode and reference electrode respectively. The NaCl solution was deaerated with N_2 gas for one hour before starting the experiments. The purging was also continued while the experiment performed. Before polarization measurements open circuit potential measurements was done. The pitting potentials and repassivation potentials had been calculated using the results of the cyclic polarization measurements for both types of alloy. Another method that used for comparing the alloys is salt spraying test. The specimens that used in this test were not be polished they used the alloys as received at the same concentrated solution of NaCl for 48 hours. After each measurement, working electrodes were analyzed by SEM and the comparison has been made. The results reveal that DCC and TRC alloys have a different microstructural form. This microstructural difference cause to the more negative values of pitting potential for TRC alloys. Kurt et al. stated that the more negative pitting potential causes the weakening

of the oxide film layer and makes the suitable environment for the formation of pits. Furthermore, they also reported that the pit sizes are smaller and the depth of the pits are smaller in the TRC alloy [31].



3. MATERIALS AND CHEMICALS

3.1. MATERIALS

An important device in electrochemical experiments is the potentiostat/galvanostat. Also, corrosion cell is another important equipment. The specification of the device and the corrosion cell are given in Table 3.1. The alloy surfaces were polished with a different grit SiC papers, the grid and average grain sizes were given in Table 3.1. The test surface is limited with electroplating tape that information is given in Table 3.1.

Table 3.1. Detailed specifications of materials that are used in this study

Material Name	Supplier	Specifications
Corrosion Cell Kit (Flat Cell)	Bio-Logic Science Instruments	<ul style="list-style-type: none"> Flat Cell with jacket and three holes. Volume: 250 mL [32]
Counter Electrode	Bio-Logic Science Instruments	<ul style="list-style-type: none"> Platinum gauze electrode - 80 mesh Dimensions: 25mm x 35 mm Wire diameter: 0.08 mm Surface area: 2.5 cm² [33]
Reference Electrode	Bio-Logic Science Instruments	<ul style="list-style-type: none"> RE-2BP calomel reference electrode Length: 92mm - OD: 6mm Electrolyte: KCl Junction: Ceramics [34]
Abrasive Silica Paper (SiC)	Metkon	<ul style="list-style-type: none"> P800, 22 μ P1200, 15μ P2500, 8μ [35]
Electroplating tape (470)	3M	<ul style="list-style-type: none"> 25.4 mm x 32.9 m [36]

Table 3.2. Detailed specifications of devices that are used in this study

Device Name	Supplier	Specifications
Potentiostat/Galvanostat (SP-200)	Bio-Logic Science Instruments	<ul style="list-style-type: none"> • Compliance: $\pm 12V$ • Control Voltage: $\pm 10 V$ • EIS Measurement: 3 MHz (1 percent,1°), 7MHz (3 percent,3°) • Current Range: 500 mA to 1μA (10 nA with gain) • Current Resolution: 760 fA (Standard Board) • Floating Mode • Analog Filtering • Calibration Board • Low Current: 6 ranges from 100 nA to 1 pA with resolution to 76 aA [37]
Polishing Device	Buehler	<ul style="list-style-type: none"> • Phoenix alpha 49-5500-230 • Grinder/Polisher [38]
Optic Microscopy	NMM	<ul style="list-style-type: none"> • NMM-800/820 Series Metallurgical Microscope • Infinite plan Achromatic Objective, 5X, 10X, 20X, 50X and 100X. [39]

3.2. CHEMICALS

The names, structural formulas, molecular formulas and the origins of the solid chemicals that used in this study is listed in Table 3.1.

Table 3.3. Name, molecular formula, and supplier of each chemical and solvent used in this study

Name	Molecular Formula	Supplier	Extra Information
Sodium Chloride	NaCl	Sigma - Aldrich	Sodium chloride puriss. p.a., ACS reagent, reag. ISO, reag. Ph. Eur., ≥99.5 percent [40]
Potassium Chloride	KCl	Sigma - Aldrich	BioXtra, ≥99.0 percent (Sigma-Aldrich) [41]
Nitric Acid	HNO ₃	Sigma - Aldrich	Nitric acid puriss. p.a., 65 percent (Hg ≤0.0000005 percent), ≥65 percent
Ethanol	C ₂ H ₅ OH	Merck	Absolute for analysis EMSURE® ACS, ISO, Reag. Ph Eur [42]
Epoxy Resin and Hardener	-	Metkon	<ul style="list-style-type: none"> • EPOCOLD -H • EPOCOLD -R [35]

4. METHODOLOGY

4.1. ELECTROCHEMICAL SYSTEM

The electrochemical systems and the preparation of electrodes are explained below.

4.1.1. Working Electrode

The working electrode is the main electrode with which the electrochemical tests were performed and analyses were done. Commercial AA1050 DCC (H24, 2 mm thickness) and AA1050 TRC (H14, 2 mm thickness) alloy plates were used as working electrodes in this study. The only difference between H14 material and H24 material production processes is that H14 is produced by deformation and H24 is produced by partial annealing in the last step of production. These processes are not processes that will make a difference in terms of intermetallics of alloys. The chemical compositions of the alloys are given in Table 4.1.

Table 4.1. Elemental composition of AA1050 DCC and TRC samples in wt percent

	Direct Chill Casting	Twin-roll Casting
Element	Percent (%)	Percent (%)
Fe	0.31	0.29
Mn	0.00	0.00
Si	< 0.20	< 0.20
Mg	0.00	0.00
Cu	0.00	0.00
Al	> 99.5	> 99.5

4.1.1.1. Sample Preparation and Polishing Procedure

Samples were prepared by using cold molding technique. Resin and hardener was mixed in a specific proportion to obtain epoxy mixture. The multi-core electrical cables were attached to the coupons that were cut with a dimension of 2 cm x 2 cm. The prepared AA coupons were placed in to the center of the plastic mold that is seen in Figure 4.1. The mixed resin mixture is poured in to the mold approximately 10 mm thickness. The samples were left to dry at least for 8 hours.

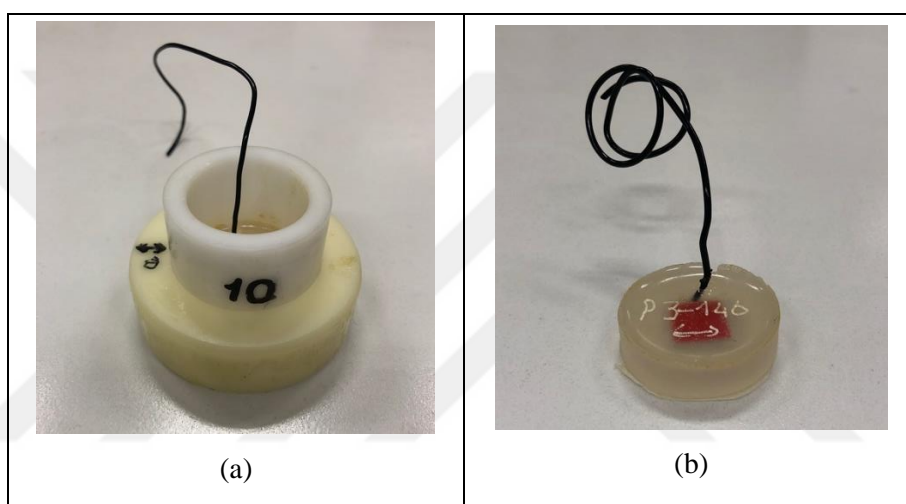


Figure 4.1. The representative image of (a) AA in a mold and (b) image of working electrode

The molds were separated from the epoxy when the samples dried and the working electrode is ready to test. The representative working electrode is shown in Figure 4.1 (b). The prepared working electrodes were labeled, and, then stored in specific sample boxes. The sample surface were polished before each experiments for getting rid of the production oil and obtain a smooth surface. The polishing procedure was done in the same way for all electrochemical method. The detailed information about the polishing procedure is given below;

- P800, 30 seconds, low speed
- P1200, 1 minute, low speed
- P2500, 1 minute, low speed

The used polishing material is given in material section. One working electrode was used in all electrochemical technique except the electrochemical noise measurements. Because of that one sample was polished according to the polishing procedure that is described above and then sonicated in ethanol for 5 minutes. Two working electrodes of the same alloy was used in the electrochemical noise measurements. The same polishing procedures were done for electrochemical noise experiments. The test surface area of the working electrode was limited with electroplating tape with a 0.8 cm diameter (0.5 cm^2) for all method except metastable pitting experiments. In metastable pitting the test surface of the working electrode was a circular area of 2 mm diameter (0.03 cm^2). The representative working electrode with a electroplating tape diameter are given in Figure 4.2.

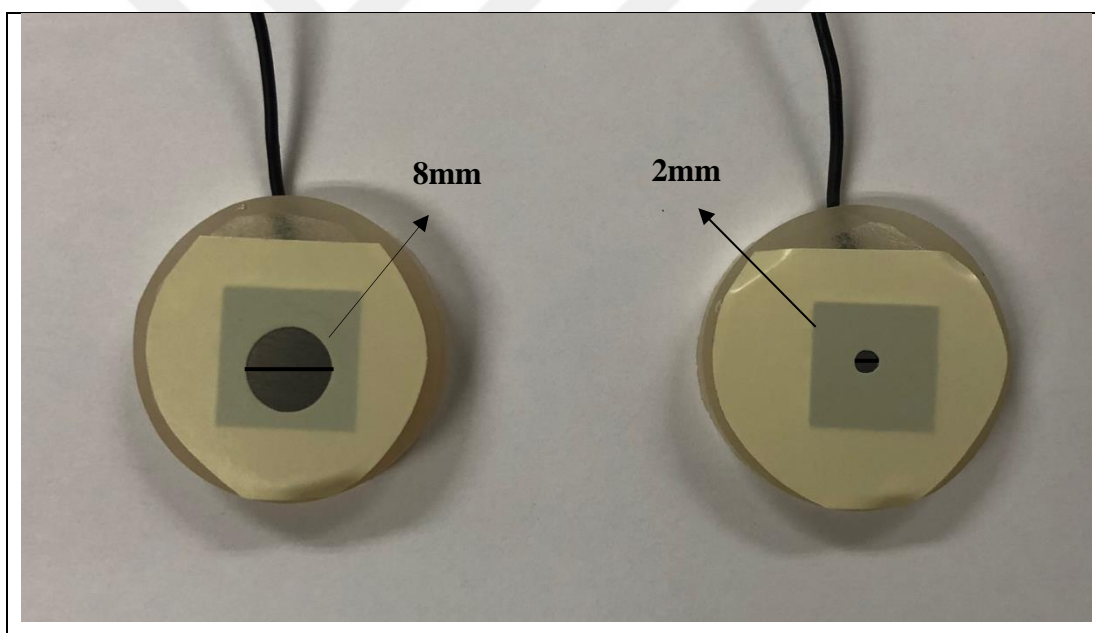


Figure 4.2. Working electrodes with different surface areas. A hole was punched on the electroplating tape to obtain the desired test surface area.

4.1.2. Counter Electrode

A potential measurement requires two electrodes as a minimum requirement, one of which is the reference electrode and the other is the working electrode. In current measurements, systems consisting working and reference electrodes may not provide a healthy response due

to ohmic resistance, especially in high resistance solutions. Therefore, a third electrode is required to be more reliable results. Because of that the counter electrode has an important role in electrochemical experiments. In this study platinum gauze 80 mesh was used and the detailed specifications were given in Table 3.1 in materials section. The representative image of the counter electrode is given in Figure 4.3.

4.1.3. Reference Electrode

The electrode potentials cannot be measured in absolute terms but can be found by comparing them with the potential of the reference electrode. Because of that reference electrode is important to key components of the electrochemical systems. In potentiometric measurements, working, counter and the reference electrode are combined to form a cell and the potential difference between them is measured. In 3 compartment cell system, the reference electrode is held close to the working electrode for reducing the solution resistance. The image of the reference electrode that used in this study is shown in Figure 4.3 and the specifications were given in Table 3.1 in materials section. The types of the reference electrode is the saturated calomel reference electrode with a ceramic junction and filled with saturated KCl. The reference electrode was controlled with a separate laboratory reference electrode before each uses to check its reliability.

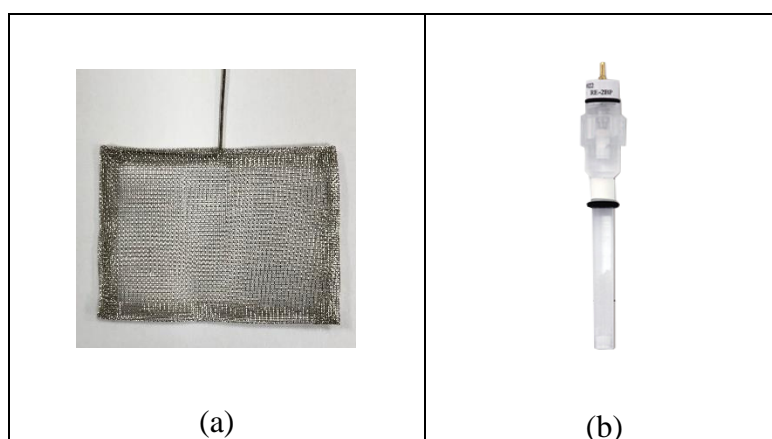


Figure 4.3. (a) Pt mesh counter electrode and (b) SCE Reference electrode that are used in electrochemical experiments

4.2. ELECTROCHEMICAL TEST

In the sections below details of the electrochemical tests are given. There were six different electrochemical test used in this study. Before open circuit potential measurements, cyclic potential polarization, repassivation potential, galvanostaircase polarization and metastable pitting measurement techniques, solutions were de-aerated with high purity (99.999 percent) Nitrogen gas for 1 hour. Electrochemical noise measurements were done with naturally aerated sodium chloride solutions. A three electrode cell (Biologic Flat Cell) was used in the experiments except the noise measurements (Figure 4.4). On the other hand, the electrochemical noise experiments were performed in custom made cell that is show in Figure 4.5. Both cells had a water jacket to keep the temperature constant. All electrochemical experiments were conducted at 25 °C. Furthermore, the solution resistance (R_{soln}) was determined in each experiment with the impedance measurements (with a frequency of 100 kHz). R_{soln} measurement was done by using the IR compensation (ZIR) technique which is a built-in function in the potentiostat (EC-Lab, EC-Lab Express for noise measurement).

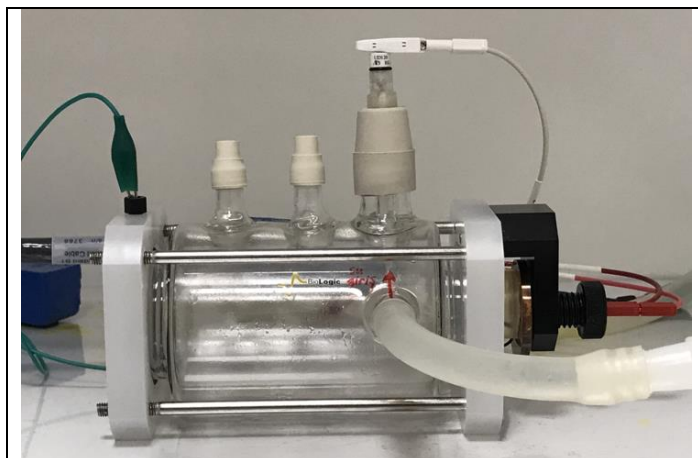


Figure 4. 4. Electrochemical polarization cell (Biologic flat cell)

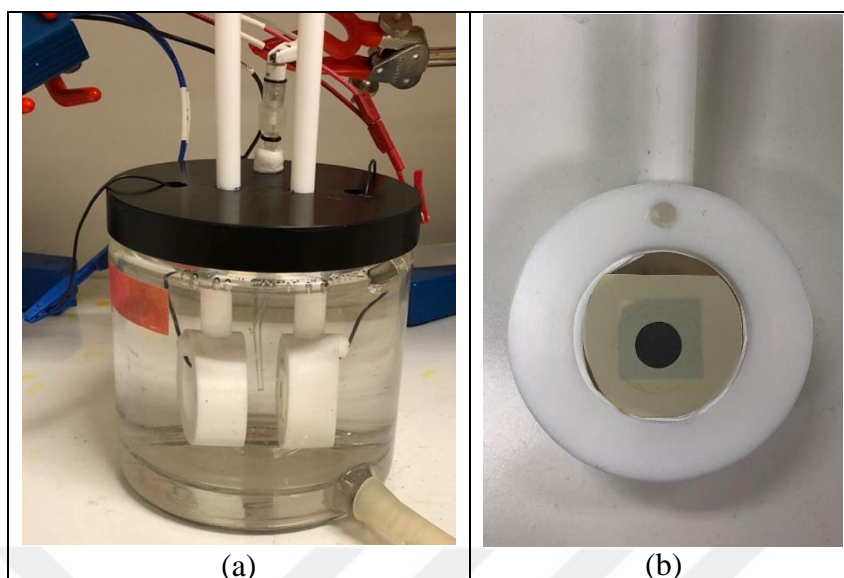


Figure 4. 5. (a) Electrochemical polarization cell for noise measurement (b) One of the working electrodes

The electroplating tape with a hole was attached to a coupon. This enabled the measurements on a circular test area of desired surface area be conducted. All electrochemical experiments were performed by using a Biologic SP-200 potentiostat/galvanostat device. The device is shown in Figure 4.6. An optical microscope was used to examine the test surface.

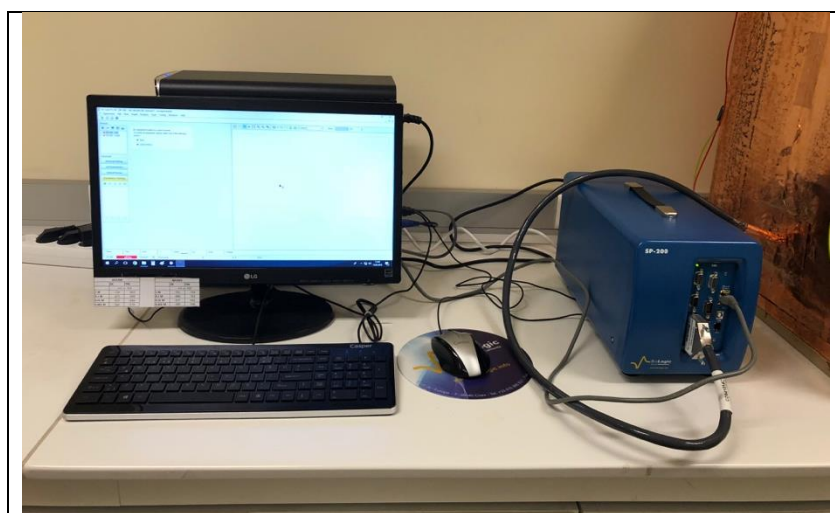


Figure 4.6. Representative Biologic potentiostat/galvanostat device

4.2.1. Microstructure Investigations

Microstructure investigations were performed on the outer surfaces of the plates in TUBITAK MAM laboratories. Microstructural analysis was performed after the surface preparation was done. The sample surface was first polished with P1200 and P2500 SiC papers. Then, the surface was polished with 3 μm diamond paste and 0.05 μm colloidal silica. The last step of the preparation was the etching the surface with 0.5 percent HF. Intermetallics were examined by optical microscope (Nikon Eclipse L150) and SEM-EDS (Jeol JSM-6335F) technique.

4.2.2. Open Circuit Potential (OCP)

Corrosion potentials of the alloys were measured by open circuit potential measurements. The OCP measurements were done in three different concentration (1 M, 0.1 M and 0.01 M) of sodium chloride solutions. During the OCP measurement no potential or current is applied to the working electrode (the sample) and only its potential with respect to the reference electrode is measured. 350 mL of sodium chloride solution was deaerated with N_2 for 1 hour until the OCP measurement was started. A sample coupon was polished according to the method given in section 4.1.1.1 and sonicated with extra pure ethanol for 5 minutes for cleaning. The sample was dried at room temperature. An electroplating tape with a hole of 8 mm diameter was attached to the surface of the electrode. This corresponds to a surface area of 0.5 cm^2 . The prepared sample (AA1050 DCC/TRC) was used as a working electrode. A platinum mesh was used as a counter electrode and the reference electrode was a saturated calomel electrode. The OCP measurement was done by using EC-Lab. The data acquisition speed was 1 Hz. The measurement were done at least 3 hours.

The sample was removed from cell at the end of the 3 hours and rinsed with deionized water. Washed sample surface was dried hot air stream at 50 $^\circ\text{C}$ using a heat gun. Two repetitions were done for each concentration for each type of alloy. A new coupon was used for each measurement.

4.2.3. Cyclic Potential Polarization Measurements

Cyclic potential polarization measurements were done to determine the pitting potentials (E_{pit}) and the repassivation potentials (E_{repass}) of the alloys in 1 M, 0.1 M, 0.01 M and 0.001 M sodium chloride aqueous solutions. Before each CPP experiment, 350 ml of solution was de-aerated by purging N_2 gas (99.999 percent) through it for 1 h in a gas-wash bottle. Specimen surface was polished to P2500 and sonicated in ethanol as explained in the polishing procedure. After the polishing, an electroplating tape with a hole of 8 mm in diameter was attached to the sample surface. Thus, the test surface area was 0.5 cm^2 . The sample was, then, placed in the solution and the CPP was started after 30 minutes of waiting at open-circuit potential (OCP). The anodic sweep (the sweep in the direction of more positive potentials) was started -200 mV below the OCP and was continued until the vertex current density was reached. Afterwards, the sweep was reversed until the potential reaches the value at the start of the CPP. The sweep rate was 1 mV/s. The vertex current density was 1 mA/cm^2 in experiments in 1 M, 0.1 M, and 0.01 M NaCl and was 0.1 mA/cm^2 for experiments in 0.001 M NaCl.

At least 9 experiments were performed for each alloy in 1 M, 0.1 M and 0.01 M NaCl solutions. In 0.001 M NaCl, at least 5 experiments were done. A new sample coupon was used for each CPP experiment. After the CPP measurement, the specimen was washed with deionized water and dried with a heat gun that blows air at $50 \text{ }^\circ\text{C}$.

4.2.4. Potentiostatic Determination of the Repassivation Potential (E_{repass})

In this method, first, pits are intentionally generated at the surface (activation step). Then, the potential is decreased to a lower value and the behavior of current with time is observed to determine the repassivation potential [43]. The experiments were conducted in deaerated NaCl solutions of 1 M, 0.1 M and 0.01 M concentration. The test surface area was 0.5 cm^2 by attaching an electroplating tape with an 8 mm hole to the surface. The determination in this work consisted of the following steps;

- i. Open circuit potential measurement for 30 minutes.
- ii. First step (activation step); potentiostatic measurement until a total charge of 60 mC passed at a potential above the pitting potential of the alloy in the test solution of the coupon.
- iii. Second step; potentiostatic measurement at a lower potential.

The data acquisition speed was 1 data per second for the OCP measurement. The data acquisition speed during the first and second steps were 2 Hz. The activation potentials in the first step were -650 mV for 1 M NaCl solution, -550 mV for 0.1 M NaCl solution and -500 mV for 0.01 M NaCl solution. In the second step, potentiostatic measurement continued a potential 50 mV or 25 mV lower for 15 minutes. The experiments were repeated with lower potential values for the second step from the OCP with a new sample until the current density drops below a typical value of $1 \mu\text{A}/\text{cm}^2$. At least two experiments were repeated in the vicinity of E_{repass} . E_{repass} was found within a range of 25 mV.

4.2.5. Galvanostaircase Polarization (GSCP)

Galvanostaircase polarization technique is used for measuring breakdown potential (E_b) and protection potential (E_{prot}) of alloys [44]. In contrast to the CPP and potentiostatic experiments, the current is the controlled variable in the GSCP technique. The current was increased from $0 \mu\text{A}$ to $60 \mu\text{A}$ with step of $10 \mu\text{A}$ and, then, decreased with the same step size to $0 \mu\text{A}$. At each current step, the potential of the test alloy was measured for 2 minutes. An average potential of each current step was calculated by taking average of the potential measured during the last 10 seconds. Average potential versus time plot were then plotted. A line was fitted to the potential versus time data for the part of GSCP in which current was increased stepwise. The extrapolation of this data to $t=0$ gave E_b . A line fit was also done on the part in which the current was decreased and the E_{prot} was calculated when the extrapolation to $t=24$ min. Before a GSCP test, OCP was measured for 1 minute. The solution concentrations were 0.01 M, 0.1 M and 1 M NaCl. The test surface area was 0.5 cm^2 .

In this study, GSCP measurements were performed for 5 times for each alloy type in each NaCl concentration. Average E_b and E_{prot} were calculated by taking the arithmetic average of the values determined in five measurements. The data acquisition speed was 2 Hz.

4.2.6. Metastable Pitting

In this method, the solutions concentrations were lower because the number of metastable pits can be too large in highly aggressive conditions, which can make the analysis difficult. Thus, 0.01 M and 0.001 M deaerated NaCl solutions were used. Solutions were deaerated with pure nitrogen gas (99.999 percent) for 1 hour. To decrease the background current so that individual metastable pits can be determined, the test surface area was also lower. An electroplating tape with a hole of 2 mm diameter was attached to the coupon surface. Hence, the test surface area was 0.03 cm². It is known that metastable pits can form at potentials below the pitting potential. Potentiostatic runs were performed to study the metastable pitting activity of the alloys in NaCl solutions. The experiments were conducted at potentials 50 mV, 75 mV and 100 mV below the pitting potentials of the alloys determined by the CPP experiments. For instance, the pitting potential for the TRC alloy in 0.01 M solution was determined as -646 mV from the CPP experiments so the applied potential that is 50 mV below the E_{pit} was -696 mV. The experiments were repeated two more times under the same conditions. A new coupon was used in each repeat. In the potentiostatic measurement, the current was measured for 30 minutes with a data acquisition speed of 10 Hz. After the experiments, the current versus time plots were prepared and metastable pitting events were determined. Metastable current events could be identified as current spikes in the current versus time data. The criteria for a metastable pitting event was a peak current of at least 4 nA above the background current. The number of metastable pitting events and the charge of each event were also determined from the plots.

4.2.7. Electrochemical Noise Measurement (ECN)

Electrochemical noise measurements can be done to study the localized corrosion of metals and alloys. In this technique, there were two identical coupons of the same alloy production technique immersed in the test solution. Hence, there were two working electrodes. They were located very close to each other in a custom-made cell as shown in Figure 4.5. The potentiostat was used in the ZRA mode to form a galvanic pair between the two electrodes. In the literature, ECN measurements were done after different immersion times have passed and for different durations. For instance, Curioni et al. performed measurements with

99.99 percent pure Al and AA2024 for about 15 h [45]. Homborg et al. measured ECN of carbon steel galvanic pairs in 3 wt percent NaCl solution after immersion 1 h, 2h, 24 h and 48 h [46]. They collected data for different durations. In this study, a pair was immersed in the solution. In one set of experiments, ECN measurements were started 10 minutes later (9 minutes OCP measurement with auto current range and 1-minute waiting time), and data were collected for 3 h with fixed current range. In the second set of experiments, the measurements were started 24 h after the immersion and noise data were collected for 30 minutes. EC-Lab Express software was used in this technique. The electrochemical cell was placed inside a Faraday cage to avoid the external noise. Measurements were performed in 0.1 and 0.01 M naturally aerated NaCl solutions (700 mL). The surface area of working electrode was 0.5 cm². The data acquisition rate was 10 Hz (ten data points per second). A low pass filter of 5 Hz (=Nyquist frequency) was used. The controlled and measured resolutions were 9.92 μ V and 7.63 μ V, respectively. After the experiments, current versus time and potential versus time plots were plotted. Furthermore, power spectral density (PSD) plots were also prepared.

4.2.8. Immersion Tests

In this study, in addition to electrochemical tests, immersion tests were also performed. Immersion tests were performed in naturally aerated 0.01 M NaCl aqueous solution at room temperature. The surfaces of the coupons which were cut from the alloy sheets were polished with P800, P1200 and P2500 grit SiC papers, respectively. These are the alloys to be examined by scanning electron microscopy (SEM) after immersion tests. Another sets of experiment were prepared for optical profilometer analysis. The samples to be examined by optical profilometer were further polished with 1 μ m and 0.25 μ m diamond paste and 0.06 colloidal silica. After sonication with 70 percent ethanol, coupons were dried in the UV cabinet. Then, the electroplating tape with a hole corresponding to 2 cm² area was attached to the coupons surface inside the UV cabinet. The other surfaces of the coupon were covered with tape and only a test area of 2 cm² was in contact with the solution. The immersion cell and its lid were autoclaved and the test solution was filtered using a 0.22 μ m filter to prevent biological growth for a period of 1-week immersion time. The coupons were placed into the solution with their surfaces facing upwards and the immersion time was started. Coupons were removed from the solution at the end of the immersion time, then washed with

deionized water and sonicated in 70 percent nitric acid solution for 1 minute to remove corrosion products [47]. Coupons were kept in desiccator until SEM and optical profilometry analysis. Before the SEM (Jeol JSM-6335F) analysis, the surface was coated with Pt for better images. Surface morphology was obtained by optical profilometer (Bruker Contour GT-K). SEM examinations were performed at TUBITAK MAM and optical profilometer examinations were conducted at Erzurum Technical University.



5. RESULTS AND DISCUSSION

5.1. RESULTS OF MICROSTRUCTURE INVESTIGATIONS

Intermetallics on the surfaces of the alloys were examined using both optical microscope and SEM-EDS. Optical micrographs taken after polishing and etching process are given in Figure 5.1 for DCC (a) and TRC (b) alloys. The dark shapes in the images show intermetallic particles. When Figure 5.1 (a) was compared with Figure 5.1 (b), it was seen that AA1050 DCC alloy contains larger intermetallics. Particles as large as 5-10 μm are seen in the DCC alloy. The particles in the AA1050 TRC alloy are usually smaller than 1 μm . Larger intermetallics in DCC alloys have also been reported in the literature [14,16,48]. On the other hand, results reveal that the AA1050 TRC alloy contains more numerous particles than the DCC alloy. Optical images were analyzed with microscope software. The results obtained about the size and number of intermetallic particles are given in Table 5.1. The software determines the maximum size of each particle. The largest and the average of the maximum sizes are given in the table.

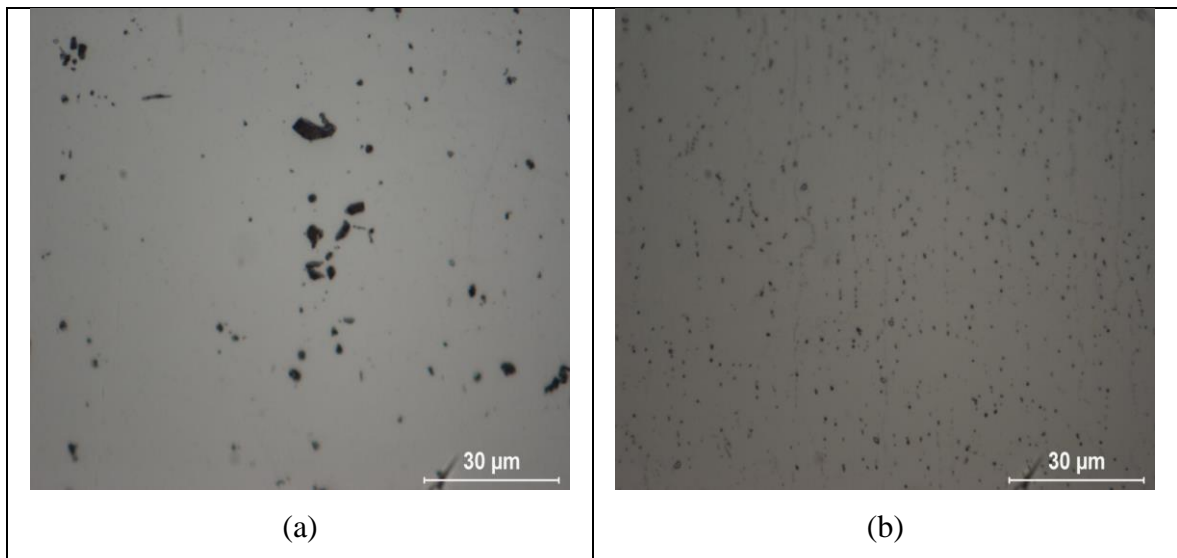


Figure 5.1. Microscope images of AA1050 alloys after etching with HF for (a) DCC and (b) TRC

Table 5.1. Size and number of intermetallic in alloys obtained from the analysis of optical photographs.

	AA1050	
	DCC	TRC
Maximum diameter, μm	10	2.2
Average maximum diameter, μm	1.5 ± 1.5	0.6 ± 0.4
Numbers of intermetallic	111	520

HF etched samples were also examined by SEM-EDS after optical microscopy analysis. Figure 5.2 gives SEM-EDS micrographs of AA1050 for both DCC (a) and TRC (b) alloys. SEM results are compatible with optical microscope results. The alloys produced by the DCC technique contain larger intermetallics than TRC alloys. It is seen that the alloys produced by TRC technique contain more intermetallic when compared with the DCC alloy.

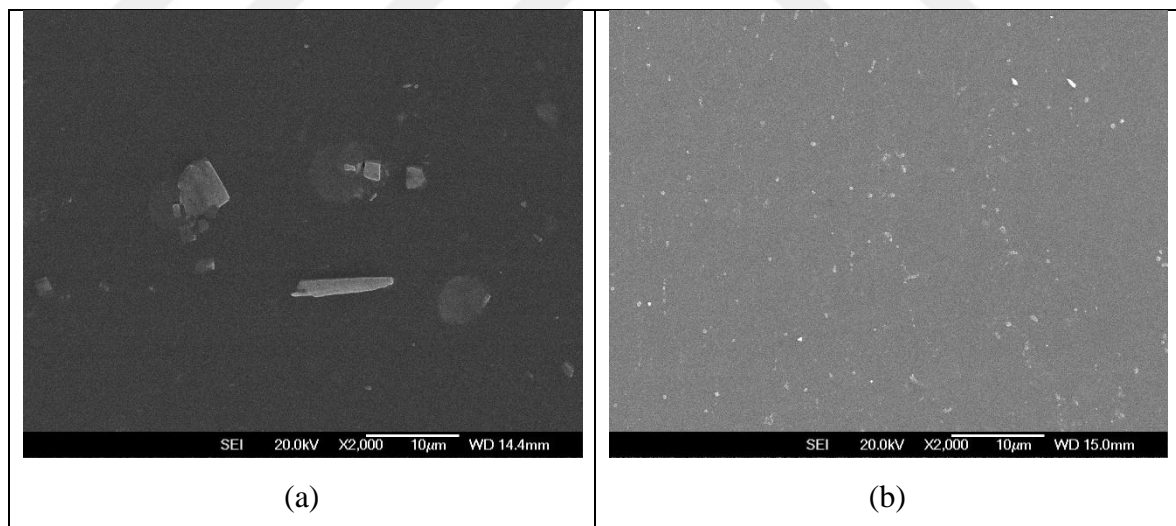


Figure 5.2. SEM images of AA1050 alloys after etching with HF for (a) DCC and (b) TRC

EDS analysis was performed on the intermetallics and the elements of intermetallic were determined. The element analysis results of the intermetallics for AA1050 DCC and TRC alloys are given in Figure 5.3. The intermetallics in the AA1050 DCC alloy contain Al, Fe

and Si. It is seen that the intermetallics in the AA1050 TRC alloy also contain Al, Fe, and Si (Figure 5.3 (b)).

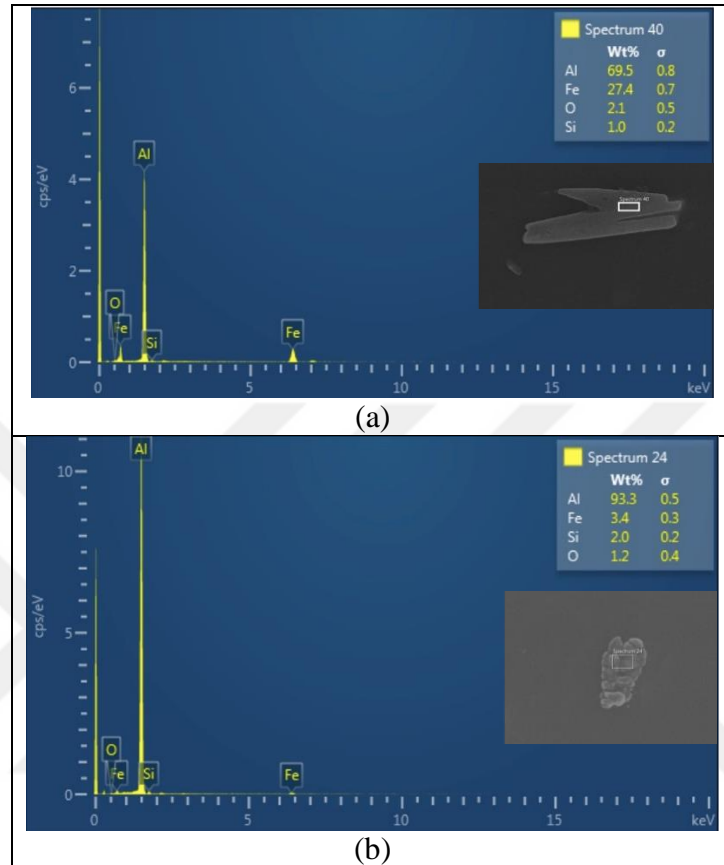
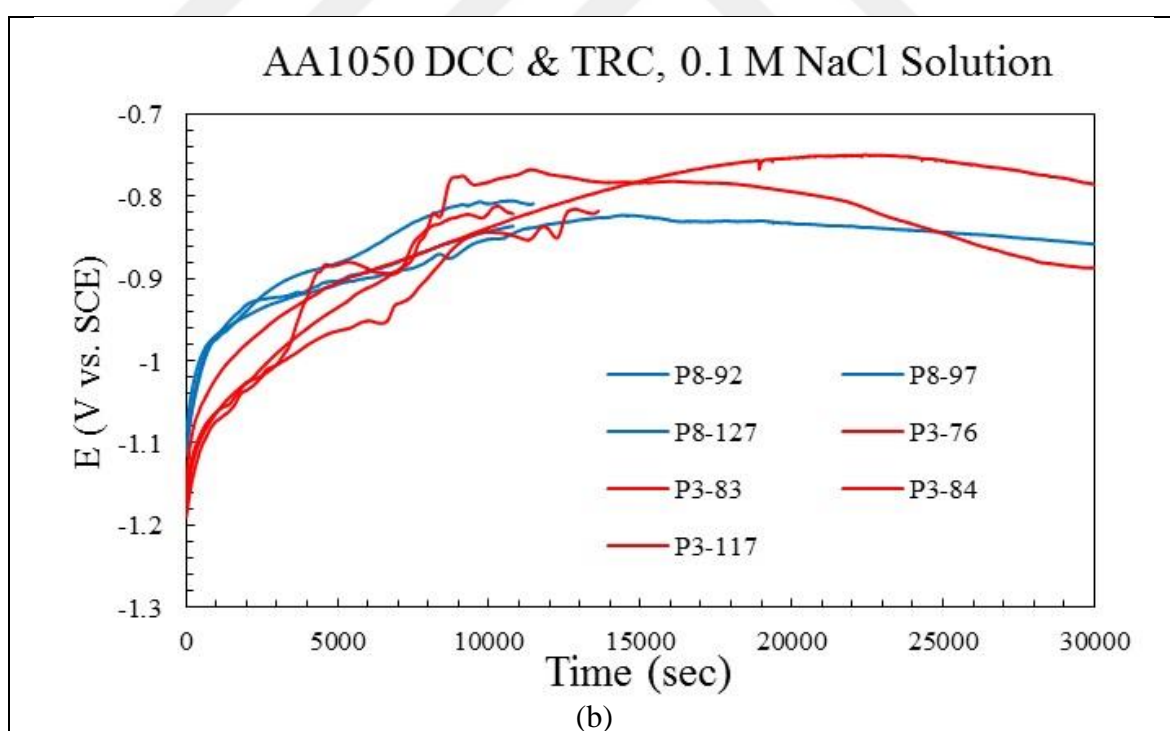
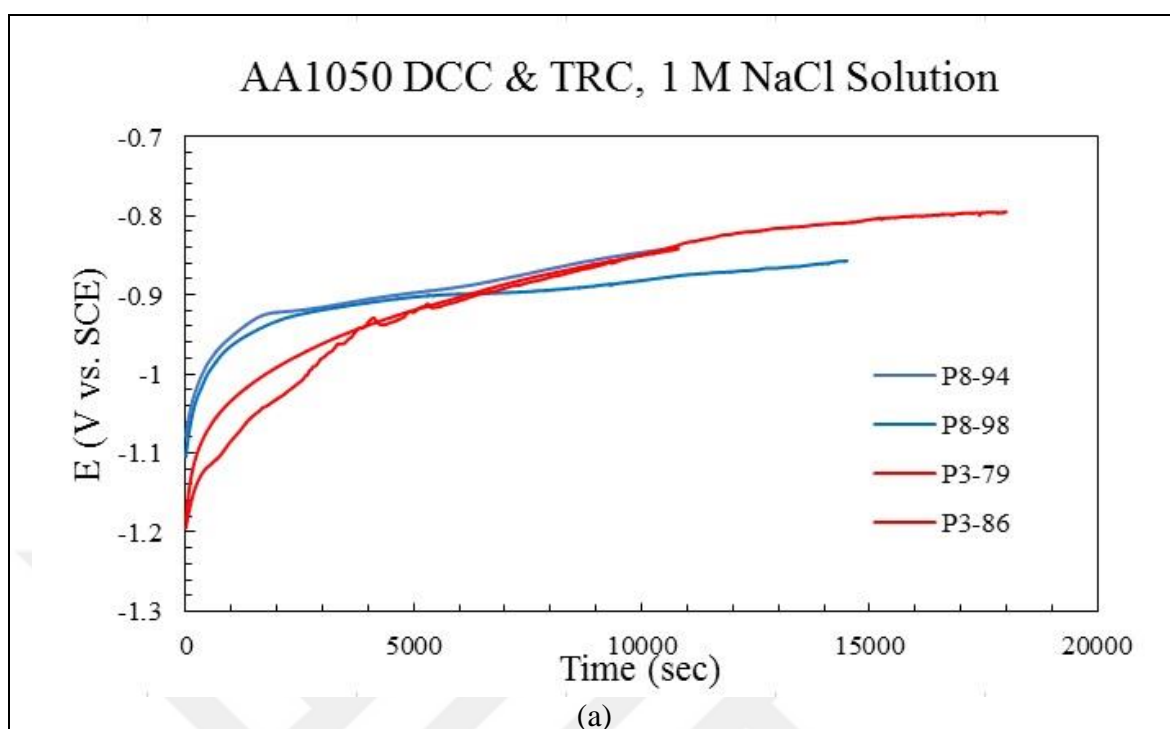


Figure 5.3. EDS analysis of intermetallics for AA1050 (a) DCC alloy and (b) TRC alloy

Particles in both DCC and TRC alloys contain Fe and Si. Fe-containing particles are more cathodic than aluminum matrix and, hence, detrimental in terms of pitting corrosion [49–51].

5.2. RESULTS OF OPEN CIRCUIT POTENTIAL MEASUREMENTS (OCP)

The corrosion potential is referred to as the open circuit potential as the metal surface corrodes freely. Corrosion potential is also called mixed corrosion potential as it represents the compromise potential of the anodes and the cathodes. The potential versus time data was collected at 3 different ion concentrations for both the DCC and TRC aluminum alloys. The OCP measurements are given in Figure 5.4. The blue lines in Figure 5.4 represents the DCC alloys and the red lines shows the TRC alloys.



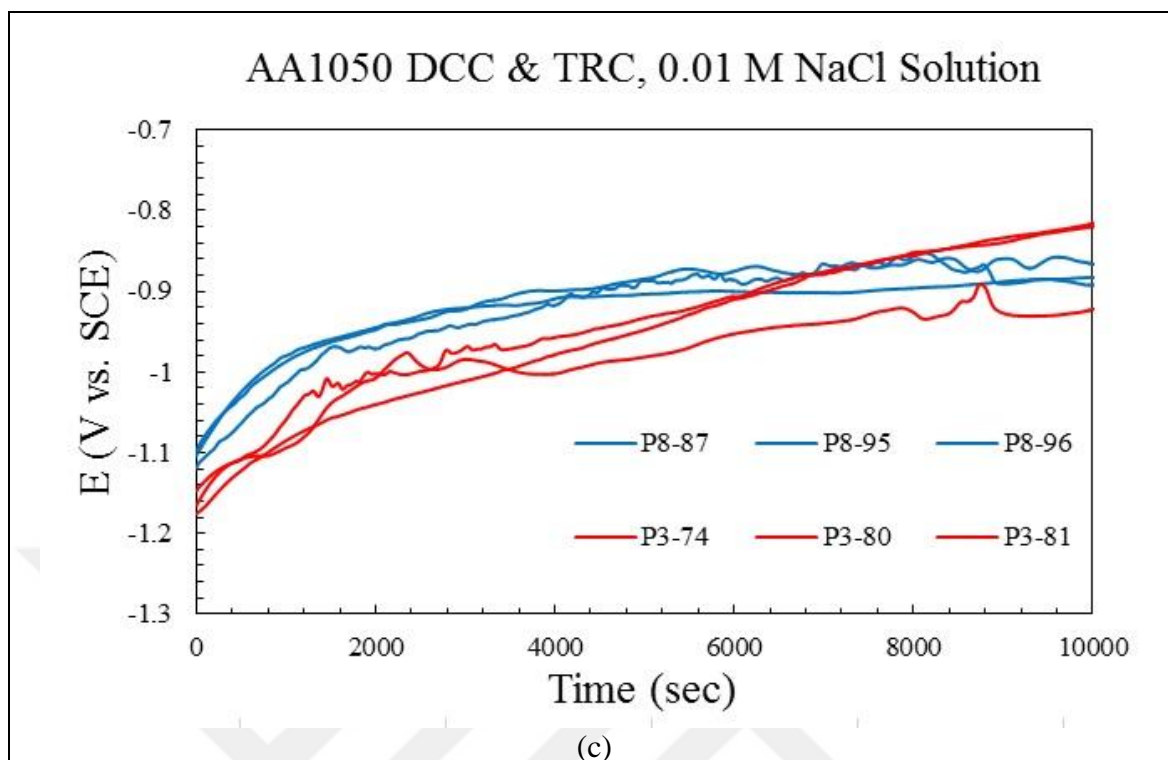


Figure 5.4. Open circuit potential results at (a) 1 M, (b) 0.1 M and (c) 0.01 M for DCC and TRC alloys

The corrosion potential raised rapidly for the first 6000 seconds in the 1 M solution for both the DCC and TRC alloys. During this interval, the TRC alloy potential is more negative than that of the DCC alloy. The potentials start to raise from -1.1 V vs. SCE and -1.2 V vs. SCE for DCC and TRC alloys respectively. After 6000 seconds, potentials show a slow rise until the end of the measurement.

In 0.1 M solution the corrosion potential measurements is represented in Figure 5.4 (b). As can be seen from the graphs the potentials of DCC and TRC alloys also increase sharply starting from -1.1 V vs. SCE and -1.2 V vs. SCE, respectively, until the 9000 seconds. There are some potential variation observed between 9000–12000 seconds in some TRC alloy samples. However, in DCC alloys the potentials change slowly after 9000 seconds.

In 0.01 M NaCl, the DCC alloy showed more positive OCP potential compared to the TRC alloy during about 6000 seconds. As in 0.1 M solution in 0.01 M solution TRC alloy potentials also fluctuate at the beginning of the measurements. On the other hand, fluctuations are also observed in the DCC alloy when the potential changes nearly stabilized.

The corrosion potentials at the end of the measurements are approximately between -800 mV and -980 mV for the three concentration. These potential ranges are similar with the Abdulstaar et al. researches [29]. In that study AA1050 alloy was used and OCP measurements were done for a various surface types. The OCP measurements in the Abdulstaar et al. study performed in naturally aerated 0.6 M NaCl solution. Thus, the corrosion potentials that is found by Abdulstaar et al. study are more positive than that found in this study [29]. The open circuit potential is found approximately -720 mV in that study [29]. The probable reason for this corrosion potential difference is the polishing procedure, the concentration of the electrolyte and the presence of oxygen in the solution.

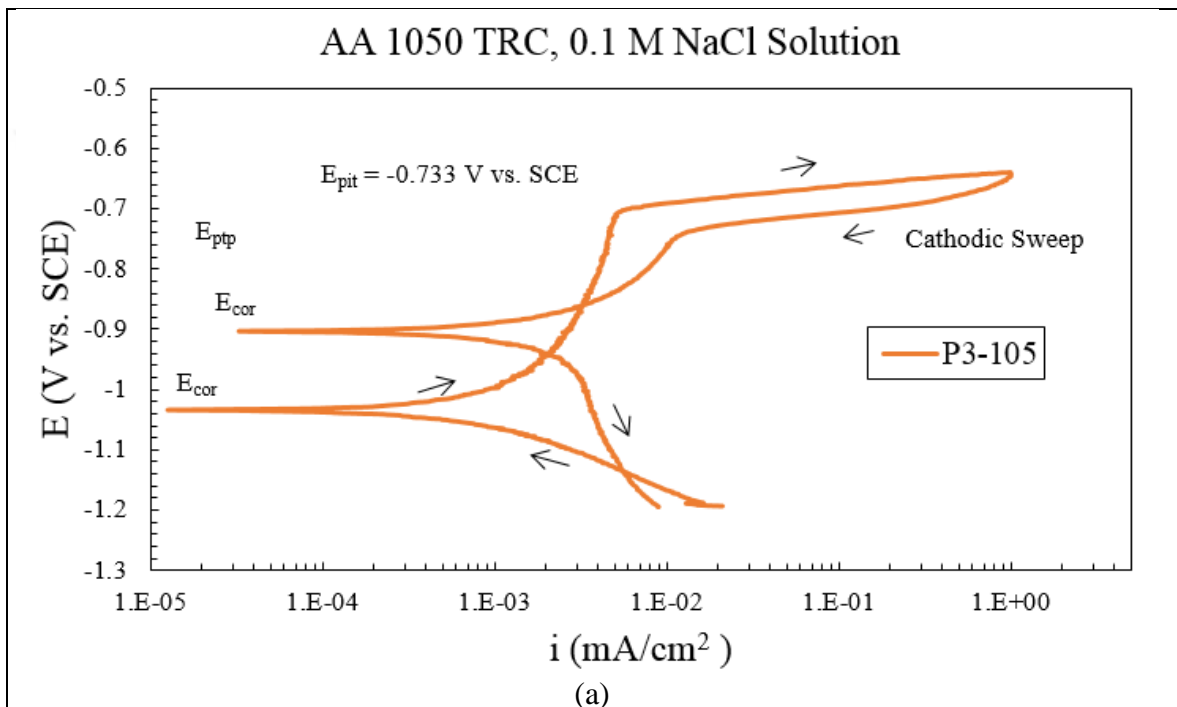
All in all, the slopes are smoother in 1M test solution for both alloys according to the result graphs and the lines are more oscillated when the chloride ion concentrations are decreased. On the other hand, the behavior of the potentials are comparable in literature [29,52].

5.3. RESULTS OF CYCLIC POTENTIAL POLARIZATION MEASUREMENTS

Cyclic potential polarization experiments (CPP) were done to determine the pitting potentials (E_{pit}) of AA1050 produced with the DCC casting technique and the pitting potentials of AA1050 produced with the twin-roll casting. The critical potentials determined from a CPP experiment are illustrated in Figure 5.5. The arrows show the sweep directions. The current density was calculated by dividing the current by the surface area of the electrode.

The scan is started from 200 mV below the potential that was obtained after 30 min OCP measurements. The current density decreased in anodic direction until the mixed potential point (or the corrosion potential, E_{cor}). This potential is the point where the anodic and cathodic reaction rates are equal. The current density increased during the anodic scan after E_{cor} until the pitting potential, where the pits were formed and the current density increased at a fast rate. The pitting potential was determined using the inflection method (Figure 5.5(a)) [53][28]. After pits formed the current density increased until the current reach the vertex point. Then the current density started to decrease in the cathodic direction. The inflection point in reversed scan is designated as pit transition potential (E_{ptp}) according to the Comotti et al. study [55]. E_{ptp} values vary according to solution concentrations and scan rate [54]. The potential at which the cathodic sweep crossed the anodic branch was taken as the

repassivation potential (E_{repass}) as shown in Figure 5.5 (b) [55]. The passive current density (i_{pas}) was calculated by taking the arithmetic average of current densities on the anodic branch between E_{pit} and E_{repass} (Figure 5.5(b)). E_{cor} The current density decreased in cathodic sweep fast after the repassivation potential. E_{cor} on the reverse sweep is the different (more positive) from that found in the anodic scan because of the surface of the alloy changed and pits formed. After that point, the current density increased until the potential where the CPP was started.



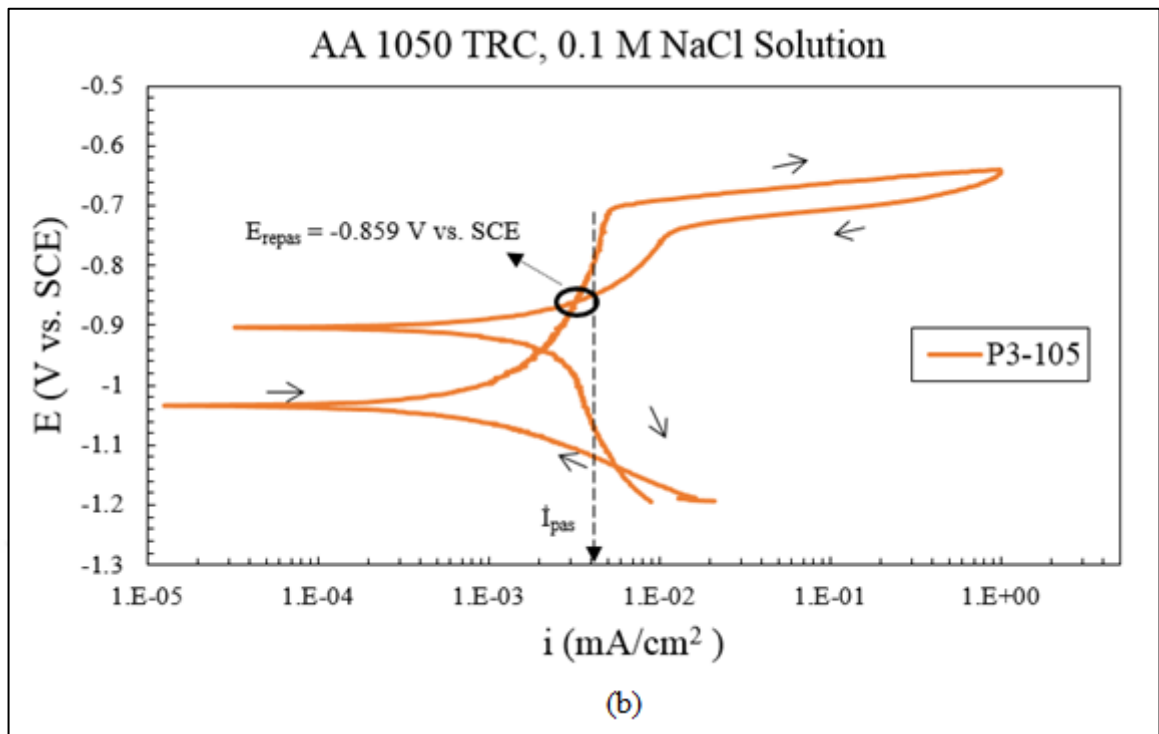


Figure 5.5. (a) Representative pitting potential, (b) repassivation potential and passive current determination for AA1050 TRC in 0.1 M NaCl

The pitting potential is often used to determine the resistances to pitting corrosion of engineering alloys. A more positive (more anodic) pitting potential is an indication of higher resistance to the pitting corrosion [56]. E_{repas} is the potential above which pits already nucleated can grow, but below which pits repassivate. Thus, a higher E_{repas} potential also indicates a higher resistance to the pitting corrosion [57]. Pits are initiated above the pitting potential and grow until the potential is below the repassivation potential.

The current density versus potential graphs are shown in Figure 5.6, 5.7, 5.8, and 5.9 for 1 M, 0.1 M, 0.01 M and 0.001 M aqueous NaCl solutions, respectively. For better illustration only four experiments are shown. The rest of the CPP curves for each alloy and concentration are given in Appendix A. The potentials are corrected for IR drop in solution in these figures.

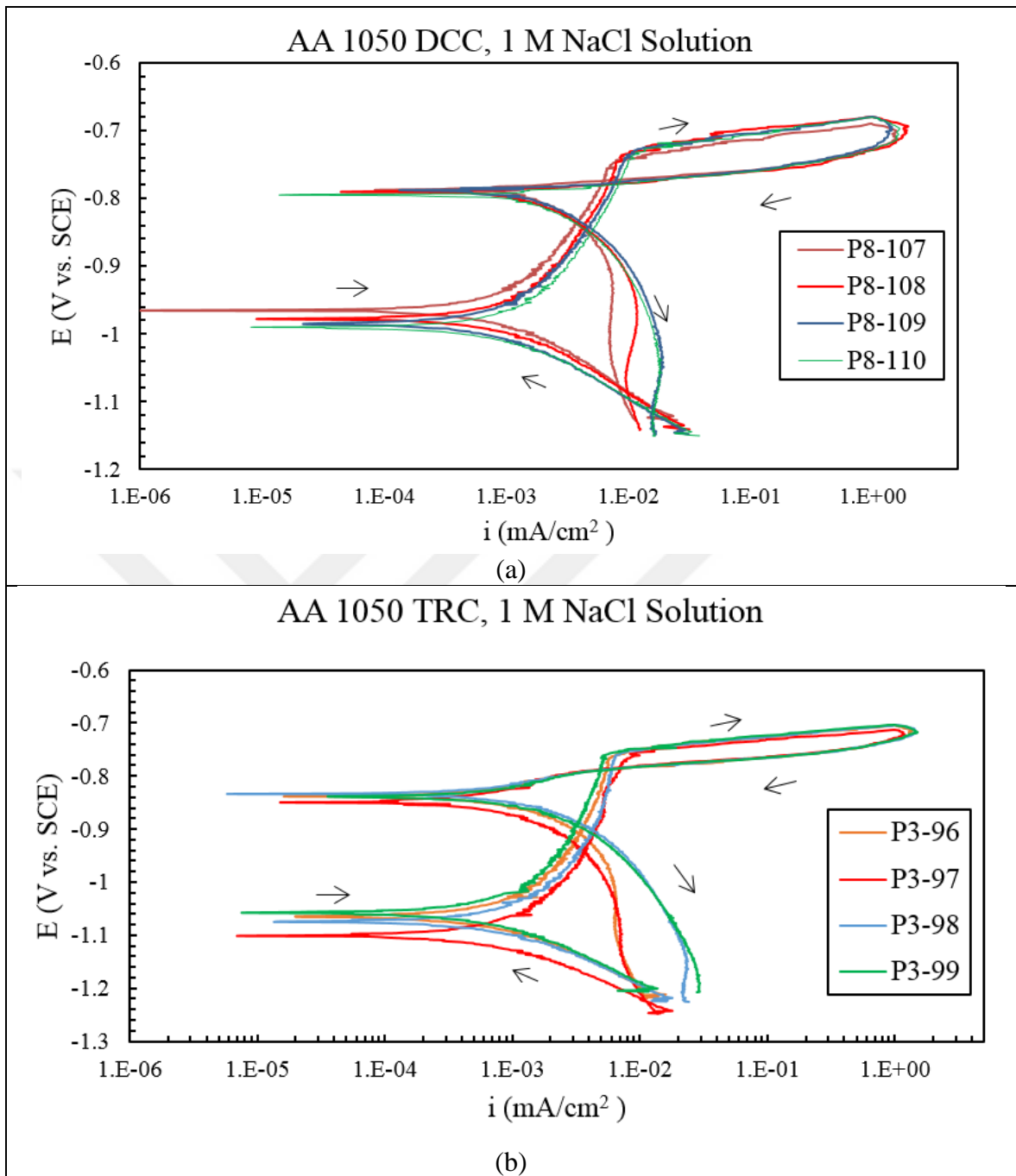


Figure 5.6. Cyclic polarization measurement results for 4 samples of AA1050 (a) DCC and (b) TRC in 1 M NaCl solution. The arrows show the sweep direction.

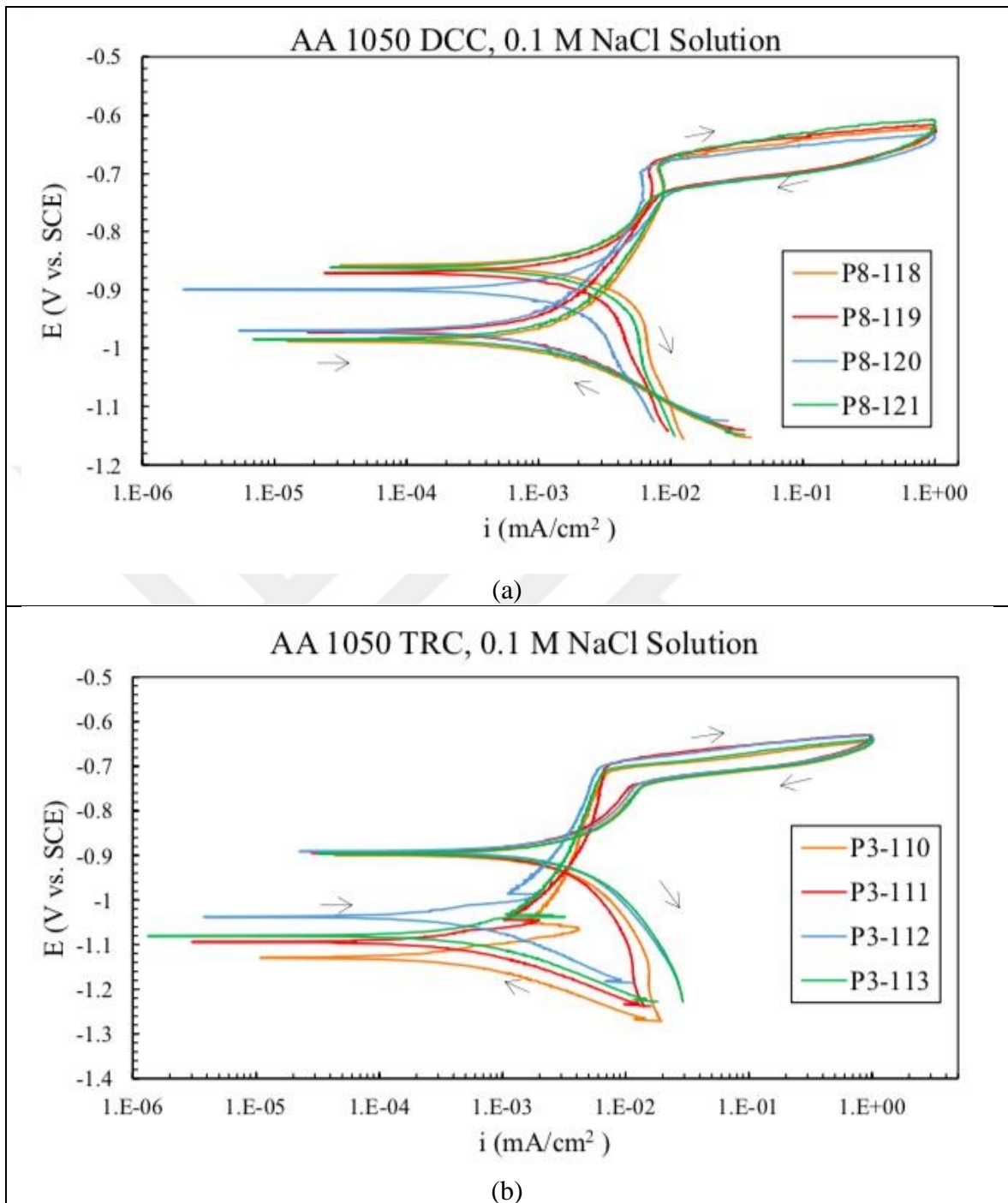


Figure 5.7. Cyclic polarization measurement results for 4 samples of AA1050 (a) DCC and (b) TRC in 0.1 M NaCl solution. The arrows show the sweep direction.

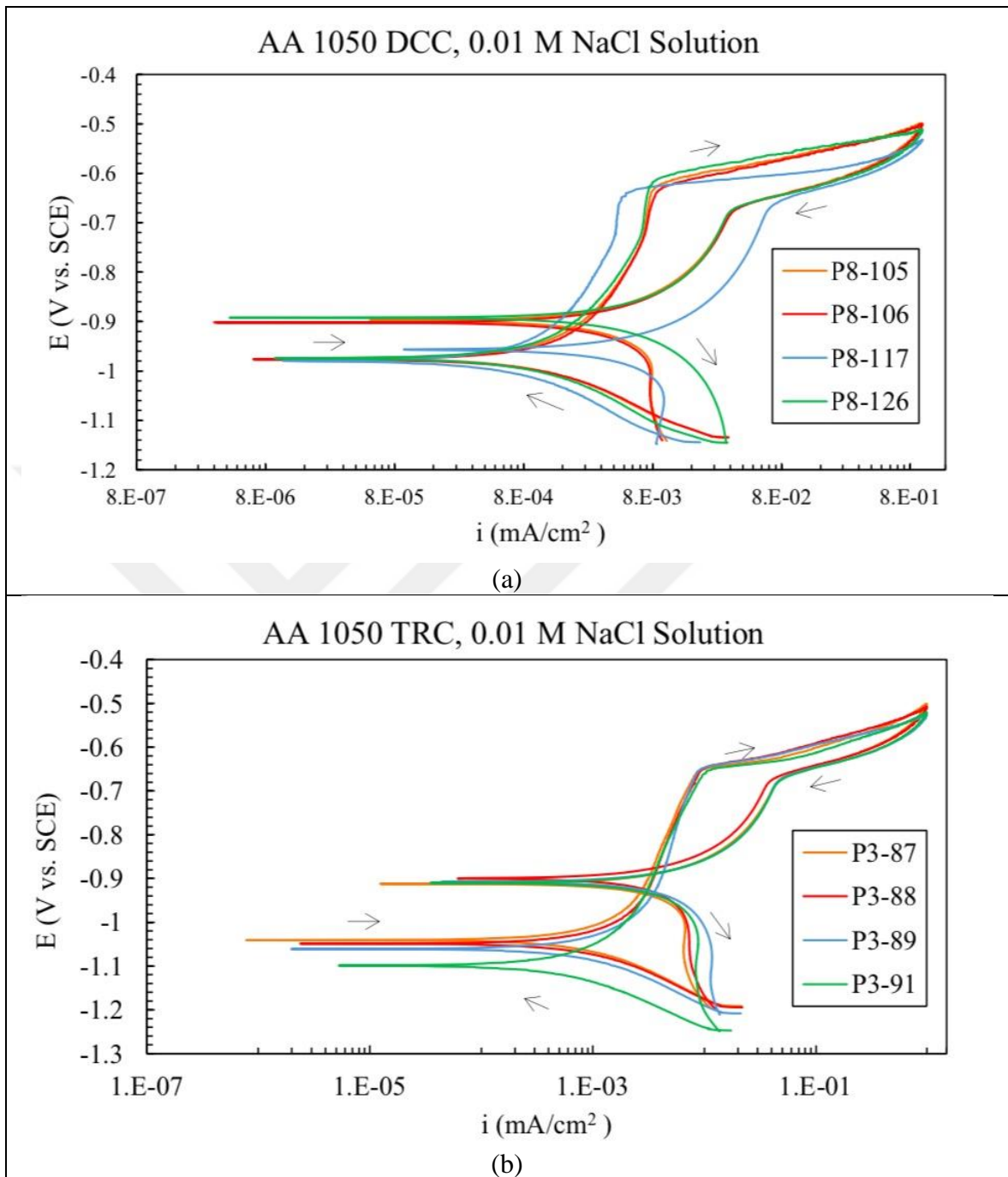


Figure 5.8. Cyclic polarization measurement results for 4 samples of AA1050 (a) DCC and (b) TRC in 0.01 M NaCl solution. The arrows show the sweep direction.

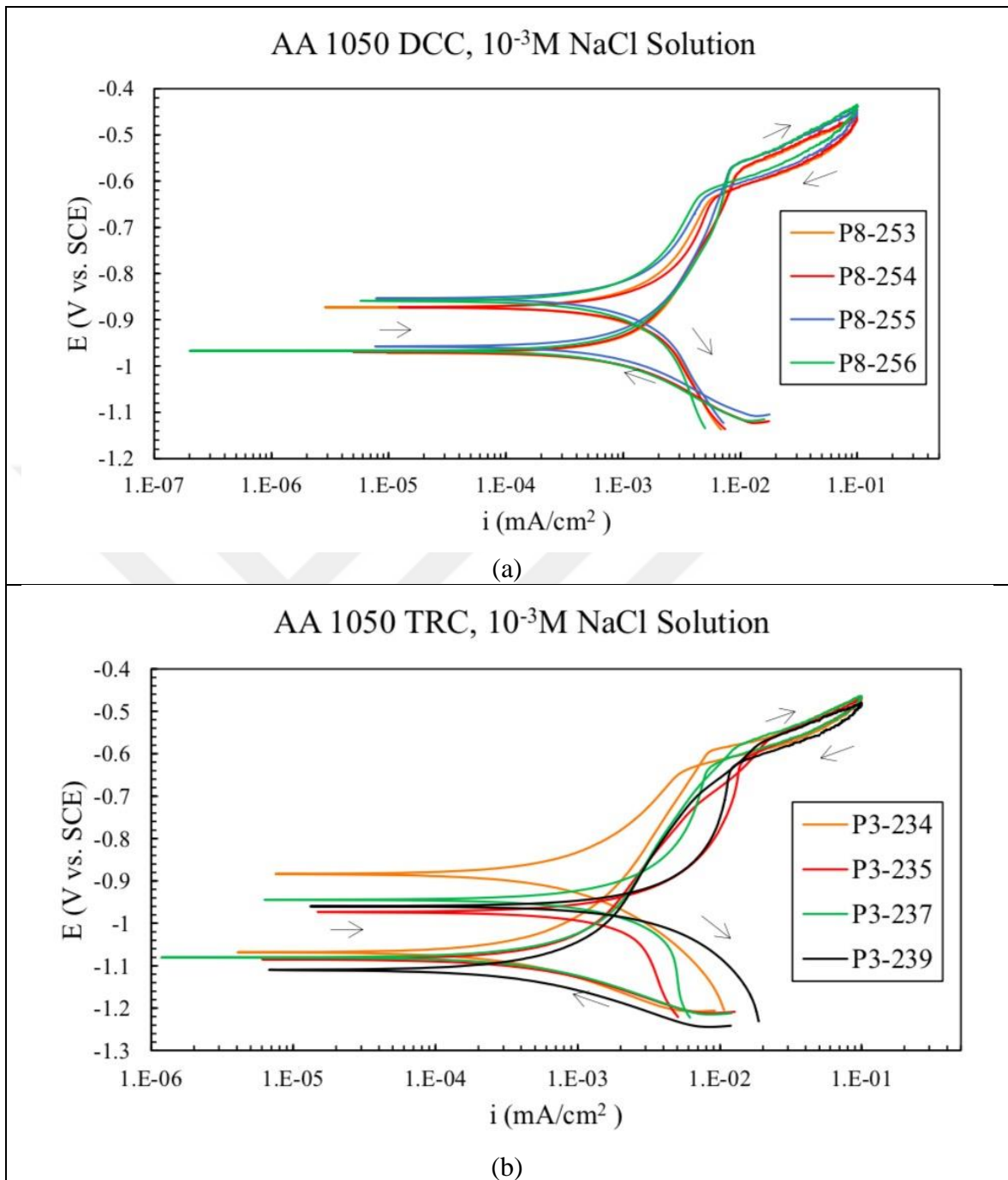


Figure 5.9. Cyclic polarization measurement results for 4 samples for AA1050 (a) DCC and (b) TRC in 0.001 M NaCl solution. The arrows show the sweep direction

The average pitting potentials of AA1050 DCC and TRC alloys determined from the CPP experiments are shown in Table 5.2. Each E_{pit} seen in the table is the average of pitting potentials determined under the same conditions. At 1 M NaCl, the pitting potentials were found as -726 mV for DCC alloy and -753 mV for TRC alloy. The largest difference between

the pitting potentials of the two production techniques was found as 27 mV at 1 M concentration. The pitting potentials for the DCC alloy at 0.1 M, 0.01 M and 0.001 M NaCl solutions are -673mV, -623mV and -564mV, respectively. The E_{pit} values for the TRC alloy are -699mV, -646mV and -570mV at the same solutions in the same order. It is seen that the pitting potentials of the DCC alloy are only slightly more positive than the pitting potentials of the TRC alloy. Furthermore, as the concentration of Cl^- ($[Cl^-]$) decreases, the E_{pit} becomes more positive for both the DCC alloy and the TRC alloys.

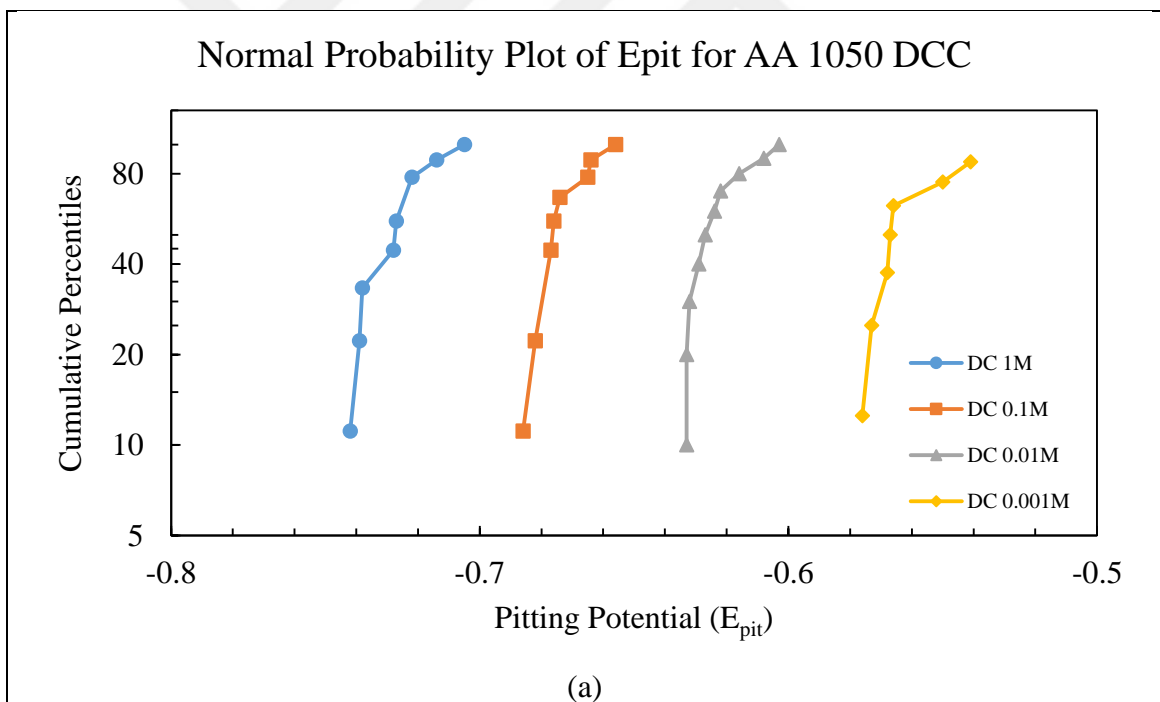
Table 5.2. Calculated average pitting potential and standard deviation value for AA1050 DCC/TRC

AA1050			
Concentration (M)	DCC	TRC	ΔE
	Pitting Potential (E_{pit}) (mV vs. SCE)		
1	-726 ± 0.0122	-753 ± 0.0044	27
0.1	-673 ± 0.0095	-699 ± 0.0059	26
0.01	-623 ± 0.0100	-646 ± 0.0025	23
0.001	-564 ± 0.0119	-570 ± 0.0097	6

Pride et al. present that the pitting potentials as -720 mV, -660 mV, 562 mV and -355 mV for 1 M, 0.1 M, 0.01 M and 0.001 M aqueous NaCl solutions, respectively [58]. These are more positive than E_{pit} values found in this study (Table 5.2) for the same concentrations. This is because Pride et al. used a high purity aluminum (99.999 percent), while AA1050 (DCC and TRC) is a commercially pure alloy with intermetallics. It is known that Fe containing intermetallics in aluminum alloys are preferential sites for pit nucleation. Comotti et al. reported the pitting potential of AA1050 in 0.6 M NaCl solution as -717mV [2]. In this thesis the average pitting potential was found for DCC and TRC alloys at 1 M is -726mV and -753mV. The results in Comotti et al. study and results in this thesis are comparable, because when the concentration is decreased the pitting potential shifts in the positive direction. On the other hand, Comotti et al. used AA1050 which was polished to 1200 grit

but the polishing was done to 2500 grit in this work. Trueba et al. found a pitting potential of -742 mV for the as received AA1050 sample in 0.6 M NaCl solution [25]. The potential that found by Trueba et al. is also comparable with the pitting potential that found in this thesis.

It has been reported in the literature that E_{pit} values shows a normal probability distribution [59][60]. Normal pitting probability graphs were also plotted and are given in Figure 5.10 for the both DCC and TRC alloys in all concentrations. It is seen that E_{pit} for both alloys exhibits normal probability distributions in all concentrations. The slight deviations from the linearity in the graphs were also seen in the plots of Pride et al. [58]. The normal probability of pitting potential is dependent to the chloride ion concentration. The normal probability graphs for the pitting potentials of the TRC alloy are more cathodic than those for the DCC alloy.



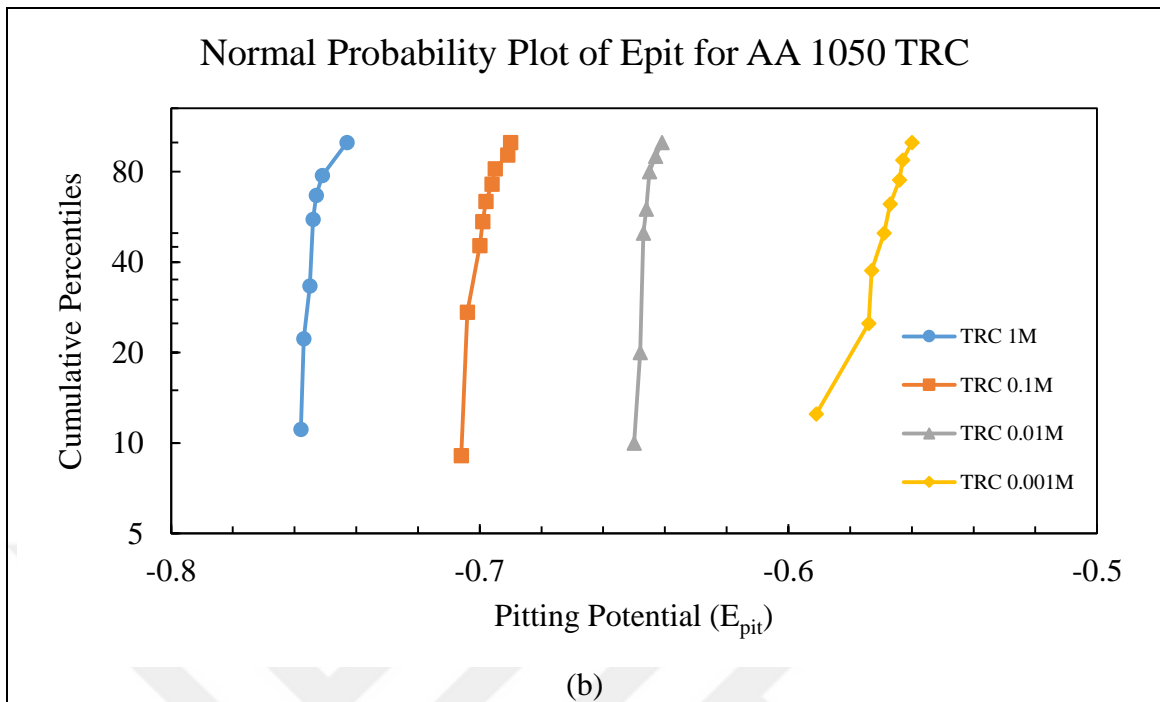


Figure 5.10. Normal distribution graph of E_{pit} data for AA1050 (a) DCC and (b) TRC in 1 M, 0.1 M, 0.01 M and 0.001 M NaCl Solution

According to the literature the pitting potential follows a logarithmic relation with the concentration of the chloride ion [58] [61] [62]. Figure 5.11 presents the concentration dependence of the pitting potentials for both the DCC alloy and the TRC alloy. As can be seen from the plots, the E_{pit} decreases with $[Cl^-]$ logarithmically. This is in agreement with the literature. The slope was as -0.053 V/decade for AA1050 DCC and -0.059 V/decade for AA1050 TRC samples.

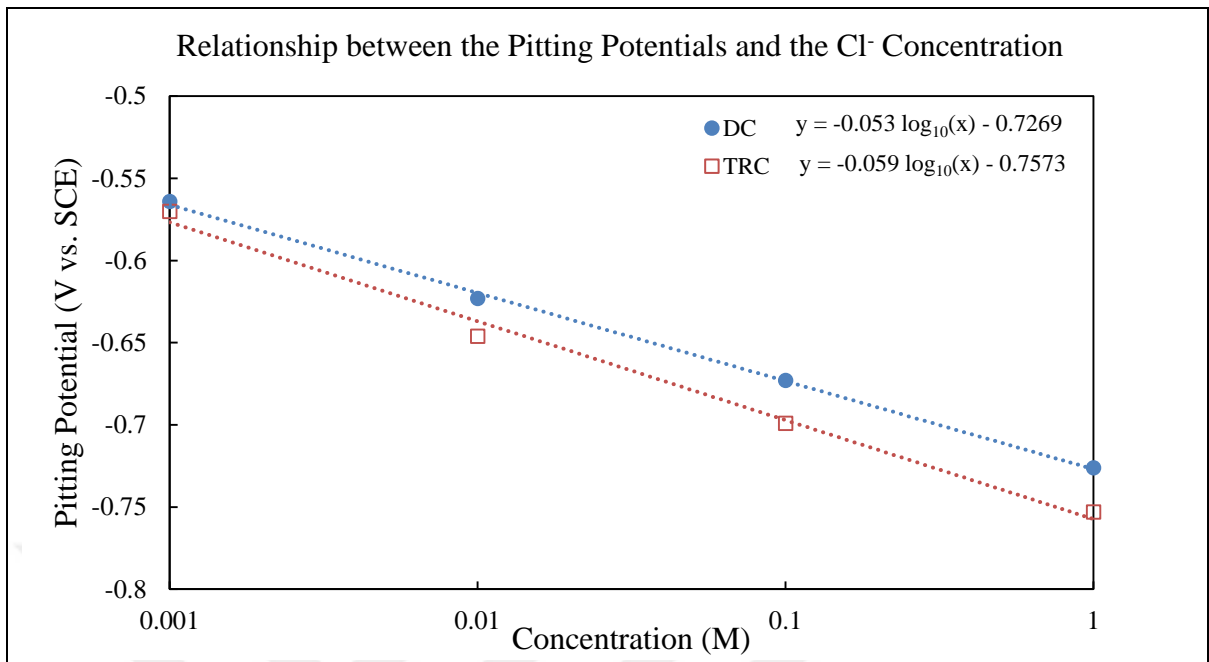


Figure 5.11. Relationship between the pitting potentials and the Cl^- concentration

Repassivation potentials and passive current densities were also calculated from the CPP curves as shown in Figure 5.5(b). The average repassivation potentials (E_{repas}) at different concentrations are tabulated in Table 5.3.

Table 5.3. Calculated repassivation potentials for AA1050 DCC and TRC alloys

AA1050		
Concentration (M)	DCC	TRC
	Repassivation Potential (E_{repas}) mV vs. SCE	
1	-776 ± 0.002	-778 ± 0.002
0.1	-761 ± 0.0049	-848 ± 0.0019
0.01	-896 ± 0.024	-887 ± 0.006
0.001	-614 ± 0.008	-614 ± 0.012

The results reveal that the repassivation potential difference between the DCC and the TRC samples is 2 mV for 1 M NaCl solution, 87 mV for 0.1 M NaCl solution, 9 mV for 0.01 M NaCl solution and there is no potential difference in 0.001 M NaCl solution. Trueba et al. found the repassivation potential of plate AA1050 as -751 mV for 0.6 M de-aerated NaCl solution with a scan rate of 10 mV/s and a vertex current density of 1×10^{-3} A/cm². [25] Although the vertex current density is the same as that in this study, they used a higher scan rate. This is likely to be the reason for their E_{repass} to be higher than those found in this study for 1 M and 0.1 M (-776 mV and -761 mV, respectively). At the same vertex current density, Comotti et al. reported a repassivation potential of -760 mV for AA1050 at 0.6 M NaCl solution with 10 mV/min.

The passive current densities for different NaCl concentration are tabulated in Table 5.4. The i_{pas} values of the alloys of the two production techniques are generally in the same order of magnitude.

Table 5.4. Calculated passive current density and standard deviation value for AA1050
DCC/TRC

AA1050		
Concentration (M)	DCC	TRC
	Passive Current Density (i_{pas}) (mA/cm²)	
1	0.0079 ± 0.0015	0.0064 ± 0.0008
0.1	0.0076 ± 0.0018	0.0055 ± 0.0013
0.01	0.0052 ± 0.0010	0.0057 ± 0.0010
0.001	0.0083 ± 0.0005	0.0141 ± 0.0046

Seen in Figure 5.12 are the representative optical micrographs of the DCC and TRC samples after CPP experiments in 1 M sodium chloride solution on 500x magnification.

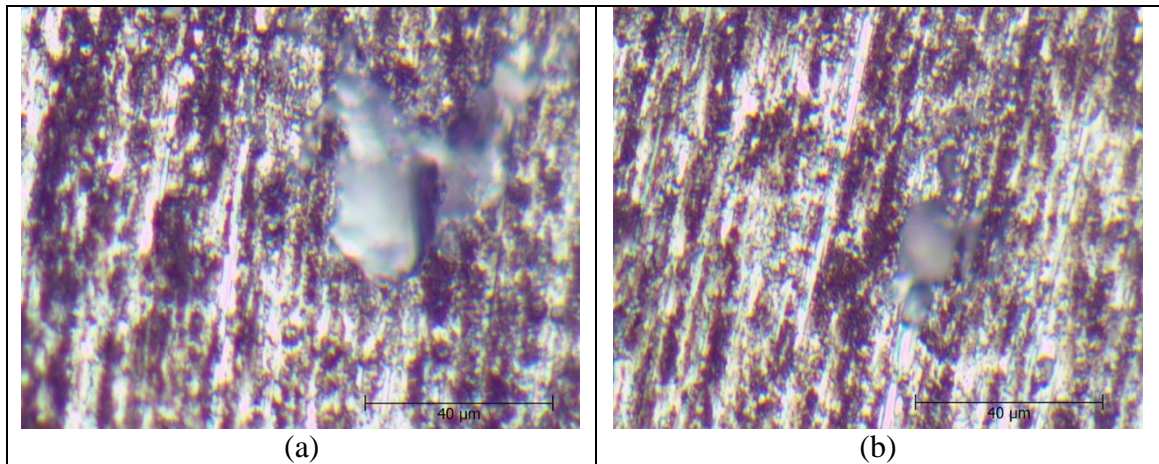


Figure 5.12. Optic microscope images for (a) DCC left side and (b) TRC right side after CPP experiments in 1 M solution

The resistance to the pitting corrosion increase when the pitting potential shifts to more positive (anodic) potentials [56]. From the CPP results, the most durable alloys between DCC and TRC is the direct chill cast alloys according to the pitting potential results.

After the CPP experiments, the region near the boundary between the electroplating tape and the test surface was checked for crevice corrosion, which is not desired. In some samples investigated, white structures (possible corrosion products) were seen near the tape boundary, which may be crevice corrosion. An example is given in Figure 5.13. To check whether the pitting potentials were affected by the crevice corrosion (that usually starts at a lower potential than pitting corrosion), further experiments were done. In these experiments, the anodic sweep was stopped once the current was seen to increase fast (above E_{pit} in Figure 5.5 (a)). No such white products were seen in these experiments (Figure 5.14). Thus, it is concluded that the pitting potential were not affected by the crevice corrosion.

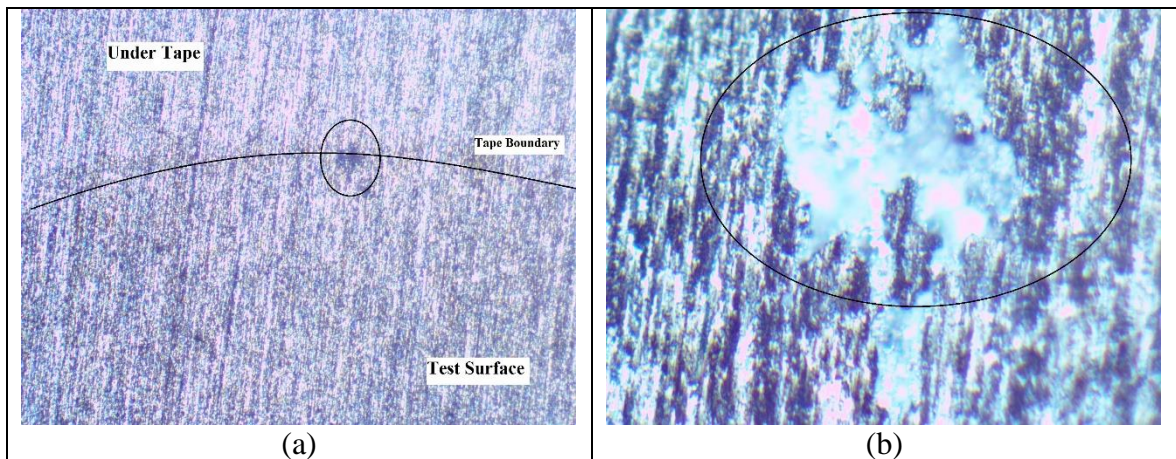


Figure 5.13. The tape boundary images (a) at 50x and white corrosion product (b) after full CPP experiments at 500x

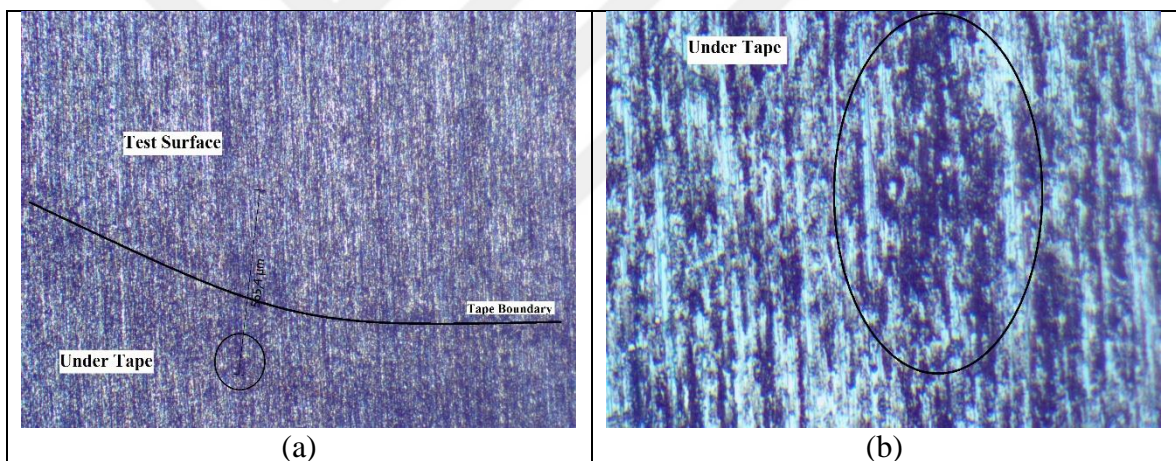


Figure 5.14. The tape boundary images (a) at 50x and surface images (b) after CPP cut experiments at 500x

The spot that shown in Figure 5.13 (b) was found under the tape boundary and it has a depth. This depth can be a crevice corrosion. On the other hand, there is no crevice corrosion (or depth) observed in Figure 5.14 (b). According to the this results, pitting potential that found from full CPP experiments are reliable but the repassivation potential results may be effected by the crevice corrosion.

5.4. RESULTS OF POTENTIOSTATIC DETERMINATION OF THE REPASSIVATION POTENTIAL MEASUREMENTS

In these experiments, the pits are formed on purpose to find the repassivation potential (E_{repas}) of the DCC and TRC AA1050 alloys. E_{repas} is the potential below which nucleated pits stop growing and passivate. In this technique, initially a high anodic potential was applied to the system to start the pitting corrosion (activation step). Then, the corrosion activity was tried to be stopped by decreasing the potential to a lower value (potentiostatic step). There are various methods for determining the repassivation potential of alloys such as ASTM F746, Tsujikawa-Hisamatsu electrochemical method (THE) and the one used by Nisancioglu et al. [43]. One difference between these methods and the one used in this work is that a new sample coupon was used in the iterative procedure used in the determination of E_{repas} .

Localized corrosion was formed by passing 60 mC of charge through the sample surface at potentials more positive than the pitting potential found by the CPP experiments. For example, for 1 M NaCl solution, 60 mC charge was passed through the surface of aluminum at -650 mV. These potentials were applied to the system for the first step of the measurement. The activation potentials for the sodium chloride concentrations are tabulated in Table 5.5. Figure 5.15 shows examples of pits that formed at the surface of the AA1050 DC cast alloy in the activation steps in different NaCl concentrations. After pits were formed, repassivation potentials were measured by applying the potential lower potentials as explained in more detail in the methodology section. The repassivation of the pits was assumed when the current density dropped below a typical current density of $1 \mu\text{A}/\text{cm}^2$.

The potential versus time and current density versus time graphs for the AA1050 DCC alloy in 1 M solution are given in Figures 5.14 and 5.15, respectively. As can be seen from Figure 5.14, there were 5 different potentials applied after the activation step (-700, -725, -750, -775, and -800 mV) to determine the repassivation potential. The corresponding current density graphs are seen in Figure 5.15 (a) and (b). Figure 5.15 (c) shows a magnified graph to better illustrate the repassivation potential range, which was between -0.775 V and -0.800 V in this case. This potential range is determined since the passive current density is below $1 \mu\text{A}/\text{cm}^2$ at -0.800 V and above $1 \mu\text{A}/\text{cm}^2$ at -0.775 V. A better illustration of the repassivation potential determination for this alloy in 1 M NaCl is given in Figure 5.16 (a).

The horizontal line in this figure show the current density limit of $1 \mu\text{A}/\text{cm}^2$. Note that the current densities change with time. Thus, an average current density was calculated for each potential neglecting the initial few minutes during which large changes occurred. In the figure, for two experiments at -0.800 V , the average current densities are below the limit of $1 \mu\text{A}/\text{cm}^2$ and for two experiments at -0.775 V , the average densities are above it. Hence, the repassivation potential range is reported as -0.775 to -0.800 V (within 25 mV). Figure 5.16 (b) show the current densities near the current density limit ($1 \mu\text{A}/\text{cm}^2$) for the TRC alloy in the same concentration. Figure 5.17 and 5.18 show the repassivation ranges for 0.1 and 0.01 M NaCl , respectively.

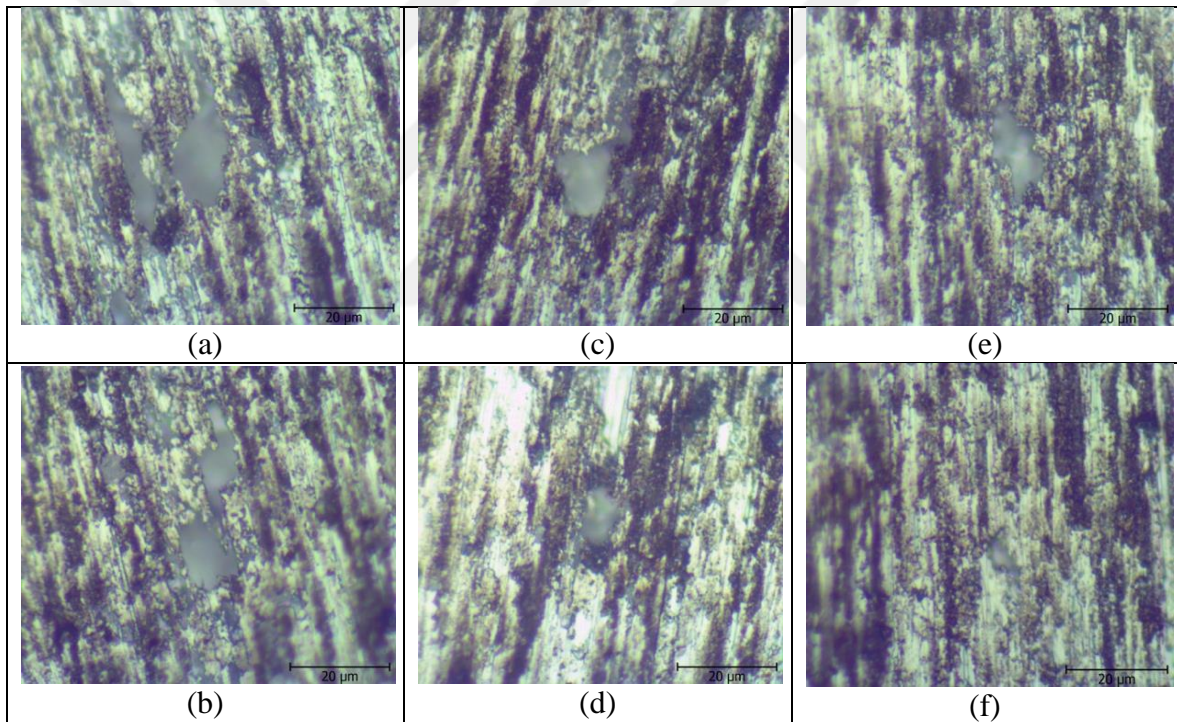


Figure 5.15. Optical examination of pits at the activation potential for AA1050 DCC alloys at (a and b) 1 M , (c and d) 0.1 M and (e and f) 0.01 M (Magnification X1000)

Table 5.5. Activation potentials for experiments for determination of repassivation potentials in different NaCl solutions

Concentration (M)	Applied Potential (mV)
1	-650
0.1	-550
0.01	-500

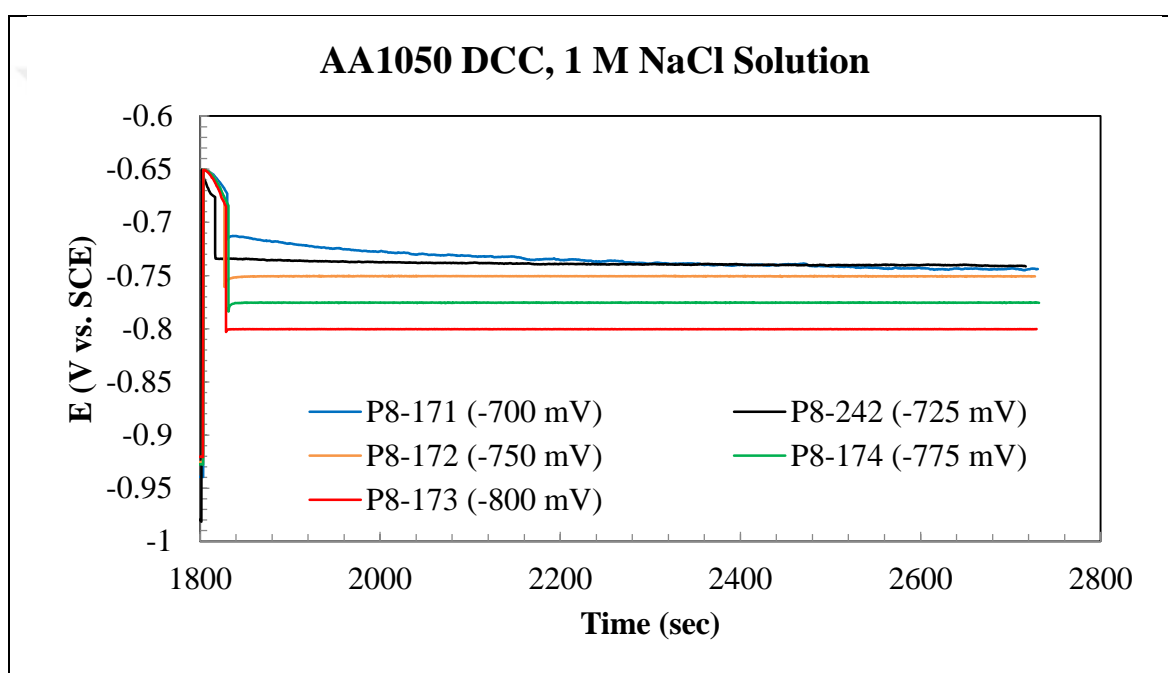
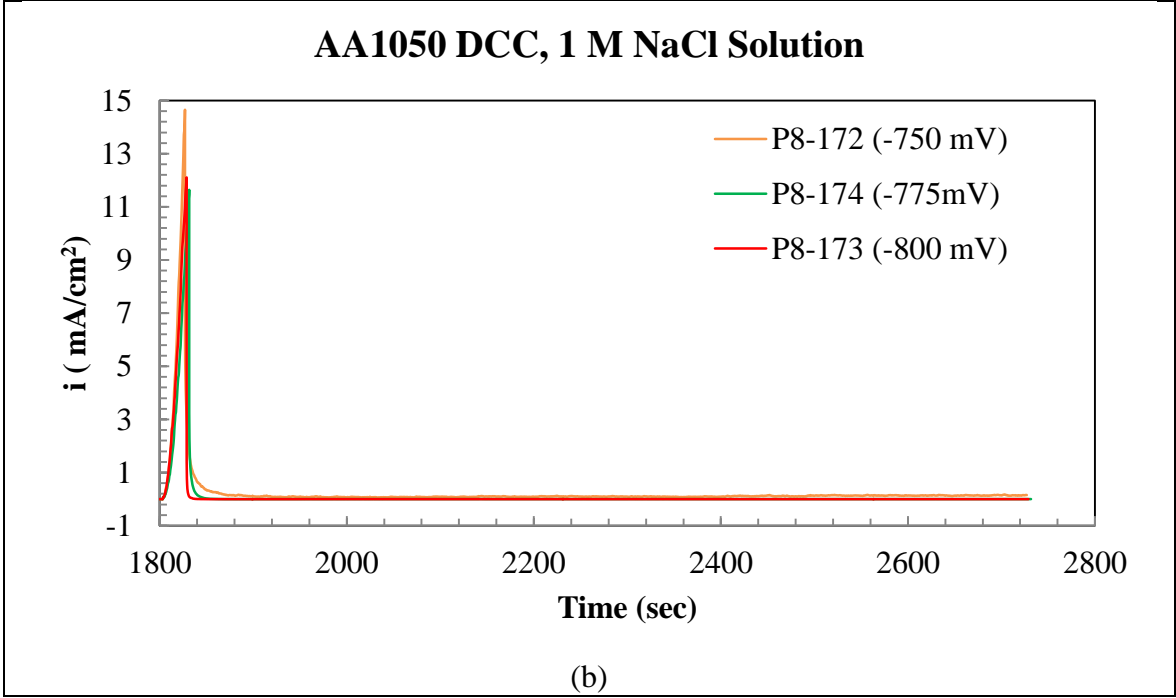
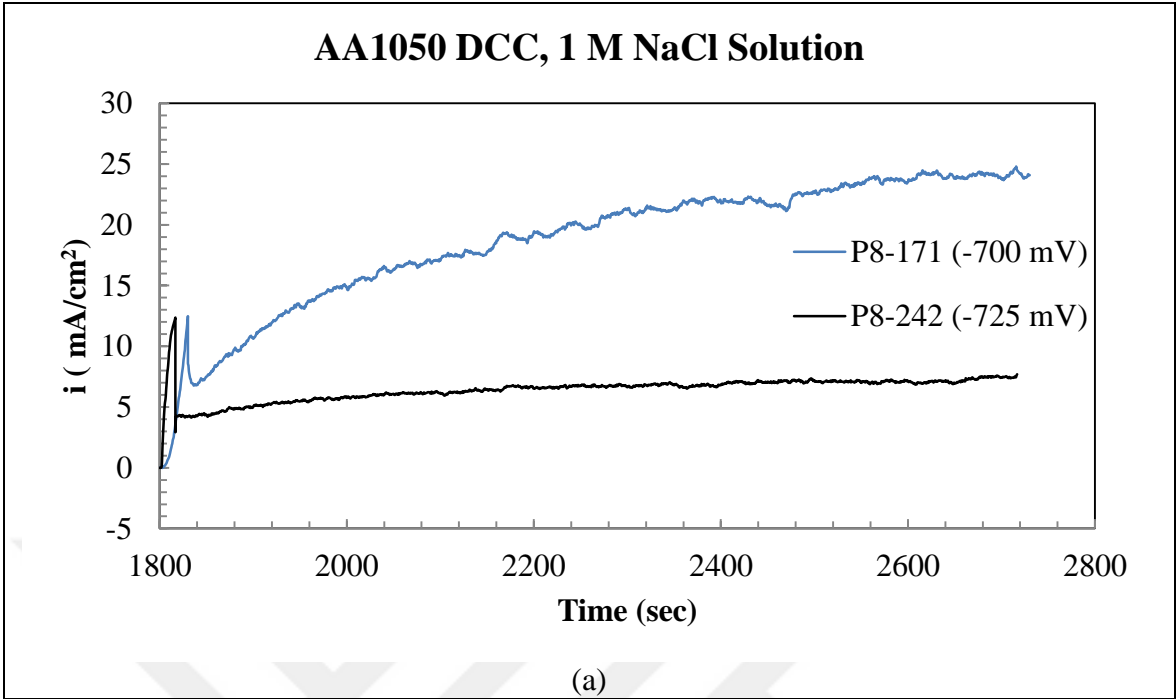


Figure 5.16. Potentiostatic determination of E_{repass} plots for DCC alloy in 1 M NaCl (Potential is corrected for potential drop in solution)



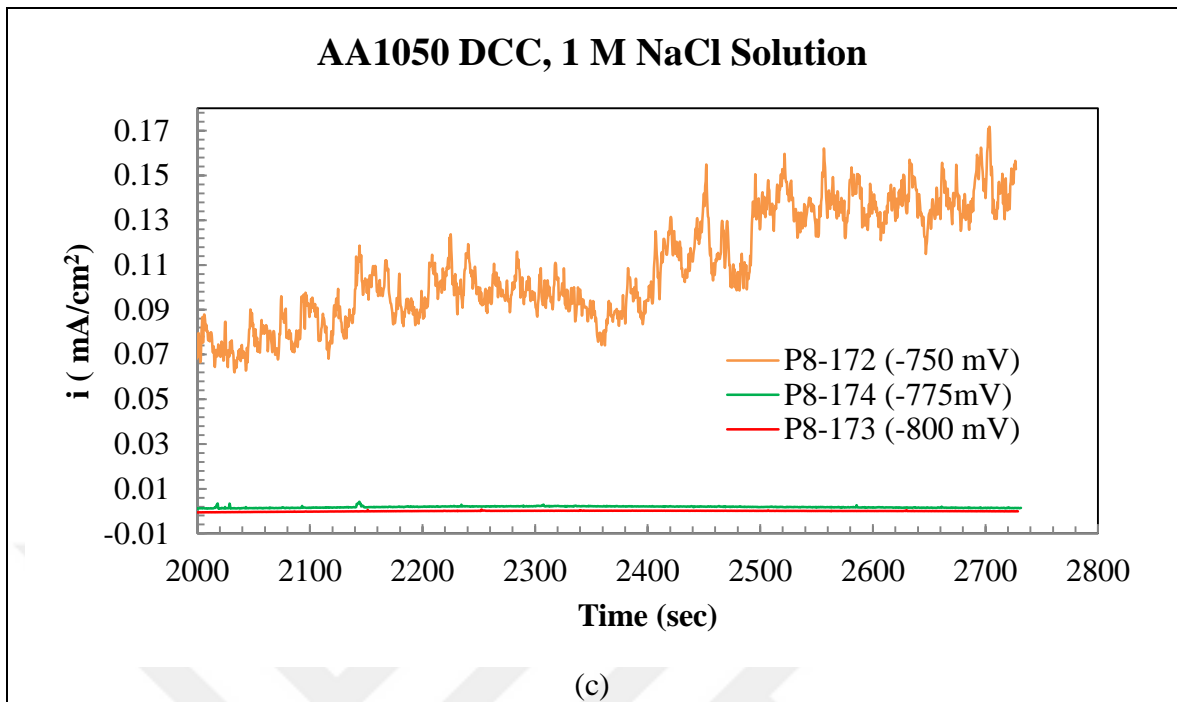


Figure 5.17. Potentiostatic determination of E_{repas} current density versus time plots for AA1050 DCC alloy in 1 M NaCl solution (a) between -700 and -725 mV, (b) between -750 and -800 mV and (c) magnified graph for between -750 and -800 mV potentials

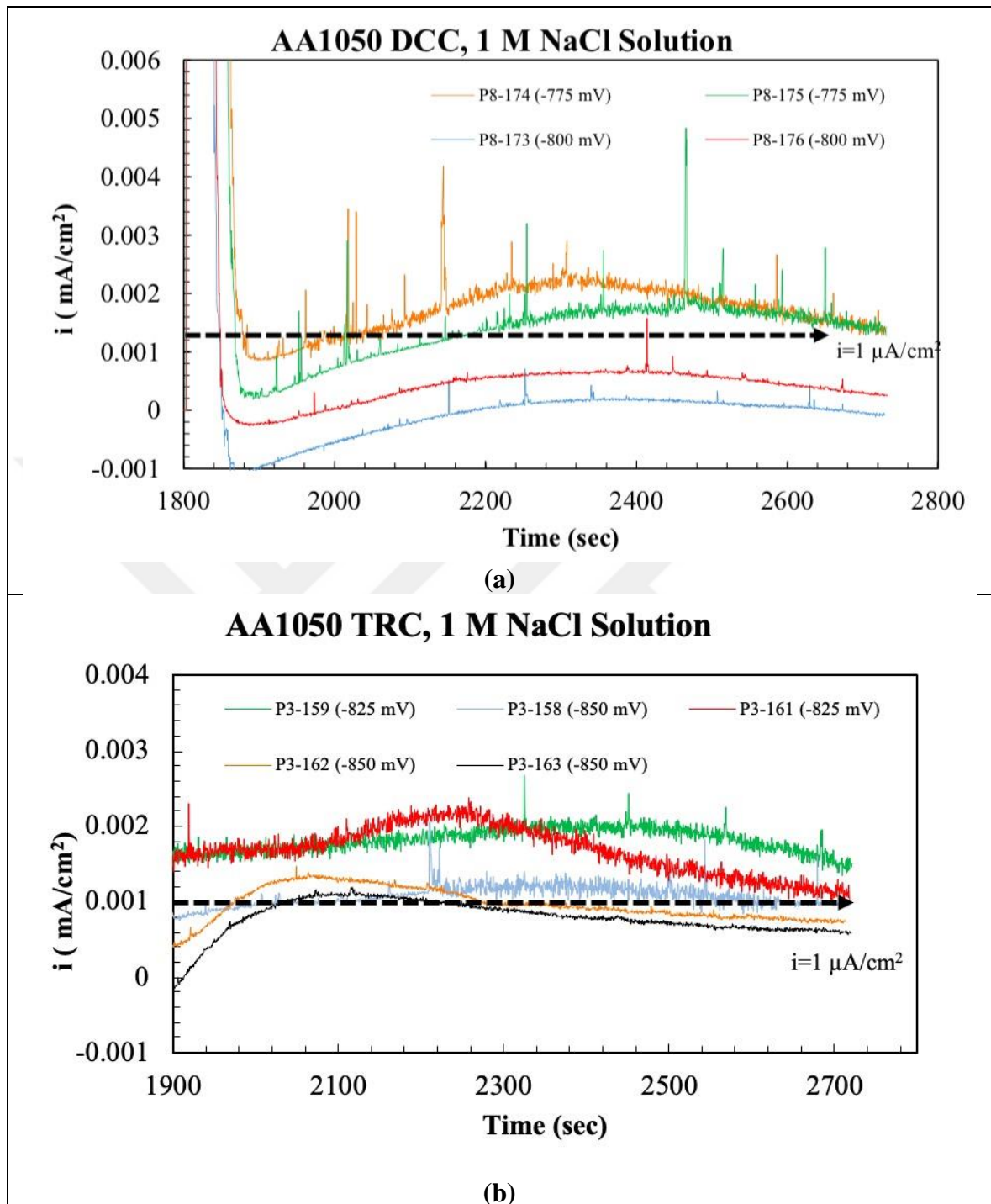


Figure 5.18. Potentiostatic determination of E_{repas} current density versus time plots in 1 M NaCl solution (a) for DCC alloys and (b) for TRC alloys (These plots shows the determination of E_{repas} interval)

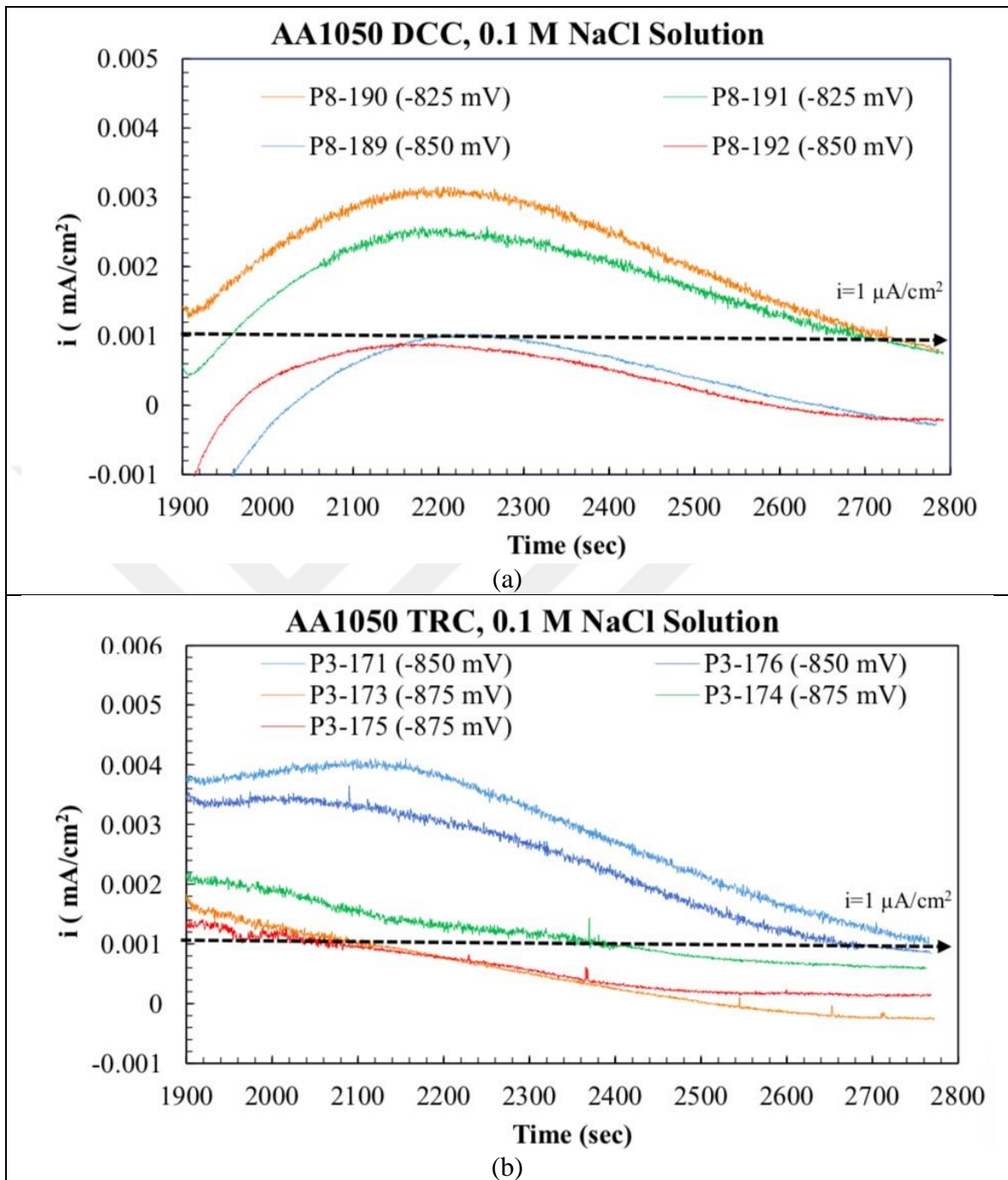


Figure 5.19. Potentiostatic determination of E_{repas} current density versus time plots in 0.1 M NaCl solution (a) for DCC alloys and (b) for TRC alloys (These plots shows the determination of E_{repas} interval)

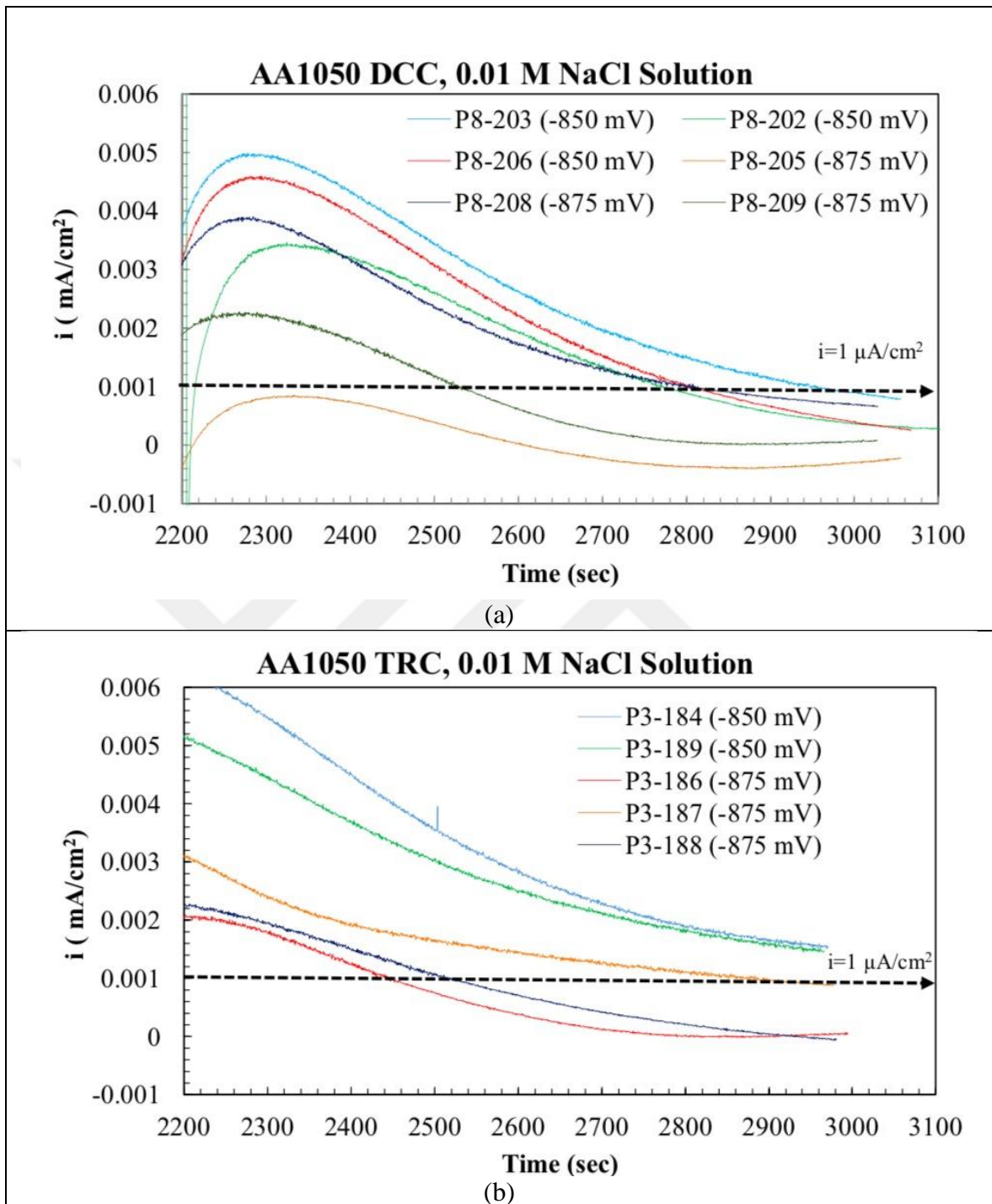


Figure 5.20. Potentiostatic determination of E_{repas} current density versus time plots in 0.01 M NaCl solution (a) for DCC alloys and (b) for TRC alloys (These plots shows the determination of E_{repas} interval)

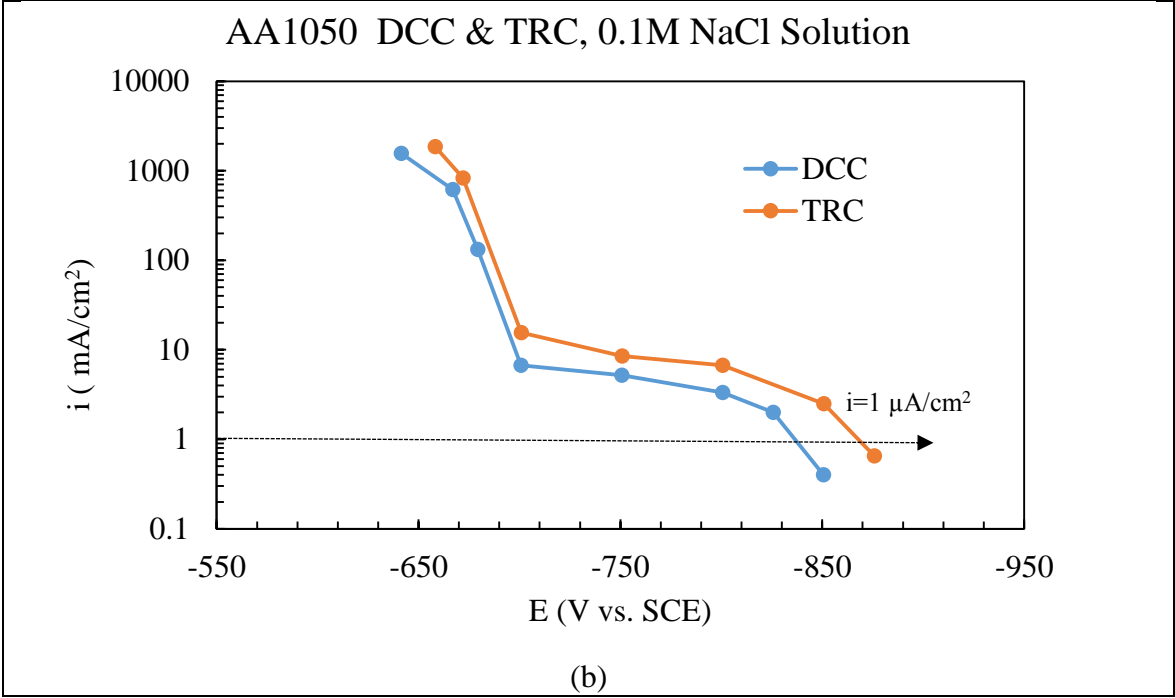
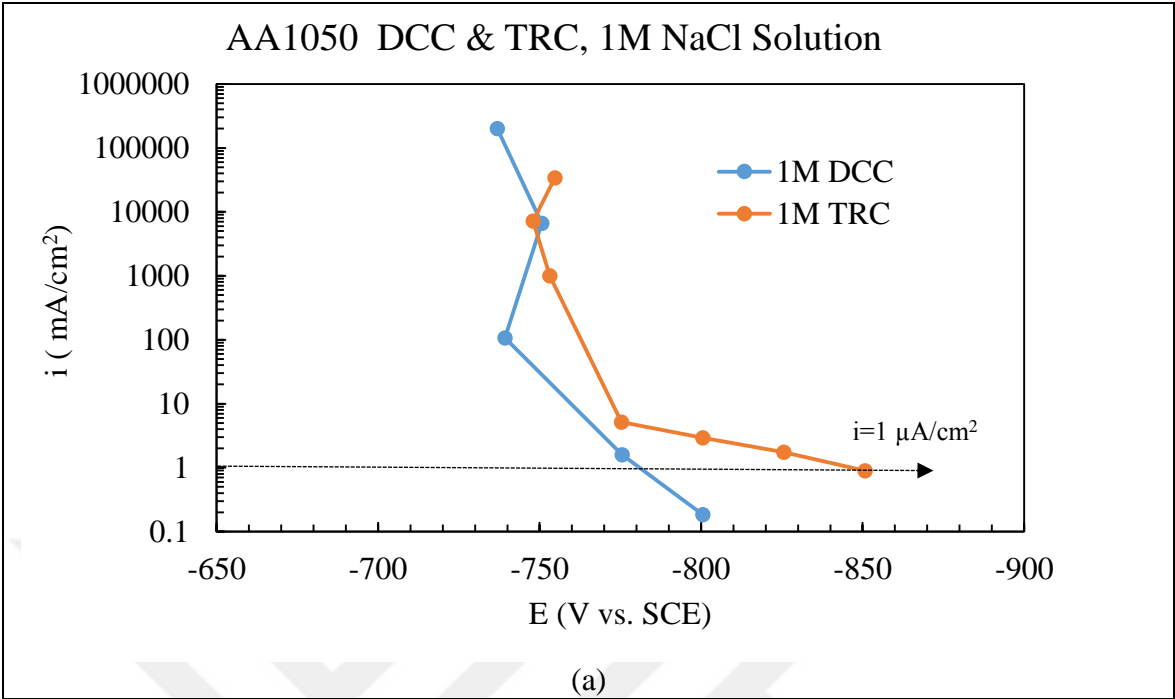
The graphs show that there are peaks on the current density data such as those seen in Figure 5.17 (a). The peaks are highest in 1 M NaCl solution for the both DCC and TRC alloys (Figure 5.17). The peaks are larger at the more positive potentials. The peak sizes are getting smaller when the chloride ion concentration decreases. These peaks are likely to be metastable pits.

The repassivation potentials are tabulated in Table 5.6. The DCC alloys have more positive repassivation potential when compared with the TRC alloys. If the midpoint of these ranges are taken as E_{repass} potential, the highest potential differences were found in 1 M NaCl solution (50 mV). The difference of midpoint potentials are getting lower when the concentrations decreases between DCC and TRC alloys. The midpoint potential differences are 25 mV in 0.1 M solution for both DCC and TRC alloys. DCC and TRC alloys have no midpoint potential difference in 0.01 M solutions. The potentials for the DCC and TRC alloys have more negative values when the chloride ion concentrations were decreased.

Table 5.6. Repassivation potential range over concentration data for AA1050 DCC and TRC samples

	AA1050 DCC	AA1050 TRC
Concentration (M)	Repassivation Potential (E_{repass}) (V vs SCE)	
1 M	$-0.775 < E_{\text{repass}} < -0.800$	$-0.825 < E_{\text{repass}} < -0.850$
0.1 M	$-0.825 < E_{\text{repass}} < -0.850$	$-0.850 < E_{\text{repass}} < -0.875$
0.01 M	$-0.850 < E_{\text{repass}} < -0.875$	$-0.850 < E_{\text{repass}} < -0.875$

Nisancioglu and Holtan passed different amounts of charge in the activation step and plotted the potential versus the current density graphs for aluminum [43]. The plots showed a steep decrease at about -840 mV. They reported this potential to be the repassivation potential of the aluminum. The reproducibility was low. To compare the results found in this work with that of Nisancioglu and Holtan, a similar plot was prepared and given in Figure 5.20. As can be seen from the figure, for both alloys in 0.1 M and 0.01 M NaCl, the current density decreases rapidly initially, then, it decreases slowly but starts to increase at a fast rate again after -825 mV. This behavior was not observed in 1 M NaCl.



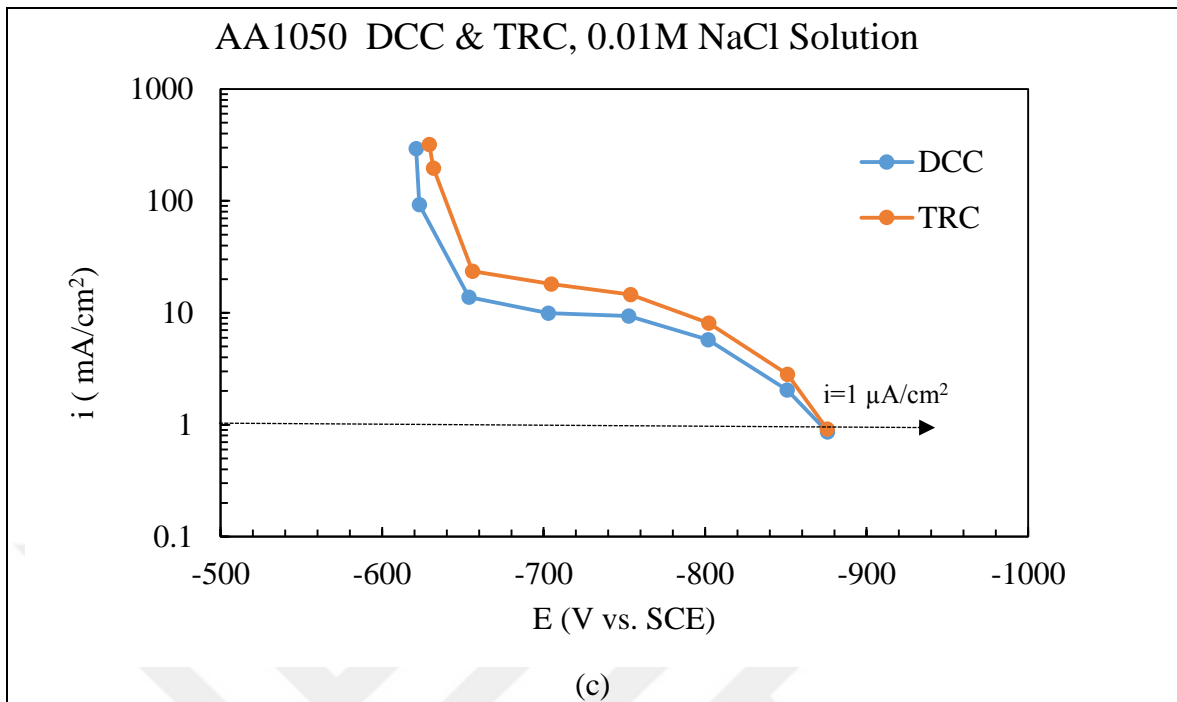


Figure 5.21. Current density versus potential graphs for DCC and TRC alloys at (a) 1 M, (b) 0.1 M and (c) 0.01 M NaCl solution

After the experiments, the regions near the boundary between the tape and the test surface were analyzed by optical microscopy for the presence of possible corrosion products (crevice corrosion indication). An example spot seen as a white structure was given in Figure 5.13 (b). Table 5.7 presents the observation results. The number of marks in each cell is the number of electrodes that are checked under those conditions. “-” mark represents no corrosion spots were observed near the tape boundary; “+” sign represents at least one is seen and “×” mark represents at least one seen under the tape near the boundary. The gray cells are indicates the E_{repas} ranges. Since there is at least one experiment in which no corrosion spot was seen for the ranges, it is unlikely that the E_{repas} determinations were effected by the crevice corrosion.

Table 5.7. Result table for analysis of controlled alloys after repassivation measurements

Concentration (M)	Potential (mV)	DCC	TRC
1	-700	-	+
	-725	+	+
	-750	×	+
	-775	-, -	-
	-800	+, -	-
	-825		-, -
	-850		+, -, -
0.1	-600	+	+
	-650	+	×
	-675	-	
	-700	+	-
	-750	+	+
	-800	+	+
	-825	-, +	
	-850	-, +	-, -
	-875		-, -, -
0.01	-550	+	+
	-600	+	-
	-650	+	-
	-700	×	-
	-750	+	-
	-800	+	-
	-825	+	
	-850	+, +, -	-, -
	-875	+, -, -	-, -, -
	-900	+	

5.5. RESULTS OF GALVANOSTAIRCASE CYCLIC POLARIZATION MEASUREMENT

The GSCP experiments is performed for obtaining the breakdown potentials (same as the pitting potential) and the protection potential of an aluminum alloys. The protection potential is the same potential of repassivation potential [63]. In contrast to the CPP and potentiostatic measurements, the current is controlled and the corresponding potential of the alloy is measured in GSCP. In this technique, the current is increased stepwise and, decreased stepwise. At each current step, an average potential is calculated. The extrapolations of these potentials give the breakdown and protection potentials. The details are presented in the methodology part.

The GSCP results are shown in Figure 5.22 for 1 M NaCl solution. Figures 5.23 and 5.24 show the results for 0.1 M and 0.01 M NaCl solutions, respectively. The graphs presented in each figure are one of the five repeated experiments for each alloy type in each concentration. The results for the remaining four measurements done under the same conditions are given in Appendix C.

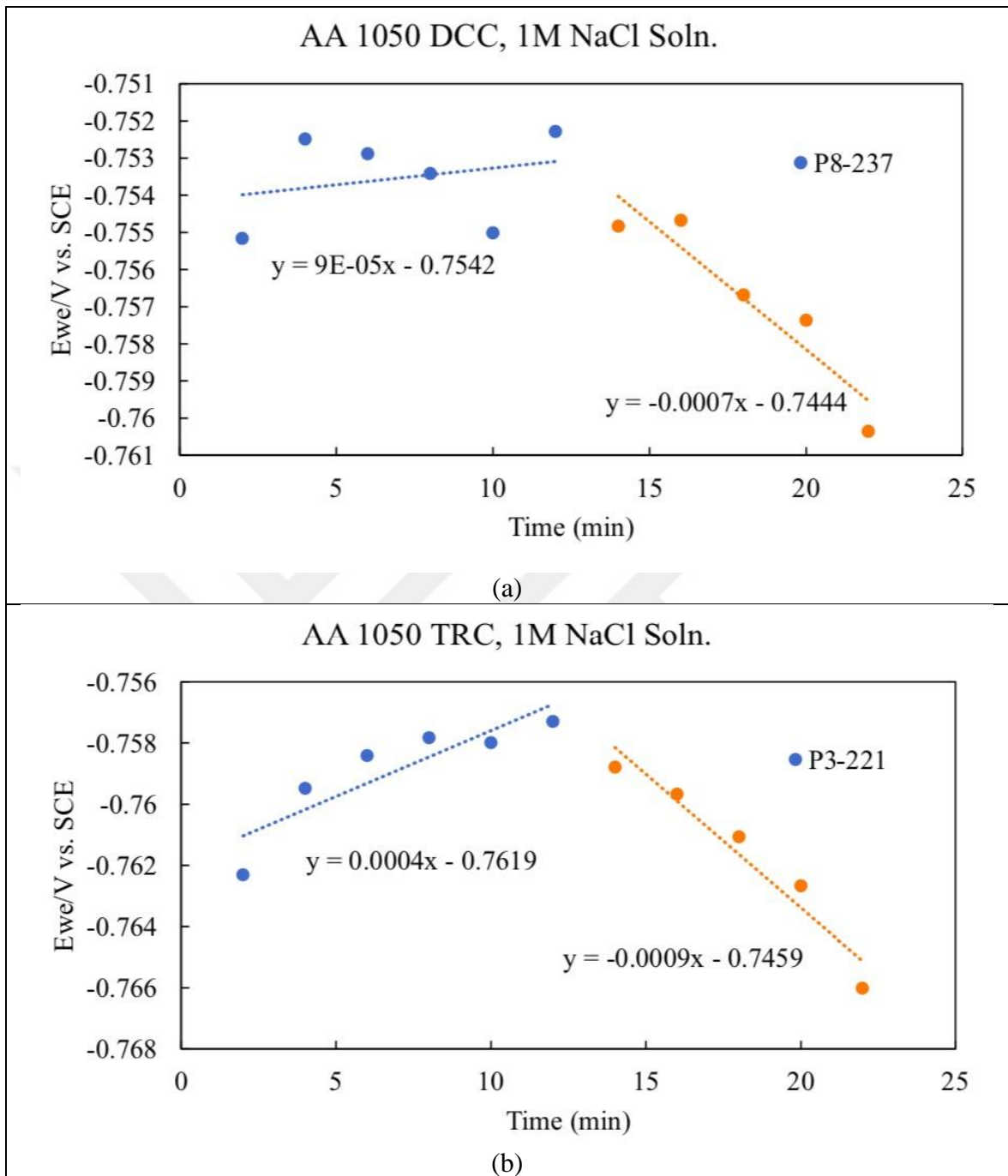


Figure 5.22. GSCP graphs for (a) the DCC alloy and (b) the TRC alloy in 1 M NaCl solution

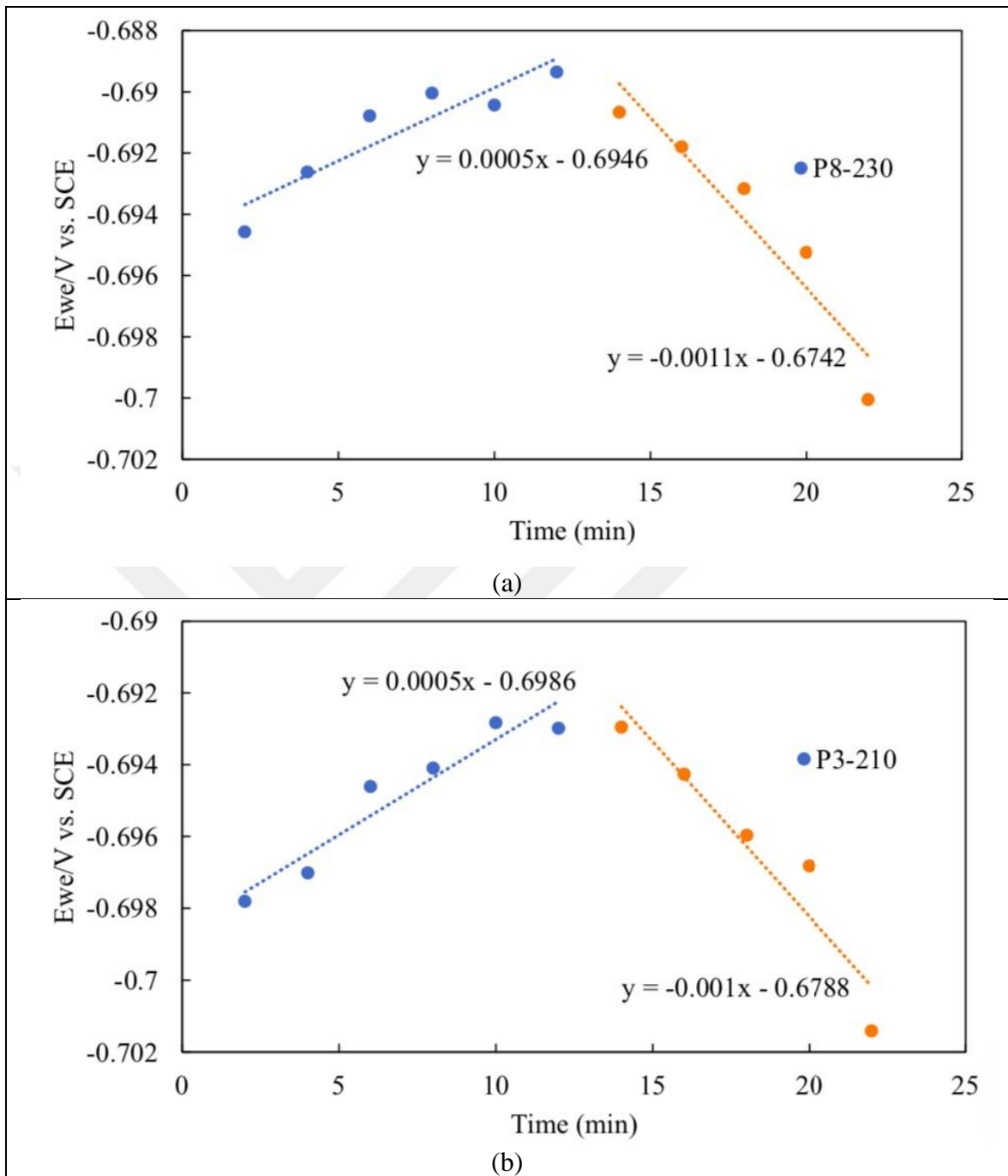


Figure 5.23. GSCP graphs for (a) the DCC alloy and (b) the TRC alloy in 0.1 M NaCl solution

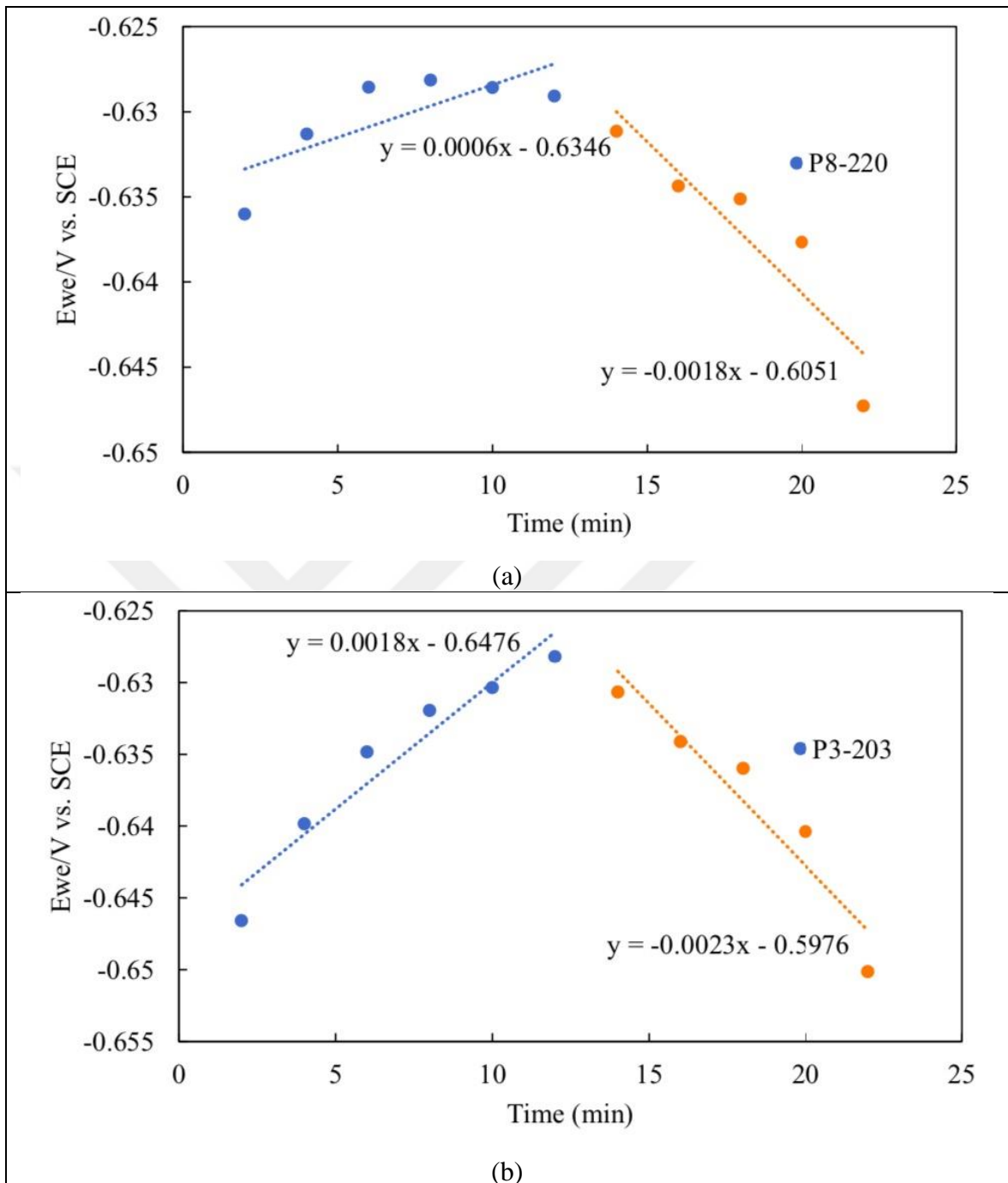


Figure 5.24. GSCP graphs for (a) the DCC alloy and (b) the TRC alloy in 0.01 M NaCl solution

The blue lines show the linear fits to the potential data obtained during the forward (increasing current) steps while the red lines show the fits for the backward (decreasing current) steps. A blue line extrapolated to 0 min gives E_b . A red line extrapolated to 24 min gives E_{prot} [44]. The average breakdown and protection potentials of the five measurements

are tabulated in Table 5.7. That is each value reported in Table 5.7 is the average of five separate measurements under the same conditions.

Table 5.8. Breakdown (E_b) and protection (E_{prot}) potentials for DCC and TRC alloys from GSCP experiments with different NaCl concentrations

AA1050				
Concentration (M)	Breakdown Potential (E_b) (mV vs. SCE)		Protection Potential (E_{prot}) (mV vs. SCE)	
	DCC	TRC	DCC	TRC
1	-752 ± 0.002	-759 ± 0.001	-756 ± 0.001	-761 ± 0.002
0.1	-692 ± 0.004	-699 ± 0.004	-698 ± 0.002	-702 ± 0.002
0.01	-631 ± 0.012	-648 ± 0.003	-645 ± 0.005	-649 ± 0.002

The breakdown potentials of the DCC alloy are very close to those of the TRC alloy at all concentrations. The largest difference is 17 mV at 0.01 M NaCl, the DCC alloy exhibiting the higher breakdown potential. The protection potentials of the two alloys are also very close. The breakdown potentials of both alloys decreased with a decrease in concentration. Note that, for the alloys, E_b and E_{prot} are close to each other in GSCP technique (Table 5.8).

So far the critical potentials were determined by different electrochemical tests (CPP, potentiostatic determination of E_{repas} and GSCP). These are compared in Figure 5.25 for E_{pit} (a) and E_{repas} (b).

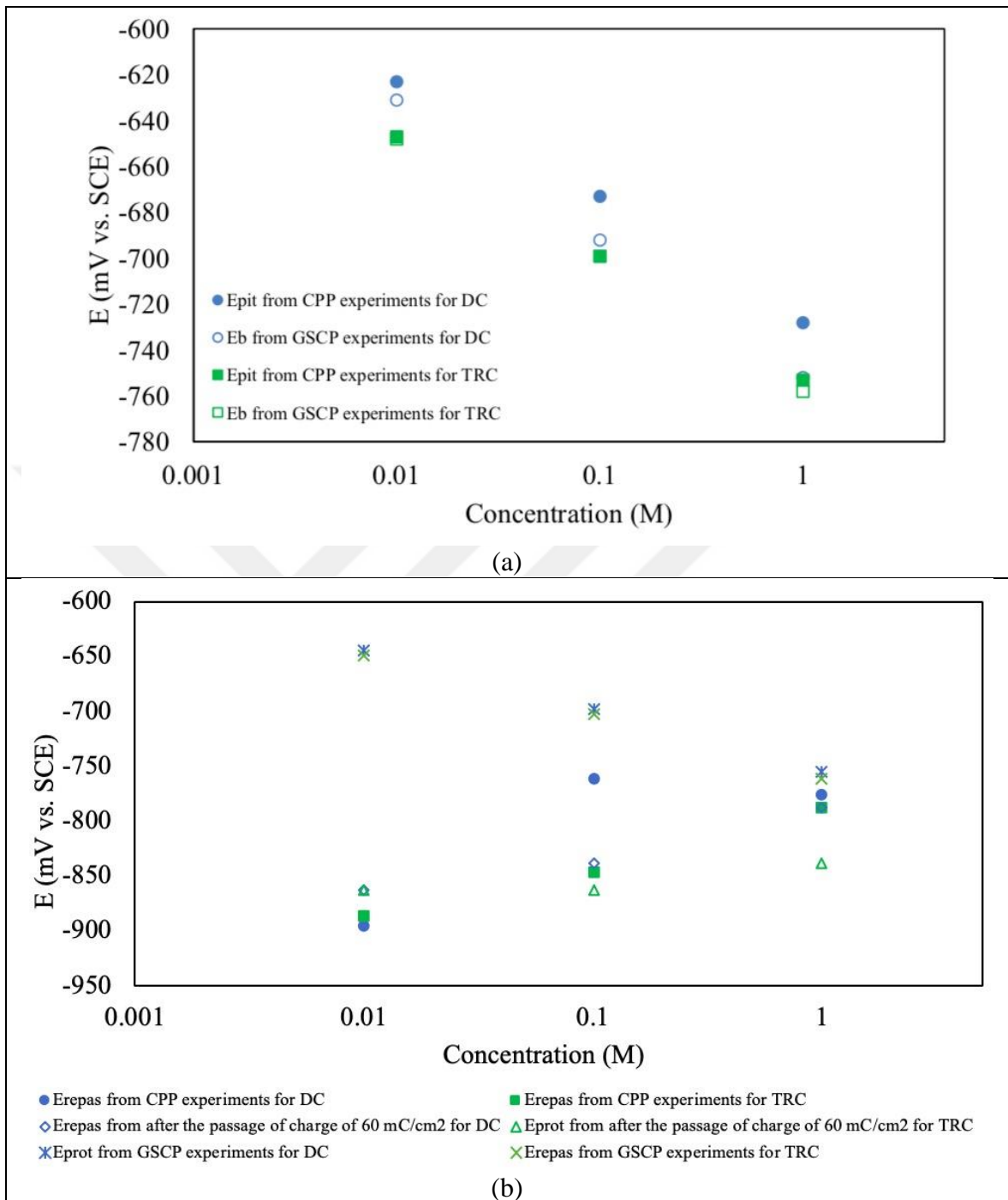


Figure 5.25. Comparison of critical potential determined by the different method (a) for pitting potential and (b) for repassivation potential

From Figure 5.25 (a), it is seen that, for the DCC alloy, the pitting potentials found by the CPP and GSCP techniques are close to each other with the largest difference being at 1 M as 26 mV. For the TRC alloy, the two techniques resulted in closer E_b potentials. However, it should be emphasized that the results of CPP tests depend on the parameters such the scan

rate and the vertex current density. Figure 5.25 (b) illustrates the repassivation results. There is a wide scatter in the values determined by the different techniques, particularly at 0.01 M and 0.1 M NaCl. The result of the potentiostatic method may be affected by the amount of charge passed in the activation step and, also, from the limit current density accepted for the passivation ($1 \mu\text{A}/\text{cm}^2$ in this study). The most noble E_{repass} values were found by the GSCP method.

The presence of possible corrosion products near the tape boundary region was also checked after the GSCP experiments with the optical microscope. Table 5.9 summarizes the results. White corrosion products were seen for experiments in 1 M concentration. However, in lower concentrations, no such products were seen near the tape or under the tape. Thus, the results of the GSCP experiments were not affected by crevice corrosion in 0.1 M and 0.001 M NaCl solutions.

Table 5.9. Result table for analysis of controlled alloys after GSCP measurements

Concentration	DCC	TRC
1 M	-, +, -, -, +	+, +, -, +, -
0.1 M	-, -, -	-, -, -
0.01 M	-, -, -	-, -, -

5.6. RESULTS OF METASTABLE PITTING MEASUREMENTS

Metastable pitting measurements were done to compare the resistance to the pitting corrosion of the AA1050 DCC alloy with that of the AA1050 TRC alloy. Metastable pitting is studied due to their relation to stable pitting [58,64–68]. For instance, Williams et al. expressed the probability of formation of a stable pit in stainless steels 316L and 304L as the multiplication of the probability of formation of a metastable pit and the probability of transition from metastable pitting to stable pitting [65]. Based on their studies with AA7075-T651, Gupta et al. reported that the metastable pitting rate provided a quantitative metric for

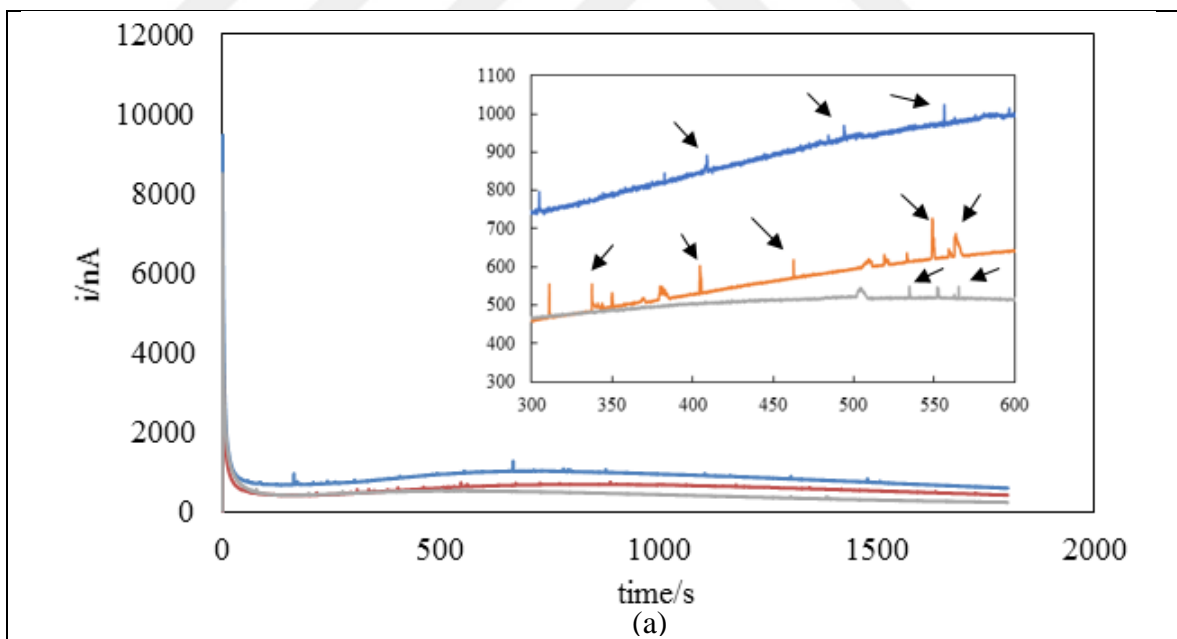
pitting corrosion [68]. An important point in this measurement is to minimize the background passive current value so that metastable pitting events can be detected [58]. This problem was overcome by using a smaller test surface area [67],[58], [69], [70]. The surface area in the studies by Pride et al., Gupta et al. and Cavanaugh et al. was 0.01 cm² [67], [58], [69]. Trueman used a test surface area of 0.025 cm². In the present study, 0.03 cm² (circular, 2 mm in diameter) surface area was used. Rather than comparing the metastable pitting rates of the two alloys at the same applied potential, the rates were compared at a constant underpotential below E_{pit} . Such an approach was suggested and used by Gupta et al [67]. The measurements were done 50 mV, 75 mV and 100 mV below E_{pit} of each alloy in the test solution. As mentioned in the methodology part, 0.01 M and 0.001 M NaCl solutions were used to keep the number of metastable pitting events smaller. The pitting potentials in the solutions had been found from the CPP experiments discussed before. The pitting potentials and the applied potentials for each type of alloy for both concentrations are given in Table 5.10.

Table 5.10. The pitting potential and the applied potential for metastable pitting experiments

Pitting Potential (E_{pit})	DCC	DCC	TRC	TRC
	0.01 M (-623 mV)	0.001 M (-564 mV)	0.01 M (-646 mV)	0.001 M (-570 mV)
	mV			
-50 mV	-673	-614	-696	-620
-75 mV	-698	-639	-721	-645
-100 mV	-723	-664	-746	-670

Figure 5.26 presents the current versus time plots for the DCC alloy in 0.01 M NaCl solution. The three curves in Figure 5.24 (a) are the repeats under the same conditions (but each with a new coupon). In this case, the potential was 50 mV below the pitting potential of the alloy in 0.01 M NaCl solution. The results for 75 mV and 100 mV below E_{pit} are given in Figure 5.26 (b) and (c), respectively. Again, the three curves seen in each were obtained

from the experiments under the same conditions. The insets show expanded views of the current-time plots to illustrate the metastable pitting events more clearly. Metastable pits are shown by arrows. Figure 5.27 present the results for the TRC alloy in the same concentration. Figures 5.28 and 5.29 show the results of the DCC alloy and TRC alloy in 0.001 M solution, respectively. As can be seen from the figures, at all underpotentials (50 mV, 75 mV, and 100 mV), the current decreased rapidly at the beginning of the experiment. This behavior was also observed by Gupta for pure aluminum and some aluminum alloys and by Speckert and Burstein for an Al-0.03Ti binary alloy [26,58,67,68]. In most cases, the current reached a local minimum value at about 140 seconds and, then, started to increase gradually. This was, then, followed by a gradual decrease. Similar behavior was also reported by Ralston et al. [71]. The number of metastable pits generally decreased when the applied potential decreased. A decrease in the rate of metastable pitting with the potential is also reported in the literature [67].



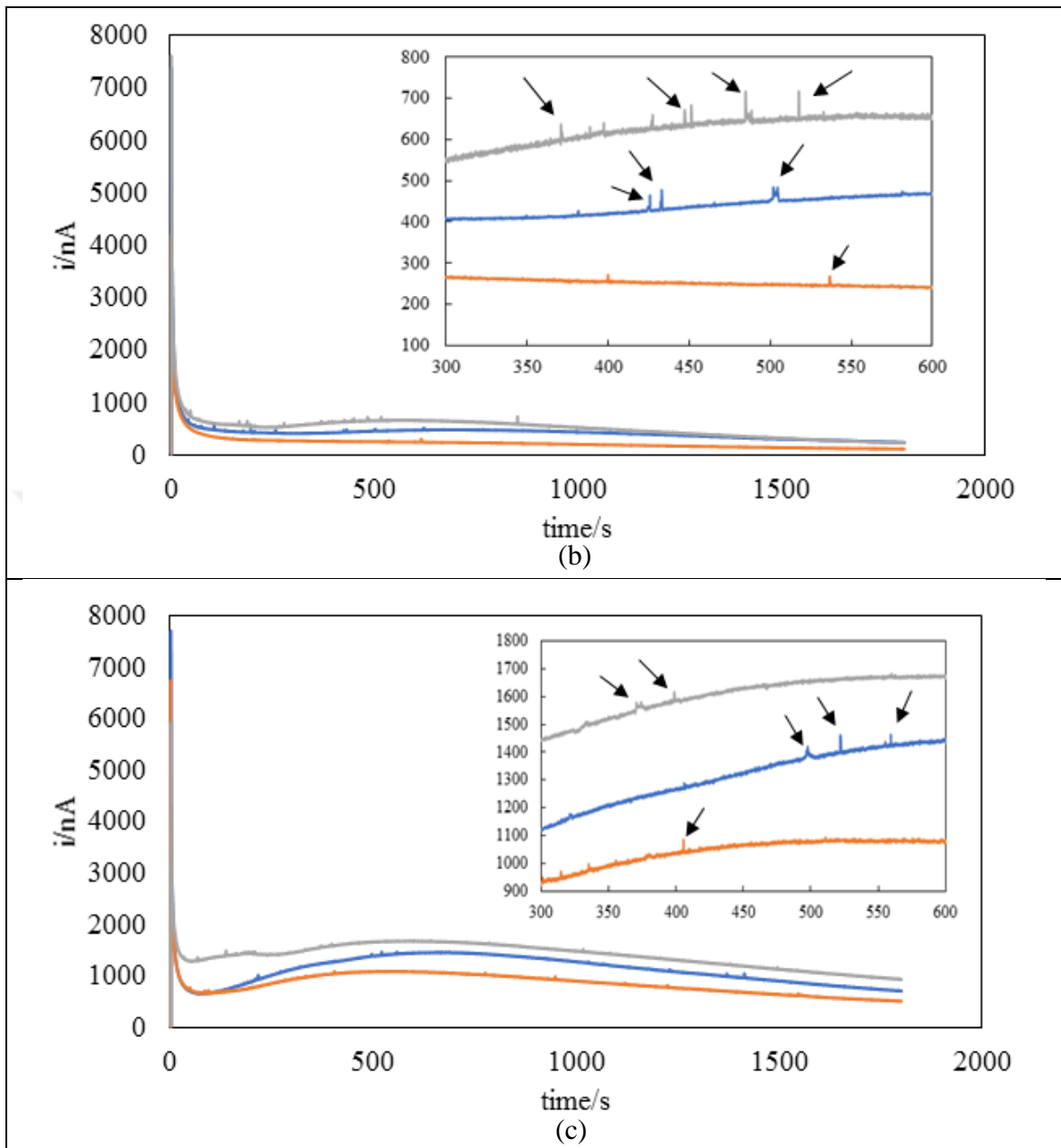
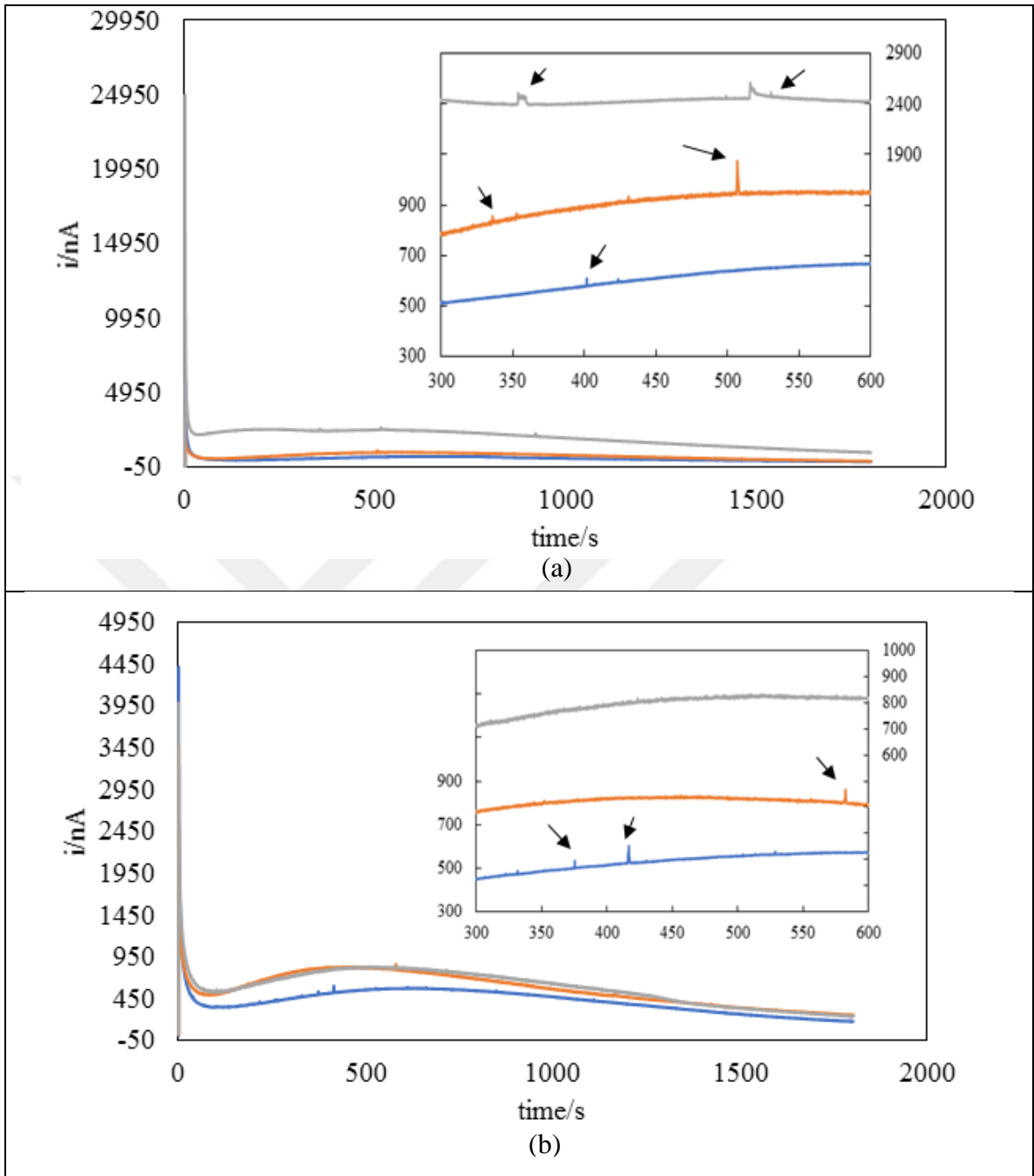


Figure 5.26. Metastable pitting graphs for DCC alloys at 0.01M NaCl test solution for (a) 50 mV, (b) 75 mV and (c) 100 mV below the pitting potential. For better representation magnified data between 300 to 600 seconds were given.



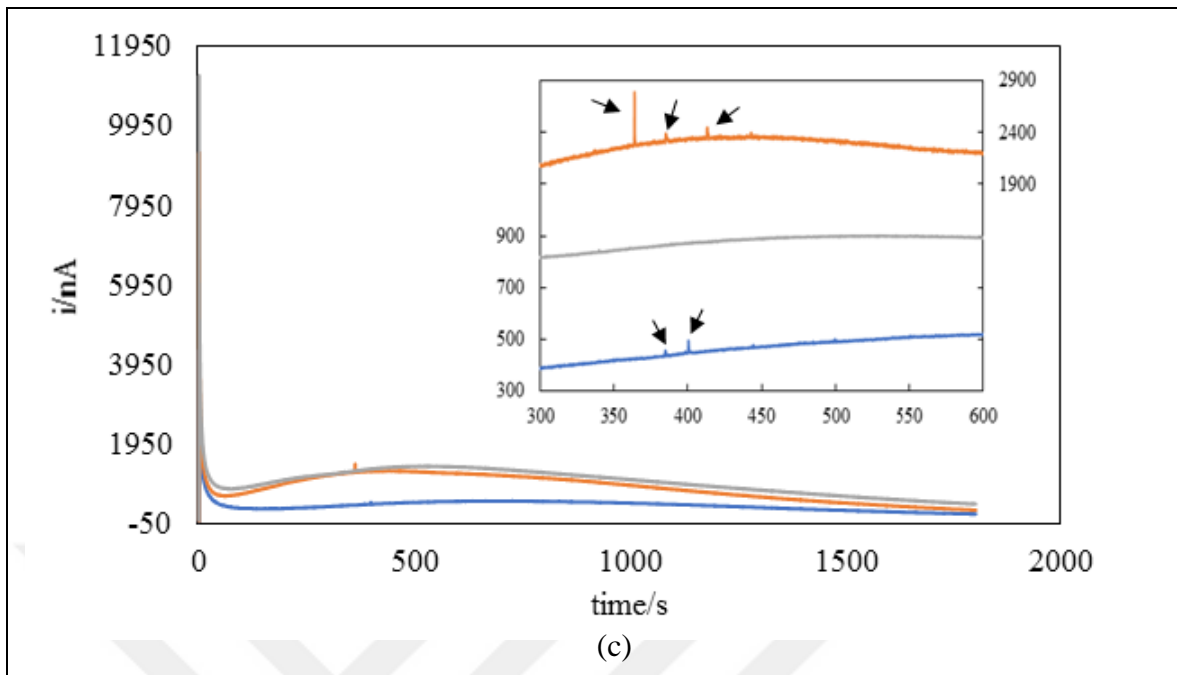
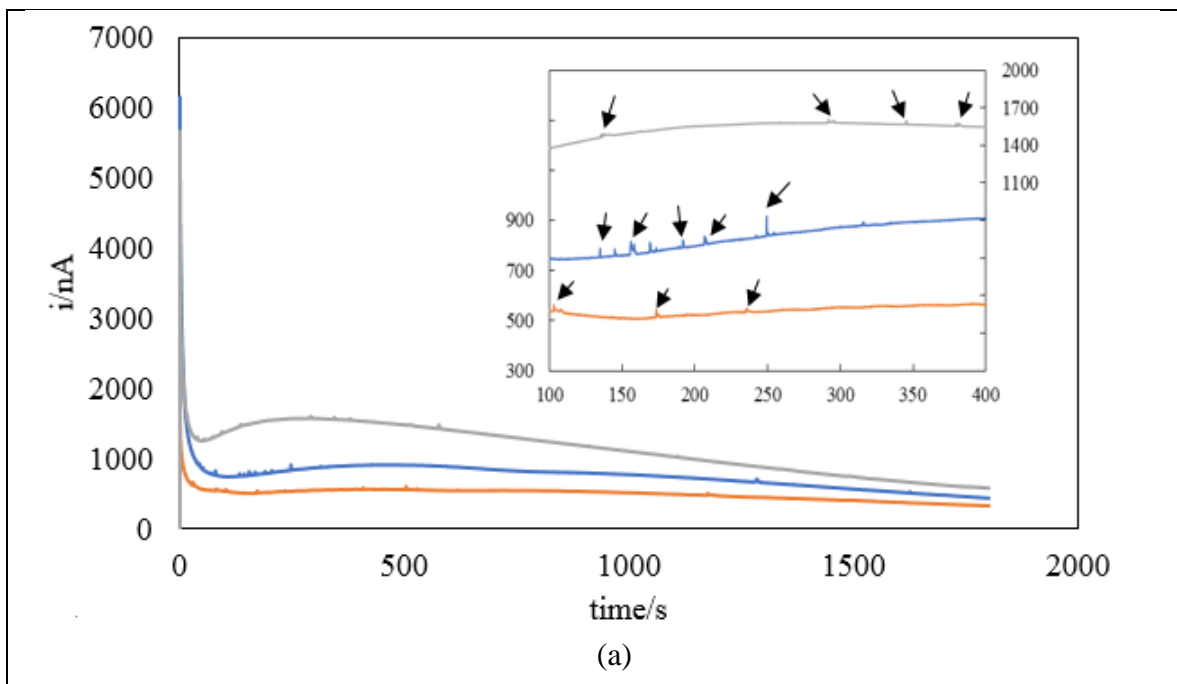


Figure 5.27. Metastable pitting graphs for TRC alloys at 0.01M NaCl test solution for (a) 50 mV, (b) 75 mV and (c) 100 mV below the pitting potential. For better representation magnified data between 300 to 600 seconds were given.



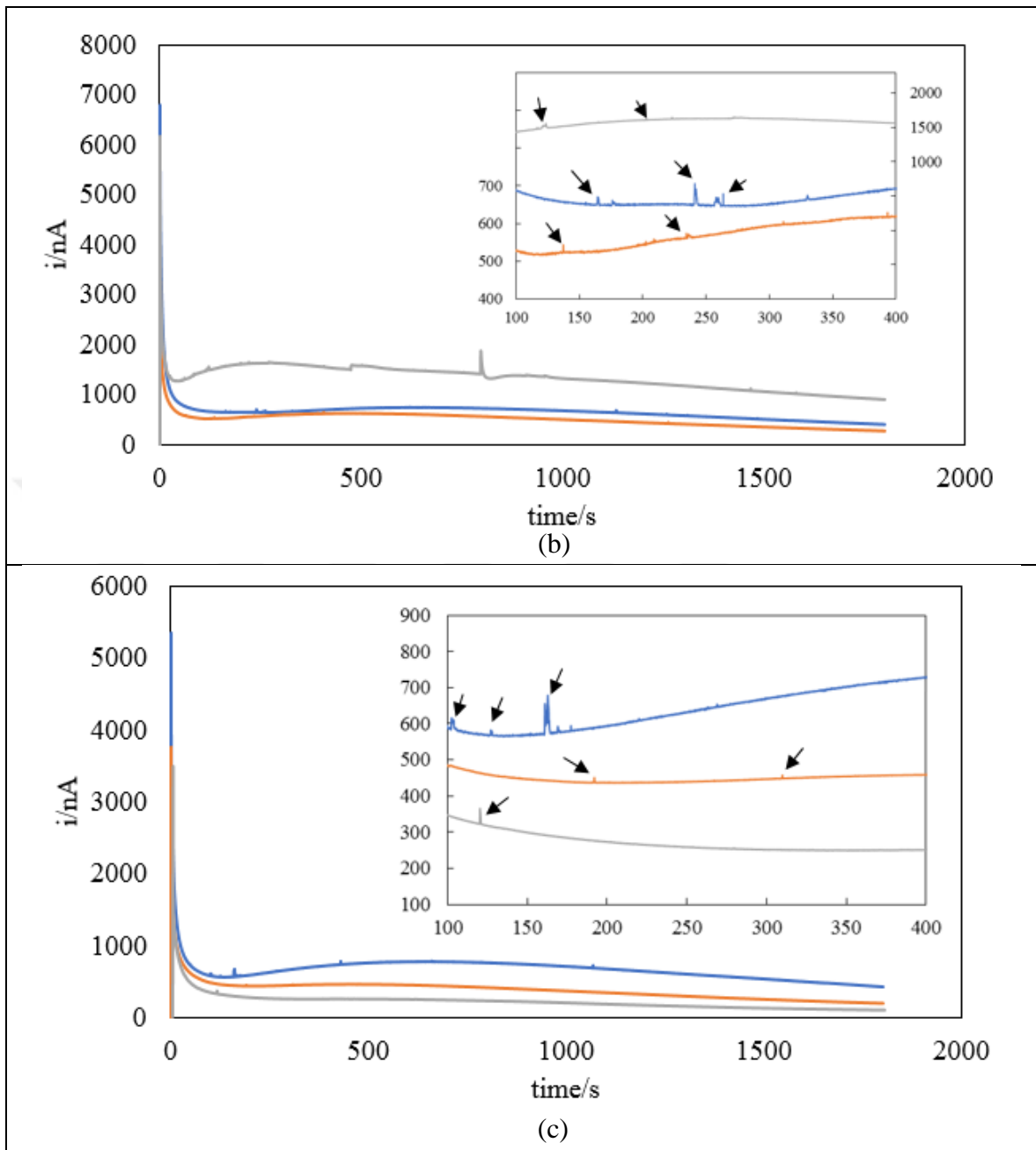
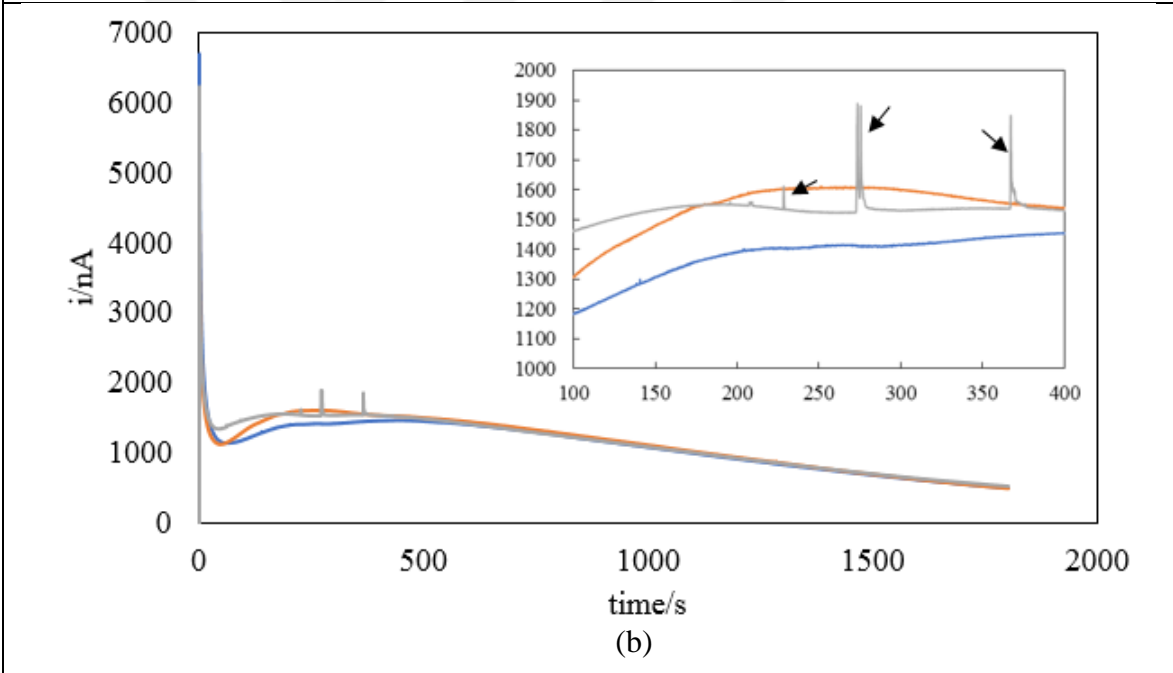
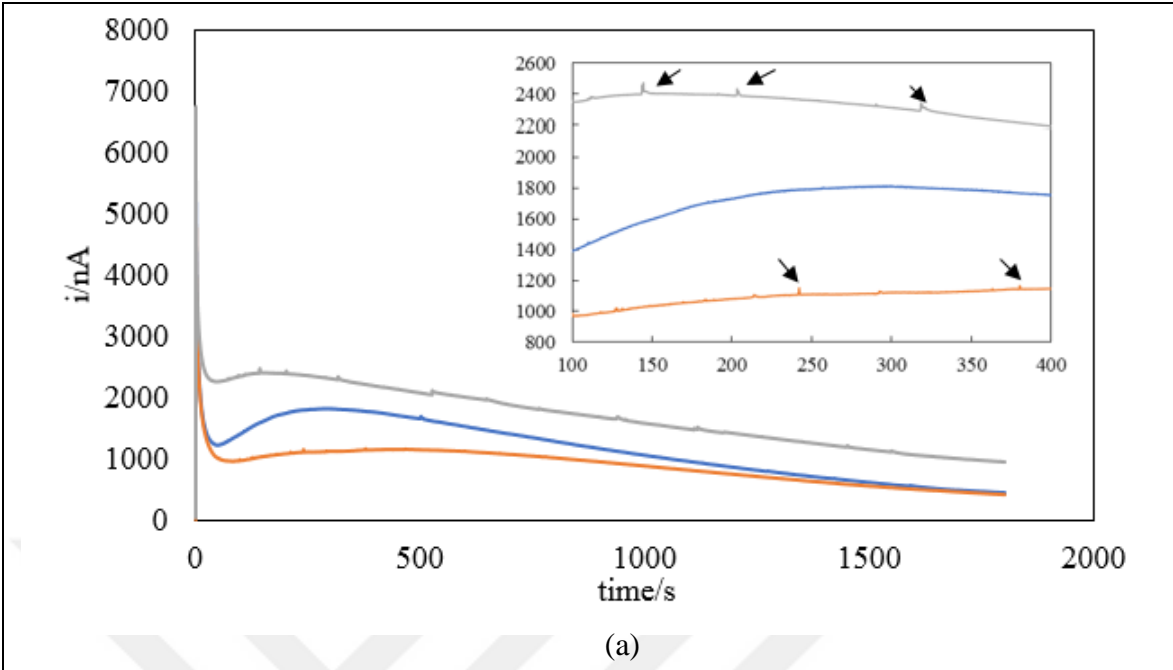


Figure 5.28. Metastable pitting graphs for DCC alloys at 0.001M NaCl test solution for (a) 50 mV, (b) 75 mV and (c) 100 mV below the pitting potential. For better representation magnified data between 100 to 400 seconds were given.



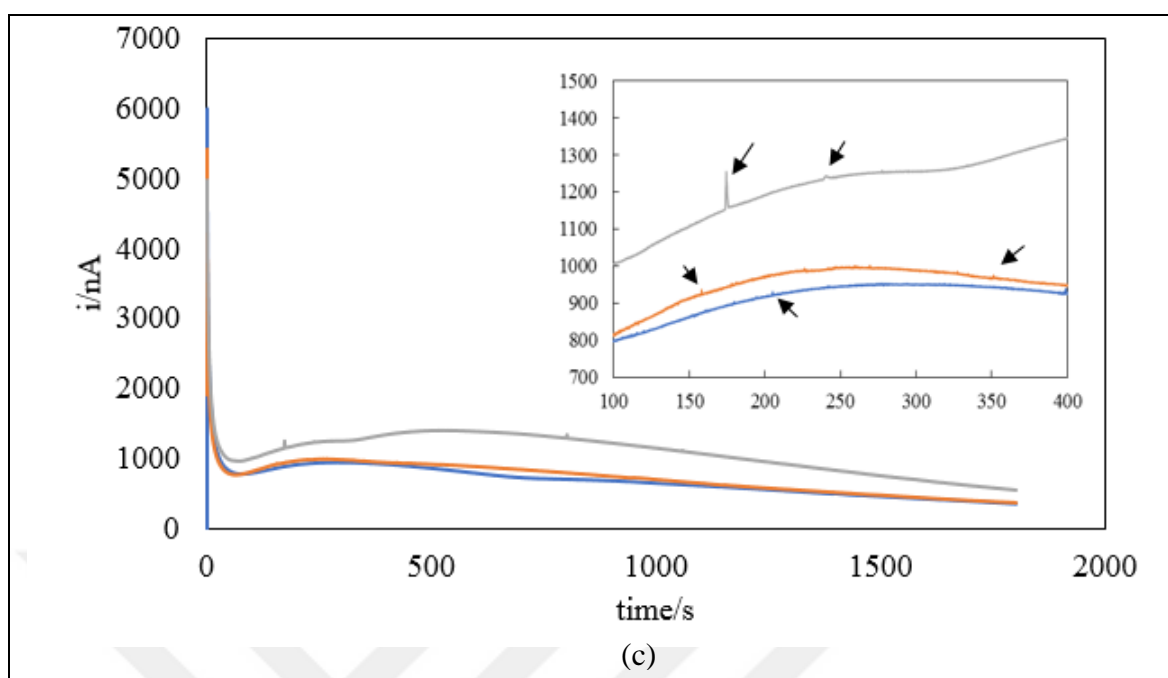


Figure 5. 29. Metastable pitting graphs for TRC alloys at 0.001M NaCl test solution for (a) 50 mV, (b) 75 mV and (c) 100 mV below the pitting potential. For better representation magnified data between 100 to 400 seconds were given.

In metastable pitting corrosion experiments, a criteria is needed for the determination of metastable pitting events seen in the current time series [67,68]. In this study, the current peaks are considered as metastable pitting events when the current rise from the background current is larger than 4 nA [67,68]. The rate of metastable pitting events (events/min/cm²) and average total charge (μC) of metastable pits were calculated for comparing the susceptibility of the two alloys to stable pitting corrosion. The metastable pits formed during the first 10 seconds of a measurement were not considered since the background current was changing very fast. The metastable pitting rate was calculated by dividing the total number of pits during a test by duration of the test (30 min) and the exposed surface area (0.03 cm²). The total charge was calculated as follows. The total charge passing in an experiment is recorded cumulatively by the potentiostat. The difference between the cumulative charge at the end of a metastable event minus the cumulative charge at the beginning of the event was taken as the charge of the metastable pitting event. The charges of all events were determined and summed to calculate the total charge of metastable pitting events in a potentiostatic experiment. Since the measurements were repeated multiple times under the same conditions, an arithmetic average was taken. Hence, the rates and charges reported in this

work are the average values. The average metastable pitting rate (events. $\text{cm}^{-2}.\text{min}^{-1}$) are given in Table 5.11. For an easier comparison of the two alloys, the data in Table 5.11 is plotted in Figure 5.30.

Table 5.11. Average metastable pitting rate results for DCC and TRC alloys

Applied Potential (below the E_{pit} , mV)	Metastable Pitting Rate ($\text{cm}^{-2}.\text{min}^{-1}$)			
	DCC 0.01 M NaCl	TRC 0.01 M NaCl	DCC 0.001 M NaCl	TRC 0.001 M NaCl
-50	40	13	19	22
-75	23	14	20	12
-100	21	9	8	13

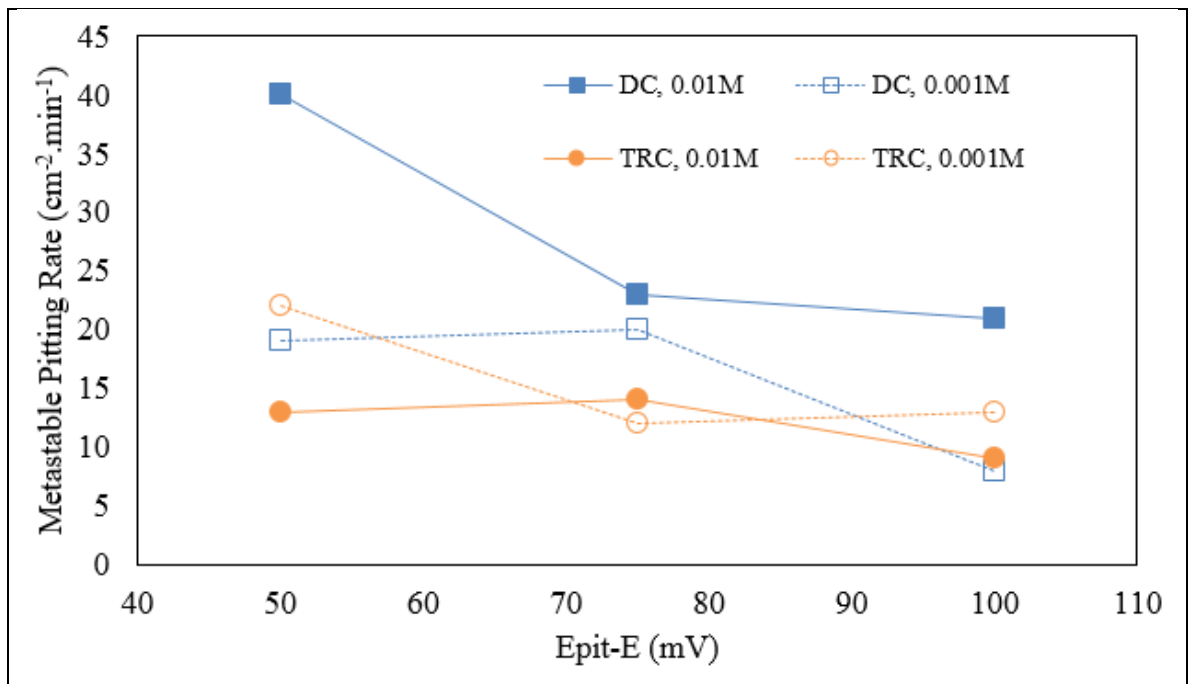


Figure 5.30. Metastable pitting rate for DCC and TRC alloys as a function of potential below E_{pit}

It is seen from the figure that the metastable pitting rate was generally larger as the applied potential approached the pitting potential for both alloys in both concentrations. For instance, for the TRC alloy in 0.001 M NaCl, the rate is 22 events.cm⁻².min⁻¹ at 50 mV below E_{pit} while it is 13 events.cm⁻².min⁻¹ at 100 mV below E_{pit}. At 0.01 M NaCl, the DCC alloy had a larger rate of metastable pitting events compared to the TRC alloy at all underpotentials. At 0.001 M NaCl, on the other hand, the rates were close to each other at 50 mV underpotential. The DCC alloy had a higher rate of metastable pitting at 75 mV underpotential, while the TRC alloy had a slightly higher rate at 100 mV underpotential. Thus, at 0.01 M NaCl, the DCC alloy may be more susceptible to stable pit formation. Gupta reported metastable pitting rates for pure aluminum at 50 mV, 75 mV and 100 mV below the pitting potential in 10 μM NaCl. The rates reported at these underpotentials were less than 50 events.cm⁻².min⁻¹ and comparable to the rates found in this study. However, the applied potential was much higher in their study, which explains comparable rates despite their use of pure aluminum in a much dilute solution.

The average total charges of metastable pitting events (μC) are given in Table 5.12. The average total charge graphs were also plotted for both 0.01 M and 0.001 M solutions and are represented in Figure 5.29.

Table 5.12. Average total charge results for DCC and TRC alloys

Applied Potential (below the E _{pit} , mV)	Total Charge (μC)			
	DCC 0.01 M NaCl	TRC 0.01 M NaCl	DCC 0.001 M NaCl	TRC 0.001 M NaCl
-50	65	18	44	76
-75	16	10	43	26
-100	59	8	6	18
Average	47	12	31	40

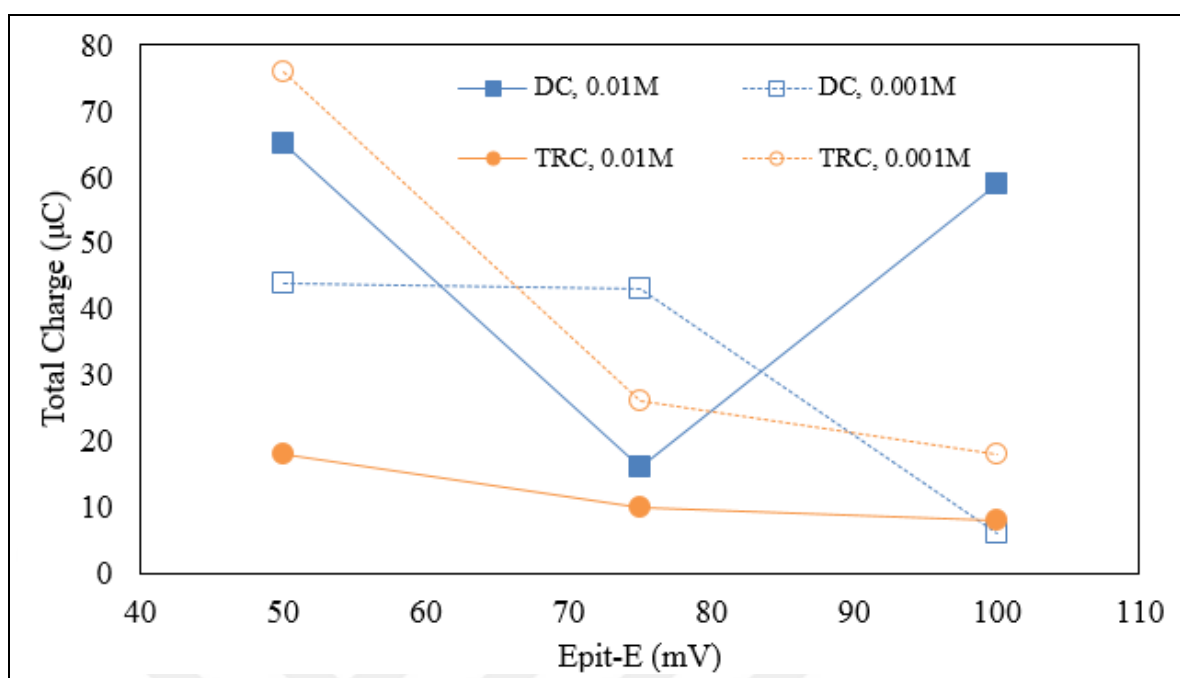


Figure 5.31. Average total charge for DCC and TRC alloys as a function of potential below E_{pit}

The average total charges generally decreased when the applied potentials became distant from the pitting potentials. For example, the total charge for TRC alloy in 0.01 M NaCl solution was 18 μC at the underpotential of 50 mV and was 8 μC at the underpotential of 100 mV. At 0.01 M NaCl, the DCC alloy had a larger total charge when compared to the TRC alloy at all underpotentials. An increase in the total charge of the events is seen when the underpotential was decreased from 75 mV to 100 mV in 0.01 M NaCl for the DCC alloy. In 0.001 M NaCl solution, the alloy exhibiting the highest total charge depended on the underpotential. According to the results presented in Tables 5.11 and 5.12, the total charge increased mostly as the metastable pitting rate increased.

5.7. RESULTS OF ELECTROCHEMICAL NOISE MEASUREMENT

Electrochemical noise (ECN) analysis is used to measure the corrosion activity in alloys without disturbing the sample to be tested. There are studies in which ECN of aluminum alloys exposed to a chloride containing solution were measured and analyzed [72–75]. It has been reported that ECN analysis can be used to differentiate between different types of corrosion [76,77]. The ECN is typically measured as the electrochemical current noise and

the electrochemical potential noise of a galvanically coupled pair of the same alloy. Both were measured in this study. In the ZRA mode, the potentiostat applies current to either electrode to equate their potential. This current as a function of time is called the electrochemical current noise. Additionally, the potential (with respect to the reference electrode) evolution of the couple with time is called the electrochemical potential noise. When pits form in the electrodes of the couple, changes in the voltage of the galvanic couple and in the current occurs. Thus, ECN can be used to study the localized corrosion activity of alloys. There are various methods (Power Spectral Density, Wavelet, Pitting Index, etc.) used to analyze the current and voltage ECN. Fast Fourier Transform (FFT) and Maximum Entropy Method (MEM) are the two sub method of power spectral density (PSD) [78]. In this study, PSD calculations were done to compare the results of the ECN experiments. The ECN data were collected after two different waiting periods while the galvanic couple is immersed in the solution. First set of experiments consisted of waiting 24 hours at open circuit potential and, then, ECN data collection for 30 minutes. The second set of experiments consisted of waiting 10 minutes at open circuit potential and then 3 hours of data collection. The experimental potential and current ECN data are plotted in Figures 5.32 through 5.35.

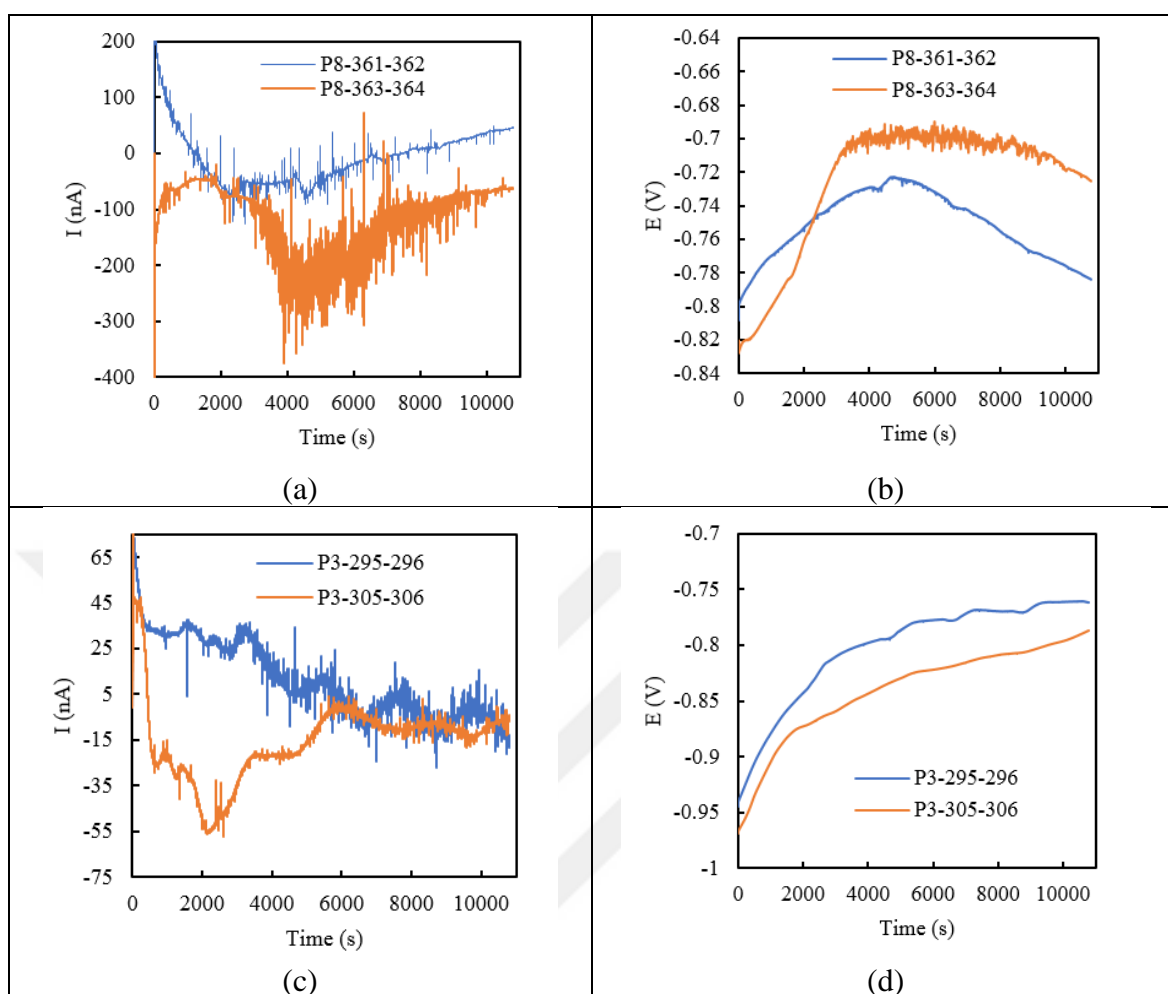


Figure 5.32. Current and potential results of 3 h ZRA measurement 10 minutes after immersion at 0.1 M NaCl solution (a), (b) DCC and (c), (d) TRC respectively

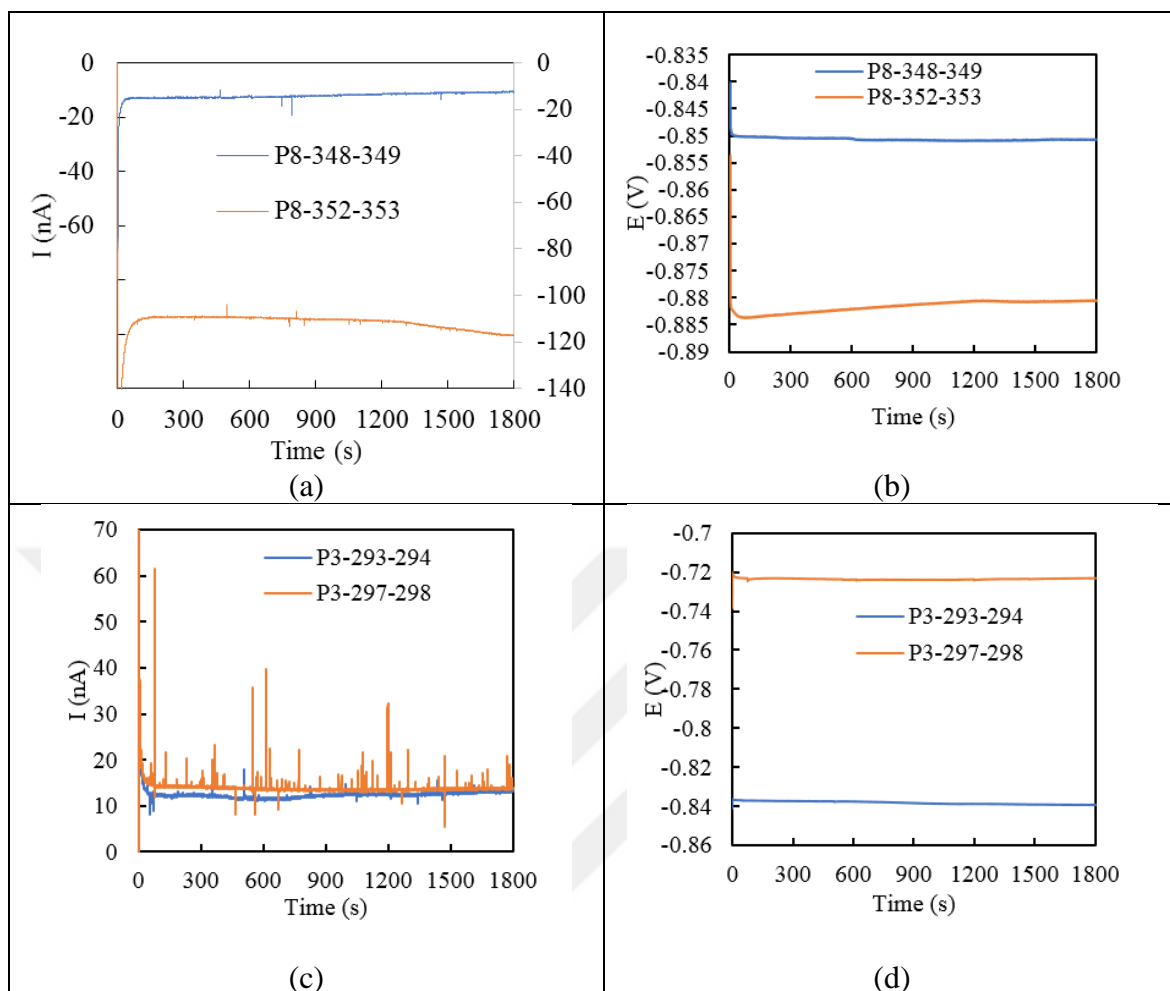


Figure 5.33. Current and potential results of 24 h OCP + 30 min. ZRA measurement at 0.1 M for (a), (b) DCC and (c), (d) TRC respectively

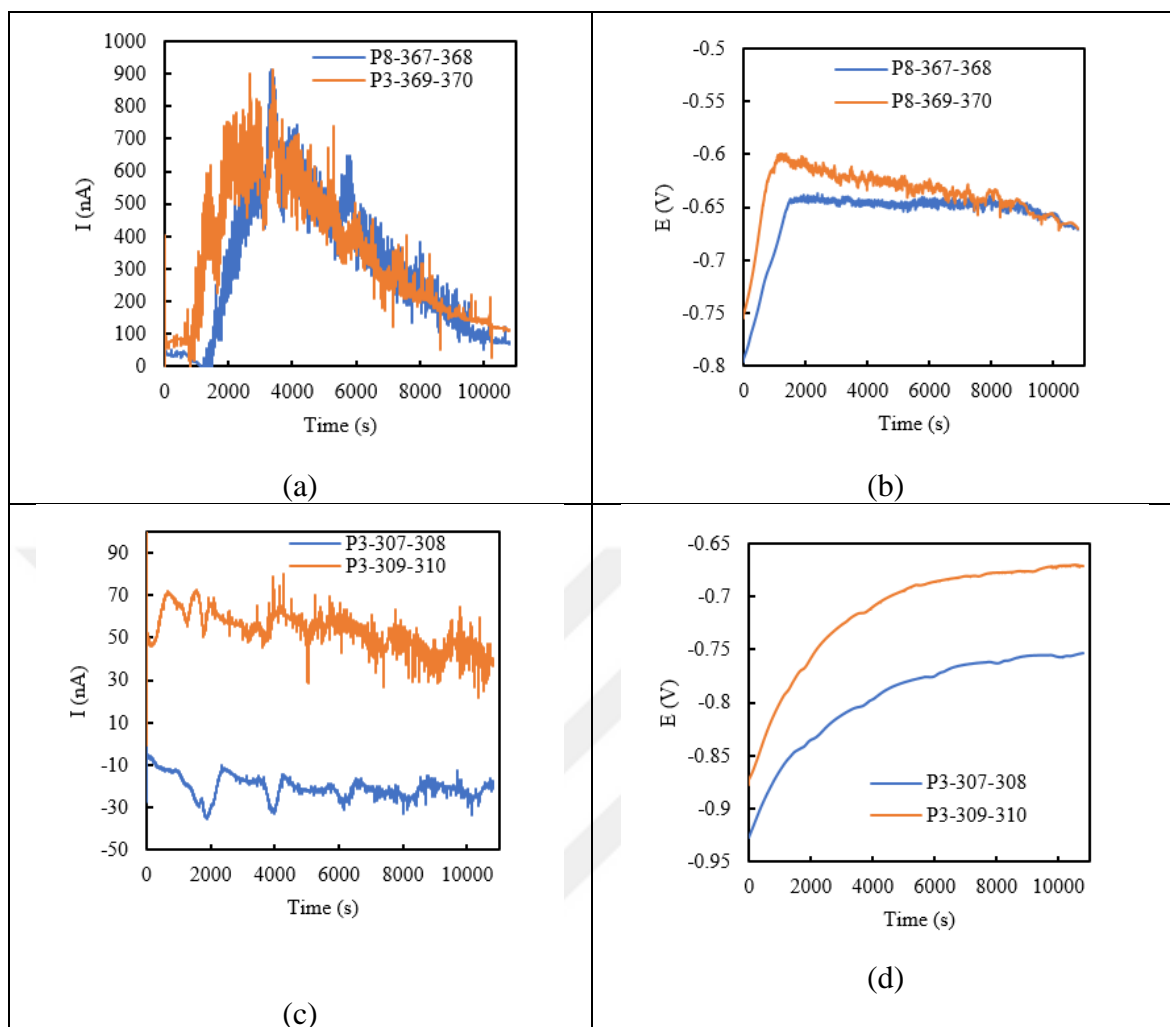


Figure 5.34. Current and potential results of 3 h. ZRA measurement 10 minutes after immersion at 0.01 M NaCl solution (a), (b) DCC and (c), (d) TRC respectively

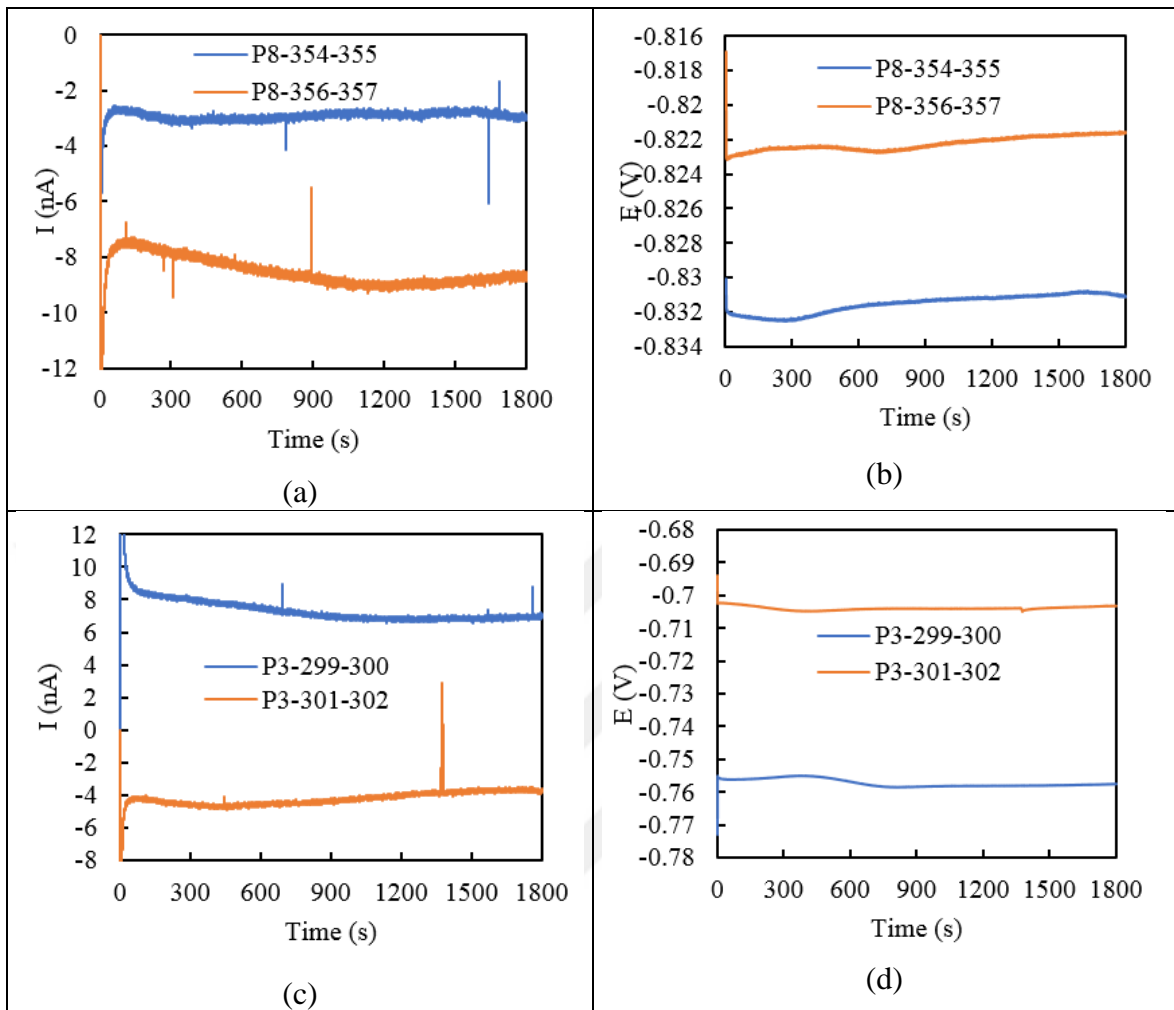


Figure 5.35. Current and potential results of 24 h. OCP + 30 min. ZRA measurement at 0.01 M for (a), (b) DCC and (c), (d) TRC respectively

Figure 5.32 compares the current and potential noise data recorded 10 minutes after immersion for the AA1050 DCC and AA1050 TRC alloys in 0.1 M NaCl solution. Figures 5.32 (a) and (b) show the results for the AA1050 DCC alloy, and (c) and (d) the results for the AA1050 TRC alloy. The orange and blue lines in each picture show the results of two experiments carried out under the same conditions. For the AA1050 DCC alloy, the current decreases in the first 1200 s (the current of the pair shown in orange exhibits negative current that decreases in absolute value). The galvanic current may be positive or negative depending on whether the corrosion is more intense in one electrode of the pair or in the other (working electrode 1 or working electrode 2). The current indicated by the blue line increased negatively after 1200 s and then decreased after 2400 seconds. After 7600 seconds, it showed a slow increase in the positive direction. The current indicated by orange increased

negatively after about 2000 s and started to decrease after about 4500 s. After 3 hours, both currents reached an absolute value of 40 - 60 nA. Fluctuations are observed in both current time series during the experiment. These fluctuations are localized corrosion events (Homborg et al., 2014b). The galvanic current in orange showed higher localized corrosion activity. For example, oscillations with large amplitudes were seen around 4000 s. Figure 5.32 (b) shows the potential noise of the same experiments. It is seen that the potentials increased from about - 0.81 V for the first 3000-4700 seconds. For the pair that exhibited high corrosion activity (orange) between 3000 and 9000 s, significant fluctuations of potential were observed, and the average potential was around -0.70 V. Its potential decreased after 9000 s. The other pair's potential (blue) decreased after 5000 s. Figure 5.32 (c) shows the current noise recorded in two experiments with the AA1050 TRC alloy. Again, in one experiment (current shown in blue) oscillations of higher amplitude (higher local corrosion activity) were seen compared to the other experiment. In the alloy produced by this production method, the currents are within ± 15 nA after about 6000 s. The potentials increased from -0.95 V to about -0.80 (Figure 5.32 (d)). Another difference between the alloys of the two production techniques is the change in corrosion activity with time. Although higher corrosion activity was seen for the DCC alloy (Figure 5.32 (a) and (c)), this activity decreased over time. For example, in the range of 4000-5000 s, high activity was observed in the current, while at 10000 s, much lower activity was observed. On the other hand, the activity of the TRC alloy was maintained for 3 hours, although lower level of local corrosion activity was observed compared to the DCC alloy.

Figure 5.33 shows the current and potential measurements of the galvanic couples after immersion in open circuit conditions for 24 hours. For both production methods it is seen that the currents remain approximately constant after the first 150 s (Fig. 5.33 (a) and (c)). In a sample couple (blue) of the AA1050 DCC alloy and in both couples of the TRC alloy, the current was between 10 and 20 nA. However, the other couple of the AA1050 DCC (orange) exhibited a current of - 110 nA. Comparing Figure 5.33 (a) with (c) shows that the current is more noisy in the TRC alloy. For example, looking at the current shown in orange in Figure 5.33 (c), there are many current peaks on the background current. These are metastable pitting events and some have peak currents above 10 nA. The potentials of the alloys of both production methods have remained approximately constant (Figure 5.33 (b) and (d)). However, the DCC alloy had more negative potentials.

The results at 0.01 M concentration are given in Figures 5.34 and 5.35. ZRA measurements initiated 10 minutes after immersion are given in Figure 5.34. In these conditions, higher currents and noise levels were seen in the AA1050 DCC alloy than the AA1050 TRC alloy (Figure 5.34 (a) and (c)). In the DCC alloy, currents increased for approximately the first 3000 s, but then decreased and dropped to 70-100 nA around 10000 s (Figure 5.34 (a)). Between 2000-6000 s, very high amplitude current oscillations, that is, intense localized corrosion activity was observed. Similar to the behavior at 0.1 M, the noise level after about 6000 s, i.e. the amplitude of the current fluctuations, decreased. In couples of the AA1050 TRC alloy, the currents were approximately 25 and 50 nA (Figure 5.34 (c)). After the first 3000 s, the corrosion activity continued. The potentials of the DCC alloy couples showed a rapid increase and reached approximately -0.62 V during the first 1500 s (Figure 5.34 (b)). Potential oscillations were observed. The same amplitude fluctuations were not observed in the potentials of the TRC alloy (Figure 5.34 (d)). ZRA measurements of samples waited in open circuit conditions at 0.01 M concentration are shown in Figure 5.35. Alloys of both production methods showed a current of less than 10 nA after 150 s. Metastable pitting events (sudden peaks and bottoms of current) were seen (Figure 5.35 (a) and (c)). From Figures 5.35 (b) and (d), the potentials of TRC couples were about 100 mV more positive. In sum, the measurements started 10 minutes after immersion showed higher local corrosion activity in DCC samples at both concentrations. However, this activity decreases after approximately 6000 s. At the end of 24 hours, more metastable pitting events were observed in the galvanic currents of the TRC alloy at 0.1 M concentration. After 24 hours, the DCC alloy's galvanic couple potentials were more negative.

The ECG-Comon PSD calculation program was used for power spectrum density (PSD) analysis of the electrochemical noise data [79]. In this method, time domain is translated to the frequency domain and current PSD data was calculated with a similar method in the Lunt et al. study [66]. The calculated PSD data were plotted in a logarithmic graph and the results are shown in Figure 5.36 for 0.1 M NaCl and in Figure 5.37 for 0.01 M NaCl. Since the current noise was more pronounced compared to the potential noise, only the electrochemical current noise was analyzed. To compare the DCC alloy with the TRC alloy, the time intervals during which high current noise were observed were chosen for the analysis. For both concentrations, the high noise activity was seen between 5000-6000

seconds for the DCC alloy and between 9800-10800 seconds for the TRC alloy in the current versus time plots.

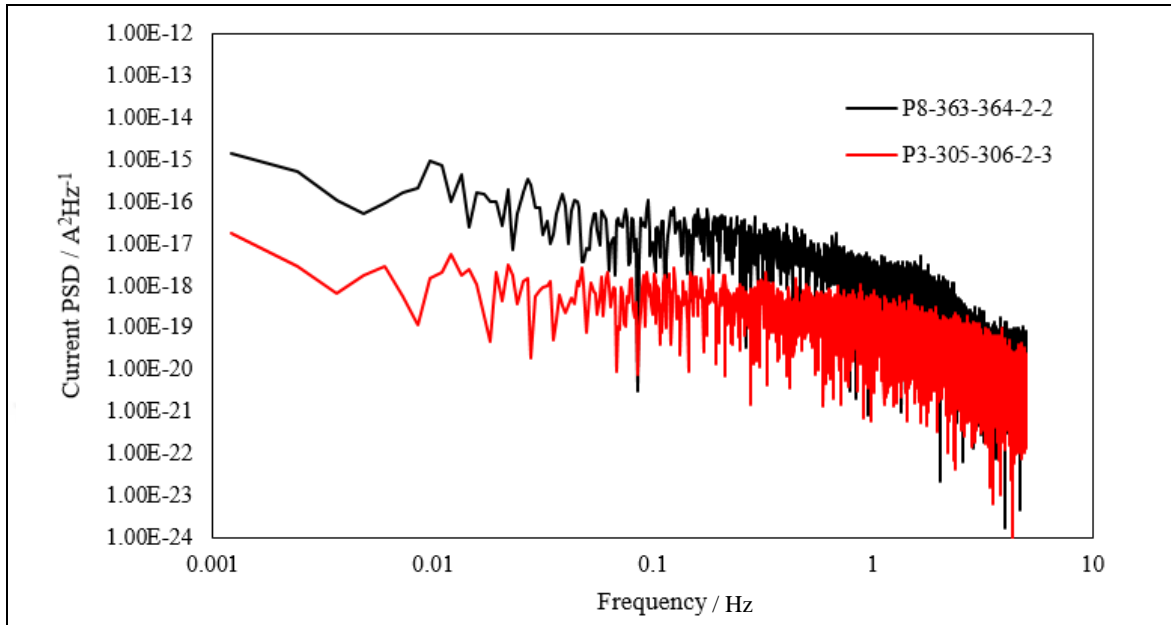


Figure 5.36. Current PSD results at 5000-6000 sec for DCC alloy and 9800-10800 sec for TRC alloy at 0.1 M for 3 sec. OCP + 3 h. ZRA measurement

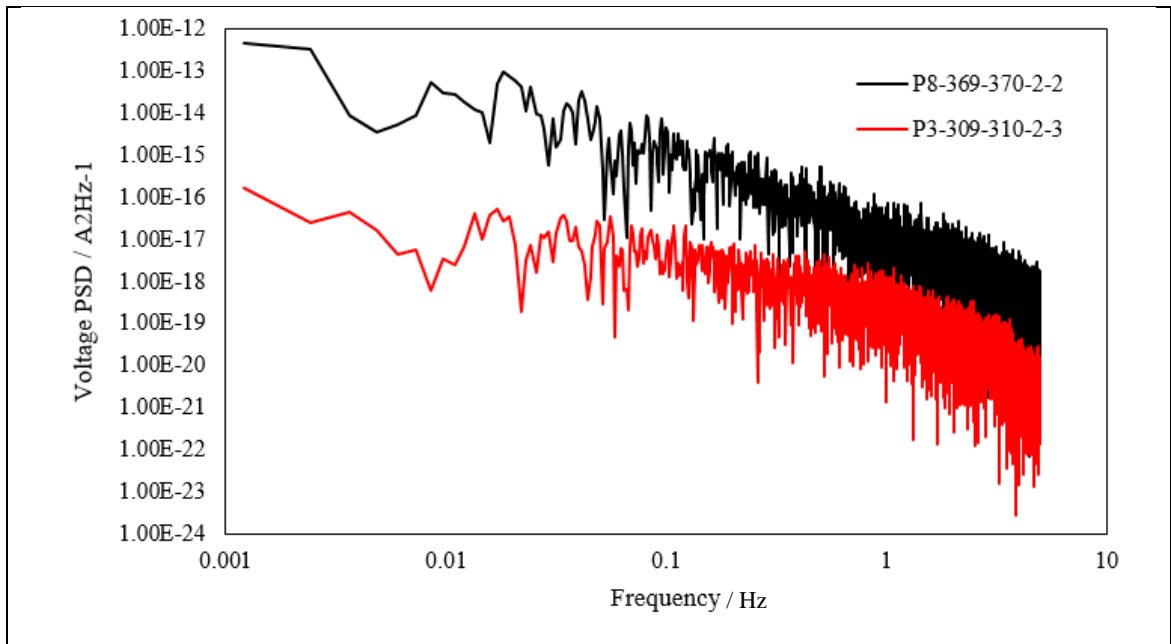


Figure 5.37. Current PSD results at 5000-6000 sec for DCC alloy and 9800-10800 sec for TRC alloy at 0.01 M for 3 sec. OCP + 3 h. ZRA measurement

Figure 5.36 shows the PSDs for the two alloys in 0.1 M NaCl. The black and red lines represent the DCC and TRC alloys, respectively. The overall level of the power density graph is indicative of corrosion activity [77,80]. In this respect, Figure 5.36 and 5.37 show that the DCC alloy exhibited higher corrosion activity because the power density graphs of the alloys of this production technique are above the graphs of the alloys of the twin roll technique. Oxygen reduction reaction is known to occur Fe-containing intermetallics [50]. The aluminum matrix around it dissolves by oxidation reaction. Thus, a galvanic corrosion event starts. Another important issue is the importance of the cathode area. A larger cathode area will result in more galvanic corrosion. Thus, the galvanic corrosion of a larger intermetallic particle will be higher than the smaller one. This probably the reason for the higher levels of noise (local corrosion activity) seen in the DCC alloy since it contains larger intermetallics.

PSD graphs may consist of two parts, a horizontal part in low frequencies and a high frequency part with a roll of slope [81] [82]. Some studies claim that the roll off slopes can be used to differentiate between the general or localized corrosion [77] [81]. Table 5.13 presents the roll off slopes that were calculated from Figures 5.37 and 5.38 for frequencies below 0.1 Hz. Higher roll-off slopes are found for the DCC alloy in both solutions, which showed higher localized corrosion activity.

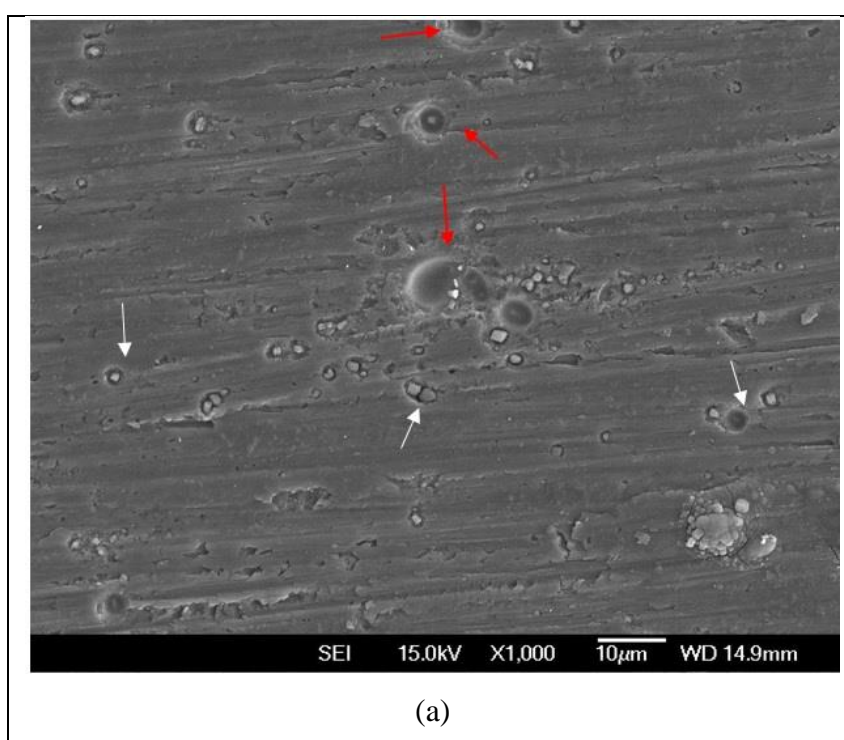
Table 5.13. The slope of the current PSD graphs at 0.1 M and 0.01 M test solution

		10 minutes after immersion ZRA Measurement	
		DCC (between 5000-6000 sec)	TRC (between 9800-10800 sec)
Type of alloys	Concentration		
	0.1 M	-2.30	-1.40
	0.01 M	-2.16	-1.91

5.8. RESULTS OF IMMERSION TESTS

In the immersion tests, AA1050 alloys produced by different production techniques were immersed in 0.01 M NaCl solution for 1 week. After the surfaces were cleaned from corrosion products, scanning electron microscopy (SEM) and optical profilometer analyses

were done. Figure 5.38 shows SEM images of the AA1050 DCC and the AA1050 TRC alloys at 1000 magnification. In the SEM-EDS investigations on the non-corroded surfaces, it was found that the intermetallics in the AA1050 alloys contain Al, Fe and Si. Since such intermetallics are more noble than the aluminum matrix, it has been reported that the aluminum matrix around them dissolves and initiate the pitting corrosion [50,83]. Aballe et al. reported that semicircular pits formed around the intermetallics in the immersion tests in AA5083 alloy. They reported that the formation of semicircular pits because the pH increase resulting from the oxygen reduction reaction on the intermetallics caused the dissolution (oxidation) of the aluminum matrix around the intermetallics. The pits surrounding the intermetallics have been reported after immersion tests in different aluminum alloys [84–86]. Figure 5.38 shows the pits surrounding the intermetallics in AA1050 alloys produced by both DCC (a) and TRC (b) method. The white arrows in these figures show examples of pits formed around the intermetallic. The red arrows show the large pits. Since the intermetallics in the TRC alloys are smaller, it is seen that the pits formed in this alloy are usually smaller than those in the DCC alloy. As shown in Figure 5.38 (b), the diameter of the pits of TRC alloys is generally less than 1.5 microns. Large pits were observed in the AA1050 DCC sample. For example, the pit (indicated by the red arrow) in the middle of Figure 5.38 (a) has a diameter of about 6 μm .



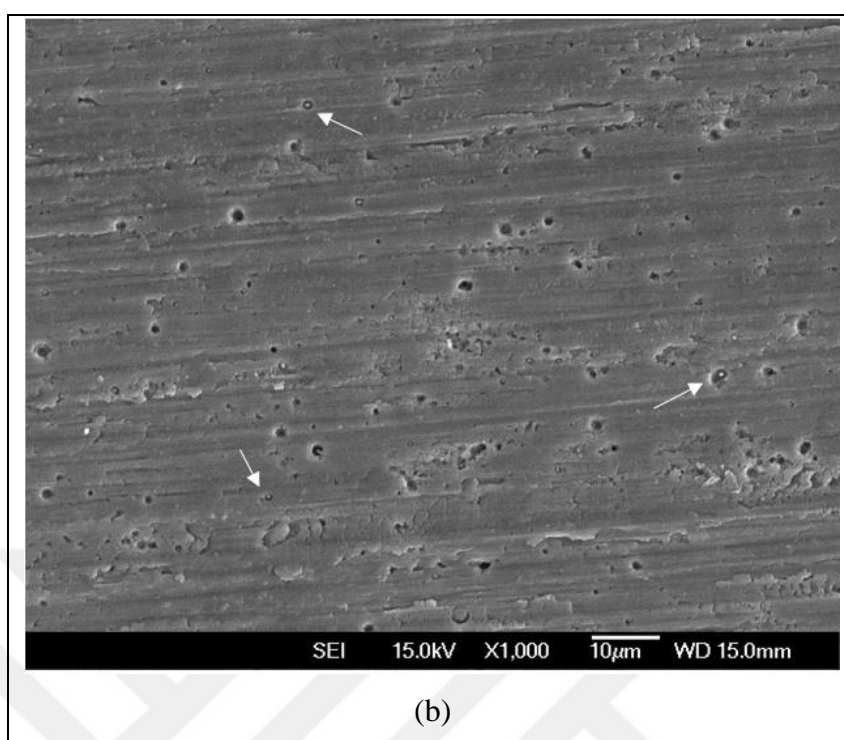


Figure 5.38. SEM images of the surfaces of AA1050 (a) DCC and (b) TRC alloys which have been immersed for 7 days in 0.01 M NaCl solution.

Optical profilometry is a technique that is used to examine the pits formed on the alloy surfaces after the immersion tests [68,87,88]. Optical profilometry analysis of the AA1050 DCC and AA1050 TRC alloys are given in Figure 5.39. Figure 5.39 (a) shows the profile of the DCC alloy and Figure 5.39 (b) shows the profile of the TRC alloy. The scale next to each picture shows the relative depth. Red represents elevation and blue represents pit. From Figure 5.39 (a), blue and approximately round spots (pits) are seen. When Figure 5.39 (a) and (b) are compared, the AA1050 DCC alloy has larger pits.

As a result, both optical profilometry and SEM investigations showed that pits of larger diameter formed in the AA1050 DCC alloy compared to the AA1050 TRC alloy.

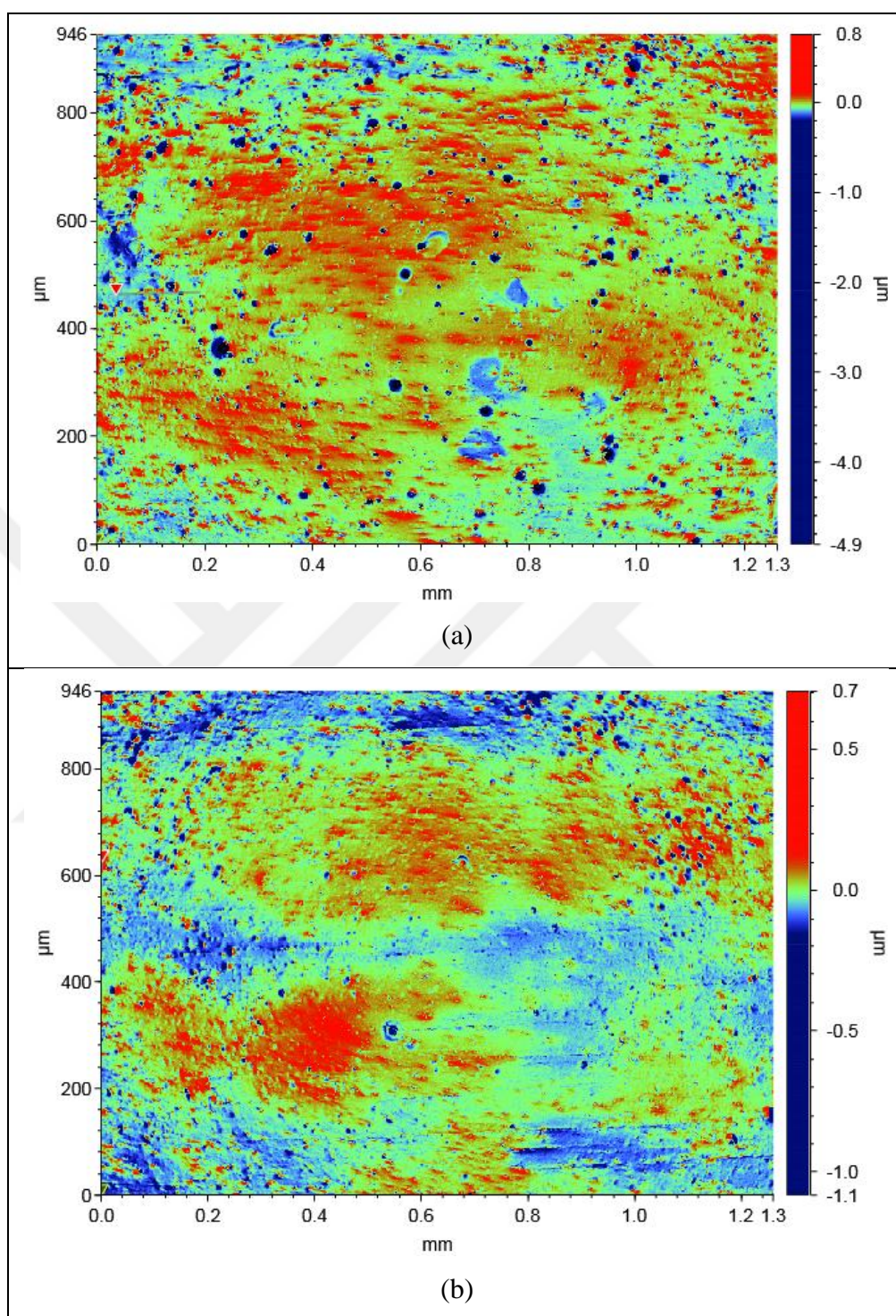


Figure 5.39. Optic profilometer images of the surfaces of AA1050 (a) DCC and (b) TRC alloys which have been immersed for 7 days in 0.01 M NaCl solution

6. CONCLUSION

The resistance of pit corrosion of AA1050 alloy sheets that are produced by the DC casting and twin roll casting techniques was compared and the following results were obtained in this study.

1. Microstructure analysis (Optical microscope and SEM EDS) results showed that larger intermetallics were present in the DCC alloy compared to the TRC alloy. It was also found that the number of intermetallics in the 1050 TRC alloy was larger. The particles contained Al, Fe and Si in both alloys.
2. In open circuit potential measurements (OCP), the OCPs of both alloys showed a rapid change in anodic direction for all three concentration (1M, 0.1M and 0.01M NaCl). In the first 5000 seconds, the potential of the DCC alloy is more anodic than the potential of the TRC alloy for all three concentration.
3. The results of the cyclic potential polarization (CPP) experiments reveal that the average pitting potentials of the AA1050 alloys produced by two production techniques are quite close to each other. In general, the alloys produced by the DCC casting technique have more positive pitting potentials than the alloys produced by the TRC technique. The highest difference was observed in 1 M solution (27 mV) and the lowest difference was observed in 0.001 M solution (6 mV).
4. Repassivation potentials (E_{repass}) were determined with potentiostatic measurements. In this technique, the repassivation potentials were found as potential ranges (25 mV) and the midpoint of a range was accepted as E_{repass} . The largest difference between the DCC alloy and the TRC alloy was at 1 M solution. The DCC alloy has 50 mV more positive E_{repass} than the TRC alloy at 1 M NaCl. The DCC alloys also has a more positive E_{repass} potential at 0.1 M NaCl. However, there is no difference in 0.01 M solution.

5. In galvanostaircase cyclic polarization method, both the breakdown potential and the protection potential were calculated. Breakdown potential and protection potentials were more positive for the DCC alloy in all three concentrations (1 M, 0.1 M and 0.01 M). The highest breakdown potential difference between the DCC alloy and the TRC alloy is found at 0.01 M solution as 17 mV. The highest protection potential difference between the alloys was found 5 mV at 1 M solution.
6. Metastable pitting studies were done in 0.01 M and 0.001 M NaCl with three different applied potentials (50 mV, 75 mV and 100 mV below pitting potential). The rates in the DCC alloy are generally higher than the TRC alloy for both concentrations. The greatest difference metastable pitting rate between the DCC and the TRC alloys is 16 events/cm²/min at 0.01 M solution for the underpotential of 50 mV. On the other hand, the lowest potential difference found as 2 event/cm²/min at 0.001 M solution for 100 mV below the pitting potential. At 0.01 M NaCl, the DCC alloy had a larger total charge when compared to the TRC alloy at all underpotentials. In 0.001 M NaCl solution, the alloy exhibiting the highest total charge depended on the underpotential.
7. The current and potential noises of the galvanic couples were measured in 0.1 M and 0.01 M NaCl solutions containing oxygen. The measurements started 10 minutes after immersion with AA1050 alloys showed higher local corrosion activity in the DCC alloy at both concentrations. The higher corrosion activity in the DCC alloy is likely due to the presence of larger intermetallics. Due to the larger intermetallics, higher galvanic effect and more intense corrosion activity between the intermetallics and the aluminum matrix is expected. However, this activity decreases after approximately 6000 s. Higher roll-off slopes were seen on the power density graphs of the current for the DCC alloy. At the end of 24 hours, more metastable pitting events were observed in the galvanic currents of the TRC alloy at 0.1 M concentration. After 24 hours, the DCC alloy's galvanic couple potentials were more negative.
8. According to the results of surface imaging analysis (optical profilometry and SEM), after the immersion tests for 7 days in 0.01 M NaCl, the pits formed in the DCC alloy are larger compared to those formed in the TRC alloy.

9. Based on the pitting potentials from the cyclic potential polarization measurements, the repassivation potentials determined from the potentiostatic measurements and the breakdown and the protection potentials found from the galvanostaircase cyclic polarization measurements, the DCC alloy and the TRC alloy exhibited similar resistances to the pitting corrosion.



REFERENCES

1. Ünal A. 1050 A, 3003, 3105, 5005 Alüminyum alaşımlarının çift merdaneli döküm yöntemiyle levha şeklinde imalatı ve mikroyapılarının incelenmesi [dissertation]. İstanbul, Istanbul Technical University; 2005.
2. Jones DA. *Principles and prevention of corrosion*. New Jersey: Pearson Education; 1996.
3. Elektrot potansiyelleri | Sanatsal eğitim. [cited 2018 19 November]. Available from: <http://www.sanatsalbilgi.com/DOKUMANLAR/24/elektrot-potansiyelleri-693.html>
4. Skoog DA, Holler FJ. *Principles of instrumental analysis*. California: Brooks/Cole; 2007.
5. What is a Reference Electrode?. [cited 2018 28 October]. Available from: <https://www.corrosionpedia.com/definition/970/reference-electrode>
6. Aluminum E-pH (Pourbaix) diagram. [cited 2019 24 June]. Available from: <https://corrosion-doctors.org/Corrosion-Thermodynamics/Potential-pH-diagram-aluminum.htm>
7. What is Localized Corrosion? - Definition from Corrosionpedia. [cited 2018 23 December]. Available from: <https://www.corrosionpedia.com/definition/741/localized-corrosion>
8. Types of Corrosion-General & Localized Corrosion-Capital Painting. [cited 2018 23 December]. Available from: <http://www.capital-painting.com/types-of-corrosion/>
9. Çukurcuk Korozyonu (Pitting Corrosion). [cited 2018 15 November]. Available from: <http://www.stmcoatech.com/cukurcuk-korozyonu-pitting-corrosion->
10. Understanding The Alloys Of Aluminum. [cited 2018 10 October]. Available from: <http://www.alcotec.com/us/en/education/knowledge/techknowledge/understanding-the-alloys-of-aluminum.cfm>

11. Aluminum Association I. *Rolling Aluminum : from the mine through the mill*. Virginia. The Aluminum Association, Inc.; 2008.
12. Kammer C. *Continuous casting of Aluminium*. Goslar: European Aluminium Association; 1999.
13. Büyükbaş F. Çift merdaneli sürekli levha döküm yöntemi ile üretilmiş AA3003 alaşımlı alüminyum levhalarda proses parametrelerinin özelliklere etkisi [dissertation]. İstanbul, Istanbul Technical University; 2001.
14. Sanders RE. Continuous casting for aluminum sheet: A product perspective. *The Journal of The Minerals, Metals & Materials Society*. 2012;64(2):291–301.
15. Barekar NS, Dhindaw BK. Twin-roll casting of aluminum alloys - An overview. *Materials and Manufacturing Processes*. 2014;29(6):651–61.
16. Slamova M, Karlik M, Robaut F, Slama P, Veron M. Differences in microstructure and texture of Al-Mg sheets produced by twin-roll continuous casting and by direct-chill casting. *Materials Characterization*. 2002;49(3):231–40.
17. Zhao YM, Morris JG. Comparison of the texture evolution of direct chill and continuous cast AA5052 hot bands during isothermal annealing. *Metallurgical and Materials Transactions A*. 2005;36A:2505–15.
18. Yu XF, Zhao YM, Wen XY, Zhai T. A study of mechanical isotropy of continuous cast and direct chill cast AA5182 Al alloys. *Materials Science and Engineering A*. 2005;394(1–2):376–84.
19. Kim K. The effect of melt conditioning on segregation of solute elements and nucleation of aluminum grains in a twin roll cast aluminum alloy. *Metallurgical and Materials Transactions A: Physical Metallurgy and Materials Science*. 2014;45(10):4538–48.
20. Lockyer SA, Yun M, Hunt JD, Edmonds D V. Micro- and macrodefects in thin sheet twin-roll cast aluminum alloys. *Materials Characterization*. 1996;37(5):301–10.
21. Yun M, Lokyer S, Hunt J. Twin roll casting of aluminium alloys. *Materials Science and Engineering: A*. 2000;280:116–23.

22. Gras C, Meredith M, Hunt JD. Microstructure and texture evolution after twin roll casting and subsequent cold rolling of Al-Mg-Mn aluminium alloys. *Journal of Materials Processing Technology*. 2005;169(2):156–63.
23. Keles O, Dundar M. Aluminum foil: Its typical quality problems and their causes. *Journal of Materials Processing Technology*. 2007;186(1–3):125–37.
24. Zhou SX, Zhong J, Mao D, Funke P. Experimental study on material properties of hot rolled and continuously cast aluminum strips in cold rolling. *Journal of Materials Processing Technology*. 2003;134(3):363–73.
25. Trueba M, Trasatti SP. Study of Al alloy corrosion in neutral NaCl by the pitting scan technique. *Materials Chemistry and Physics*. 2010;121(3):523–33.
26. Speckert L, Burstein GT. Combined anodic/cathodic transient currents within nucleating pits on Al-Fe alloy surfaces. *Corrosion Science*. 2011;53(2):534–9.
27. Krakowiak S, Darowicki K. Electrochemical and acoustic emission studies of aluminum pitting corrosion. *Journal of Solid State Electrochemistry*. 2009;13(11):1653–7.
28. Comotti IM, Trueba M, Trasatti SP. The pit transition potential in the repassivation of aluminium alloys. *Surface and Interface Analysis*. 2013;45(10):1575–84.
29. Abdulstaar M, Mhaede M, Wagner L, Wollmann M. Corrosion behaviour of Al 1050 severely deformed by rotary swaging. *Materials and Design*. 2014;57:325–9.
30. Gheem E V, Vereecken J, Pen LC. Influence of different anions on the behaviour of aluminium in aqueous solutions. *Journal of Applied Electrochemistry*. 2002;32:1193–200.
31. Kurt K, Dursun A, Dilsizoğlu B, Anger G, Ürgen M. Comparison of the corrosion behaviors of Twin-Roll cast and DC cast AA6016 and AA6082 for automotive applications. *TMS Annual Meeting*. 2007;(Cv):79–88.
32. Flat cells. [cited 2018 27 December]. Available from: [https://www.biologic.net/accessories/corrosion-cell-kit/flat-cells-1-10-cm²-sample-area/?filter\[division\]=ec-lab](https://www.biologic.net/accessories/corrosion-cell-kit/flat-cells-1-10-cm²-sample-area/?filter[division]=ec-lab), 2016

33. Counter electrodes - Bio-Logic Science Instruments. [cited 2018 27 December]. Available from: <https://www.bio-logic.net/accessories/electrodes/counter-electrodes/>
34. Reference electrodes & porous glass frits - Bio-Logic Science Instruments. [cited 2018 27 December]. Available from: <https://www.bio-logic.net/accessories/electrodes/reference-electrodes-porous-glass-frits/>
35. Metkon.com. [cited 2018 27 December]. Available from: http://www.metkon.com/pics/others/260_metkon_consumables_2018.pdf
36. 3M™ Electroplating Tape 470 | 3M United States. [cited 2018 27 December]. Available from: https://www.3m.com/3M/en_US/company-us/all-3m-products/~3M-Electroplating-Tape-470/?N=5002385+3293241703&rt=rud
37. SP-200 Potentiostat - Bio-Logic. [cited 2018 27 December]. Available from: <https://www.bio-logic.net/products/multichannel-conductivity/sp-200-potentiostat-galvanostat/>
38. Buehler Phoenix Alpha 49-5500-230 Grinder Polisher | Labequip. [cited 2018 27 December]. Available from: <http://www.labequip.com/buehler-phoenix-alpha-495500230-polisher.html>
39. NMM-800/820 Series Metallurgical Microscope. [cited 2018 27 December]. Available from: http://www.xmphio.com/html_products/NMM-800820-Series-Metallurgical-Microscope-57.html
40. Product specification NaCl. 2018 [cited 2018 29 December]. p. 2018. Available from: <https://www.sigmaaldrich.com/catalog/product/sigald/s9888?lang=en®ion=TR>
41. Product specification KCl. 1993 [cited 2018 29 December]. p. 21–2. Available from: <http://www.tandfonline.com/doi/abs/10.1080/09613219308727250>
42. Ethanol CAS 64-17-5 | 100983. [cited 2018 27 December]. Available from: http://www.merckmillipore.com/TR/tr/product/Ethanol,MDA_CHEM-100983
43. Nisancioglu K, Holtan H. The protection potential of aluminium. *Corrosion Science*. 1978;18(11):1011–23.
44. Hirozawa ST. Galvanostaircase polarization. *Journal of The Electrochemical Society*.

- 1983;130(8):1718.
45. Curioni M, Balaskas AC, Thompson GE. An alternative to the use of a zero resistance ammeter for electrochemical noise measurement: Theoretical analysis, experimental validation and evaluation of electrode asymmetry. *Corrosion Science*. 2013;77:281–91.
 46. Homborg AM, Tinga T, Zhang X, Van Westing EPM, Oonincx PJ, De Wit JHW, Mol JMC. Time-frequency methods for trend removal in electrochemical noise data. *Electrochimica Acta*. 2012;70:199–209.
 47. Huang, I. BRG. Uniform corrosion dependence on temperature and pH of Aluminum alloys 2024-T3. *ECS Transactions*. 2015;66(17):97–107.
 48. Karlík M, Slámová M, Janeček M, Homola P. Microstructure evolution of Twin-roll cast Al-Mg alloys during downstream processing. *Kovove Materialy*. 2002;40(5):330–40.
 49. Ambat R, Davenport AJ, Scamans GM, Afseth A. Effect of iron-containing intermetallic particles on the corrosion behaviour of aluminium. *Corrosion Science*. 2006;48(11):3455–71.
 50. Nişancioğlu K. Electrochemical behavior of Aluminum-base intermetallics containing Iron. *Journal of The Electrochemical Society*. 1990;137(1):69.
 51. Aziz, P.M., Godard HP. Pitting corrosion characteristics of Aluminum. *Corrosion*. 1954;(10):269–72.
 52. Garcia-Garcia FJ, Skeldon P, Thompson GE, Smith GC. The effect of nickel on alloy microstructure and electrochemical behaviour of AA1050 aluminium alloy in acid and alkaline solutions. *Electrochimica Acta*. 2012;75:229–38.
 53. Amin MA, Abd El Rehim SS, El-Lithy AS. Pitting and pitting control of Al in gluconic acid solutions - Polarization, chronoamperometry and morphological studies. *Corrosion Science*. 2010;52(9):3099–108.
 54. Øvari F, Tomcsányi L, Túrmezey T. Electrochemical study of the pitting corrosion of aluminium and its alloys-I. Determination of critical pitting and protection potentials.

- Electrochimica Acta*. 1988 Mar;33(3):323–6.
55. Yasuda M. Pitting corrosion of Al and Al-Cu single crystals. *Journal of The Electrochemical Society*. 1990;137(12):3708.
 56. ASTM G61-86 Standard test method for conducting cyclic potentiodynamic polarization measurements to determine the corrosion susceptibility of small implant. [cited 2019 2 March]. p. 1–9. Available from: <https://www.astm.org/Standards/F2129.htm>
 57. Kelly RG, Scully JR, Shoesmith D, Buchheit RG. *Electrochemical techniques in corrosion science and engineering*. New York: Marcel Dekker, Inc.; 2002.
 58. Pride ST. Metastable pitting of Aluminum and criteria for the transition to stable pit growth. *Journal of The Electrochemical Society*. 1994;141(11):3028.
 59. Gabrielli C, Huet F, Keddam M, Oltra R. A review of the probabilistic aspects of localized corrosion. *Corrosion*. 1990;46(4):266–78.
 60. Shibata T, Takeyama T. Stochastic theory of pitting corrosion. *Corrosion-NACE*. 1977;33(7):243–51.
 61. Böhni H, Uhlig HH. Environmental factors affecting the critical pitting potential of Aluminum. *Journal of The Electrochemical Society*. 2007;116(7):906.
 62. Zaid B, Saidi D, Benzaid A, Hadji S. Effects of pH and chloride concentration on pitting corrosion of AA6061 aluminum alloy. *Corrosion Science*. 2008;50(7):1841–7.
 63. Thompson NG, Syrett BC. Relationship between conventional pitting and protection potentials and a new, unique pitting potential. *Corrosion*. 1992;48(8):649–59.
 64. Williams DE, Westcott C, Fleischmann M. Stochastic models of pitting corrosion of Stainless Steels. *Journal of electrochemical Society*. 1985;132(8):1796–804.
 65. Williams DE, Stewart J, Balkwill PH. The nucleation, growth and stability of micropits in Stainless Steel. *Corrosion Science*. 1994;36(7):1213–35.
 66. Pride, S. T., Scully, J. R., Hudson JL. Cooperative stochastic behavior in localized

- corrosion. *Journal of The Electrochemical Society*. 1997;144(5):1620.
67. Gupta RK, Sukiman NL, Cavanaugh MK, Hinton BRW, Hutchinson CR, Birbilis N. Metastable pitting characteristics of aluminium alloys measured using current transients during potentiostatic polarisation. *Electrochimica Acta*. 2012;66:245–54.
 68. Gupta RK, Hinton BRW, Birbilis N. The effect of chromate on the pitting susceptibility of AA7075-T651 studied using potentiostatic transients. *Corrosion Science*. 2014;82:197–207.
 69. Cavanaugh MK, Birbilis N, Buchheit RG. Modeling pit initiation rate as a function of environment for Aluminum alloy 7075-T651. *Electrochimica Acta*. 2012;59:336–45.
 70. Trueman AR. Determining the probability of stable pit initiation on Aluminium alloys using potentiostatic electrochemical measurements. *Corrosion Science*. 2005;47(9):2240–56.
 71. Ralston KD, Birbilis N, Weyland M, Hutchinson CR. The effect of precipitate size on the yield strength-pitting corrosion correlation in Al-Cu-Mg alloys. *Acta Materialia*. 2010;58(18):5941–8.
 72. Uruchurtu JC, Dawson JL. Noise analysis of pure Aluminum under different pitting conditions. *Corrosion*. 1987;43(1):19–26.
 73. Curioni M, Cottis RA, Thompson GE. Application of electrochemical noise analysis to corroding aluminium alloys. *Surface and Interface Analysis*. 2013;45(10):1564–9.
 74. Homborg AM, Van Westing EPM, Tinga T, Ferrari GM, Zhang X, De Wit JHW, Mol JMC. Application of transient analysis using Hilbert spectra of electrochemical noise to the identification of corrosion inhibition. *Electrochimica Acta*. 2014;116:355–65.
 75. Acosta G, Veleza L, Lopez JL. Power spectral density analysis of the corrosion potential fluctuation of aluminium in early stages of exposure to caribbean sea water. *International Journal of Electrochemical Science*. 2014;9(11):6464–74.
 76. Searson PC, Dawson JL. Analysis of electrochemical noise generated by corroding electrodes under open-circuit conditions. *Journal of The Electrochemical Society*.

- 1988;135(8):1908.
77. Homborg AM, Tinga T, Van Westing EPM, Zhang X, Ferrari GM, De Wit JHW, Mol JMC. A critical appraisal of the interpretation of electrochemical noise for corrosion studies. *Corrosion*. 2014;70(10):971–87.
 78. Cottis RA. Interpretation of electrochemical noise data. *Corrosion*. 2001;57(3):265–84.
 79. Francois Huet. PSD Calculation. [cited 2018 20 November]. Available from: <http://www.s440691671.websitehome.co.uk/guideline/PSDcalculator.html>
 80. Zhang T, Shao Y, Meng G, Wang F. Electrochemical noise analysis of the corrosion of AZ91D magnesium alloy in alkaline chloride solution. *Electrochimica Acta*. 2007;53(2):561–8.
 81. Lafront AM, Safizadeh F, Ghali E, Houlachi G. Study of the copper anode passivation by electrochemical noise analysis using spectral and wavelet transforms. *Electrochimica Acta*. 2010;55(7):2505–12.
 82. Cai C, Zhang Z, Cao F, Gao Z, Zhang J, Cao C. Analysis of pitting corrosion behavior of pure Al in sodium chloride solution with the wavelet technique. *Journal of Electroanalytical Chemistry*. 2005;578(1):143–50.
 83. Nisancoglu K. Corrosion of Aluminum alloys. *The 3rd International Conference on Aluminium Alloys*; 1992: ICAA.
 84. Aballe A, Bethencourt M, Botana FJ, Cano MJ, Marcos M. Localized alkaline corrosion of alloy AA5083 in neutral 3.5 percent NaCl solution. *Corrosion Science*. 2001;43(9):1657–74.
 85. Büchler M, Watari T, Smyrl WH. Investigation of the initiation of localized corrosion on aluminum alloys by using fluorescence microscopy. *Corrosion Science*. 2000;42(9):1661–8.
 86. Ilevbare GO, Schneider O, Kelly RG, Scully JR. In situ confocal laser scanning microscopy of AA2024-T3 corrosion metrology. *Journal of The Electrochemical Society*. 2004;151(8):B453.

87. Sukiman NL, Shi H, Gupta RK, Buchheit RG, Birbilis N. Electrochemical and corrosion response of commercially pure Aluminum alloyed with binary additions of strontium. *Journal of the Electrochemical Society*. 2013;160(8):C299–304.
88. Wang Y, Gupta RK, Sukiman NL, Zhang R, Davies CHJ, Birbilis N. Influence of alloyed Nd content on the corrosion of an Al-5Mg alloy. *Corrosion Science*. 2013;73:181–7.



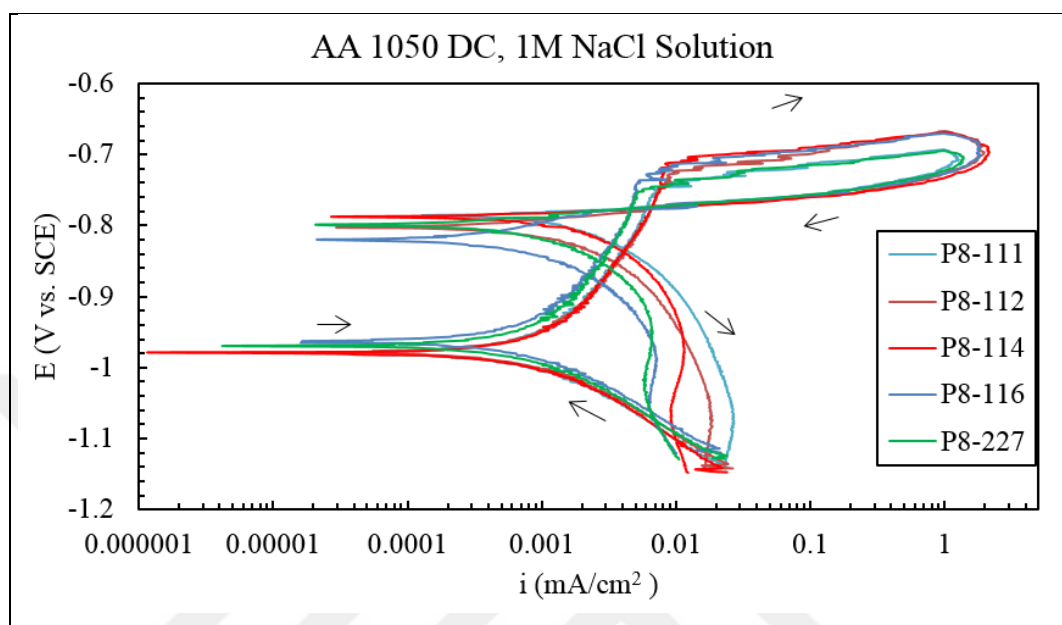
APPENDIX A: RESULTS OF CPP MEASUREMENTS

Figure A.1. Cyclic polarization measurement results for AA1050 DC in 1M NaCl solution. The arrows show the sweep direction.

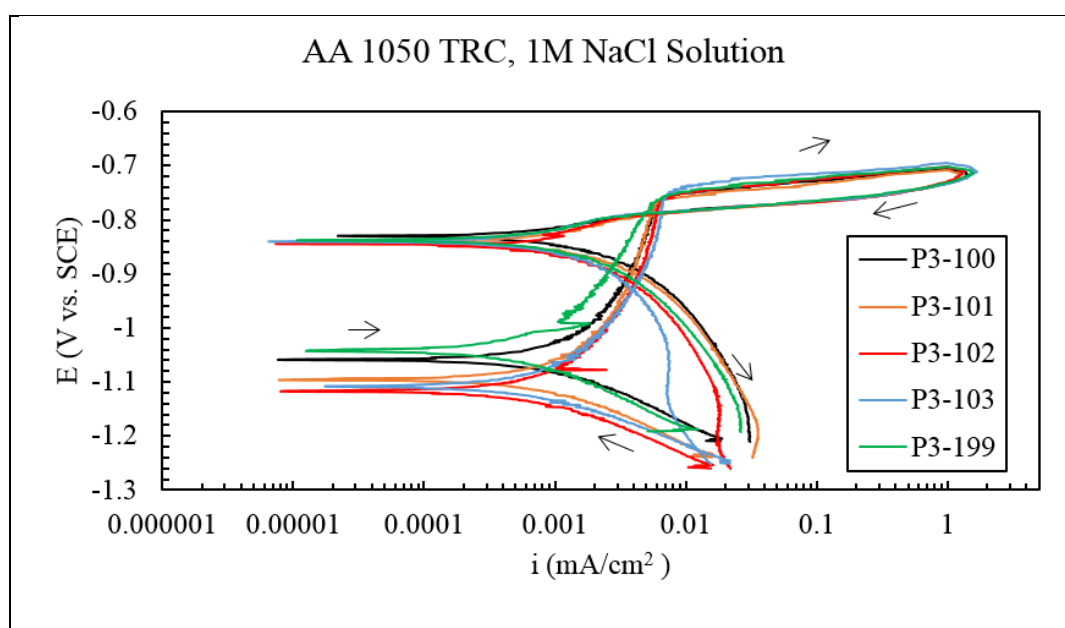


Figure A.2. Cyclic polarization measurement results for AA1050 TRC in 1M NaCl solution. The arrows show the sweep direction.

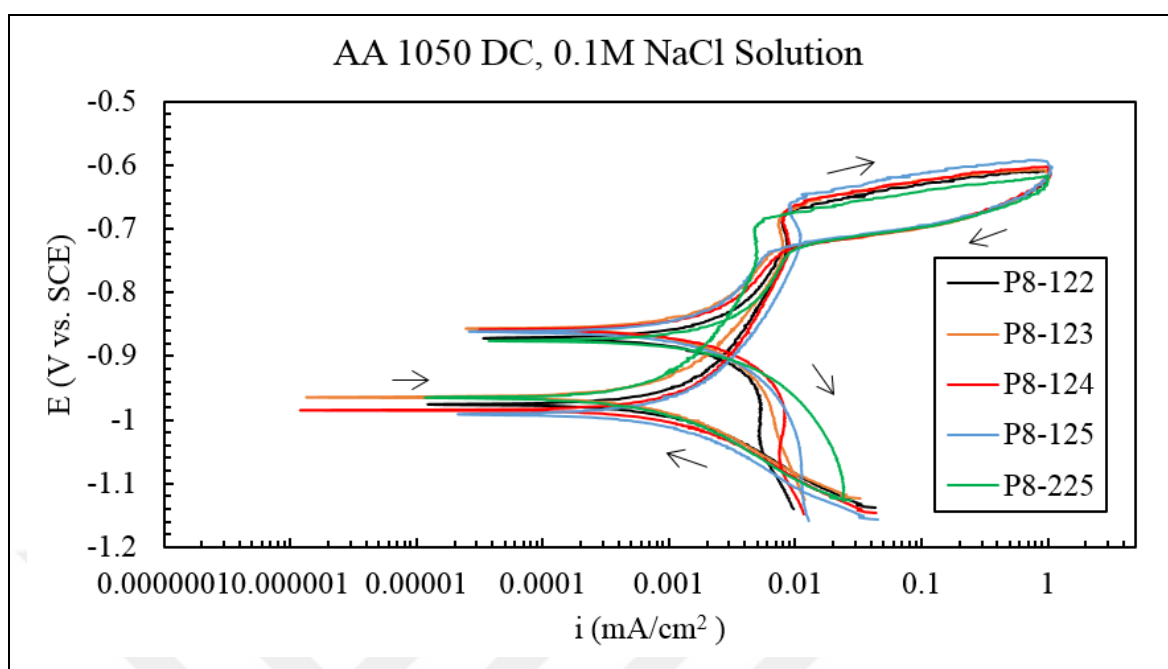


Figure A.3. Cyclic polarization measurement results for AA1050 DC in 0.1M NaCl solution. The arrows show the sweep direction.

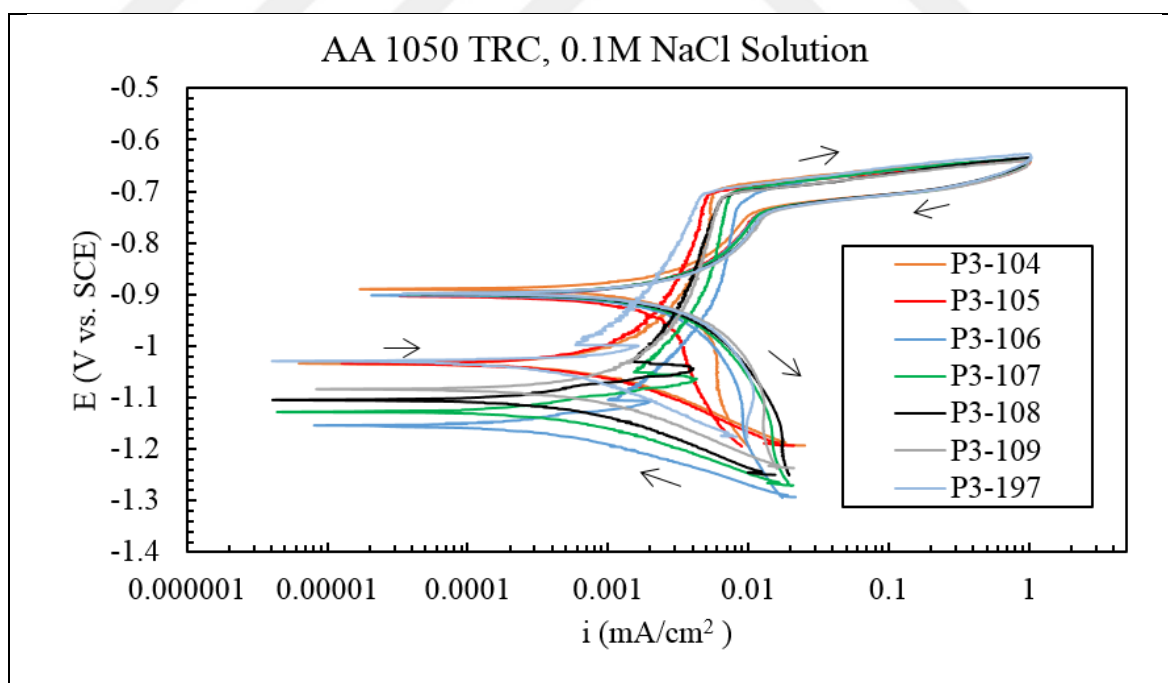


Figure A.4. Cyclic polarization measurement results for AA1050 TRC in 0.1M NaCl solution. The arrows show the sweep direction.

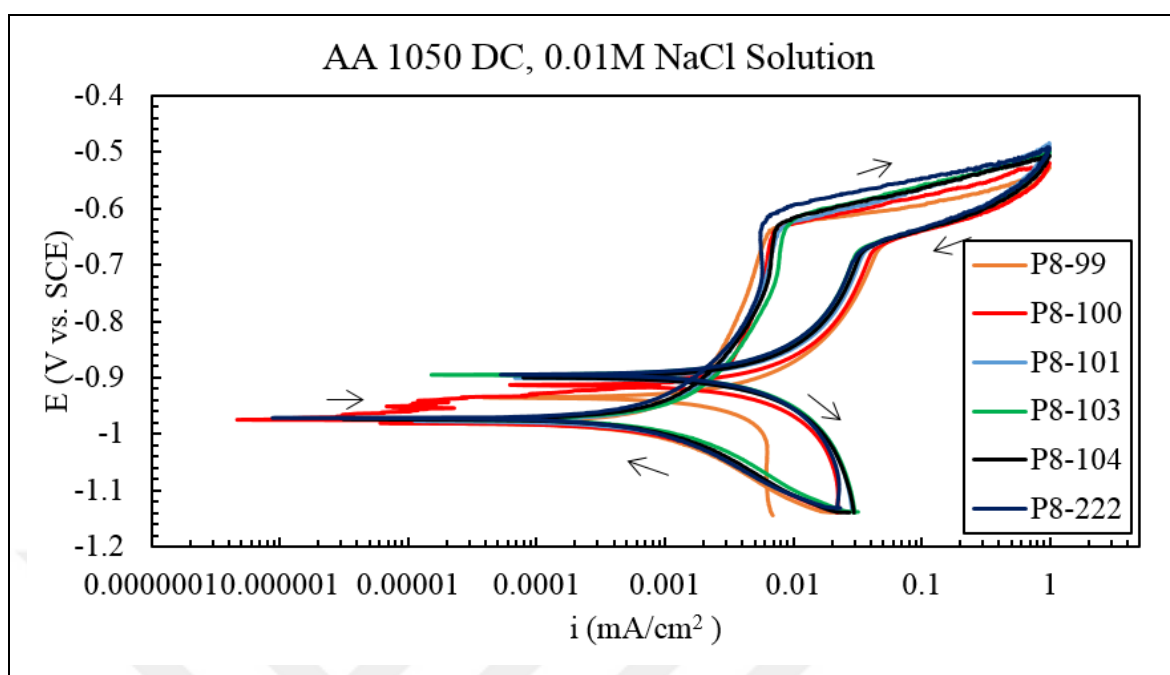


Figure A.5. Cyclic polarization measurement results for AA1050 DC in 0.01M NaCl solution. The arrows show the sweep direction.

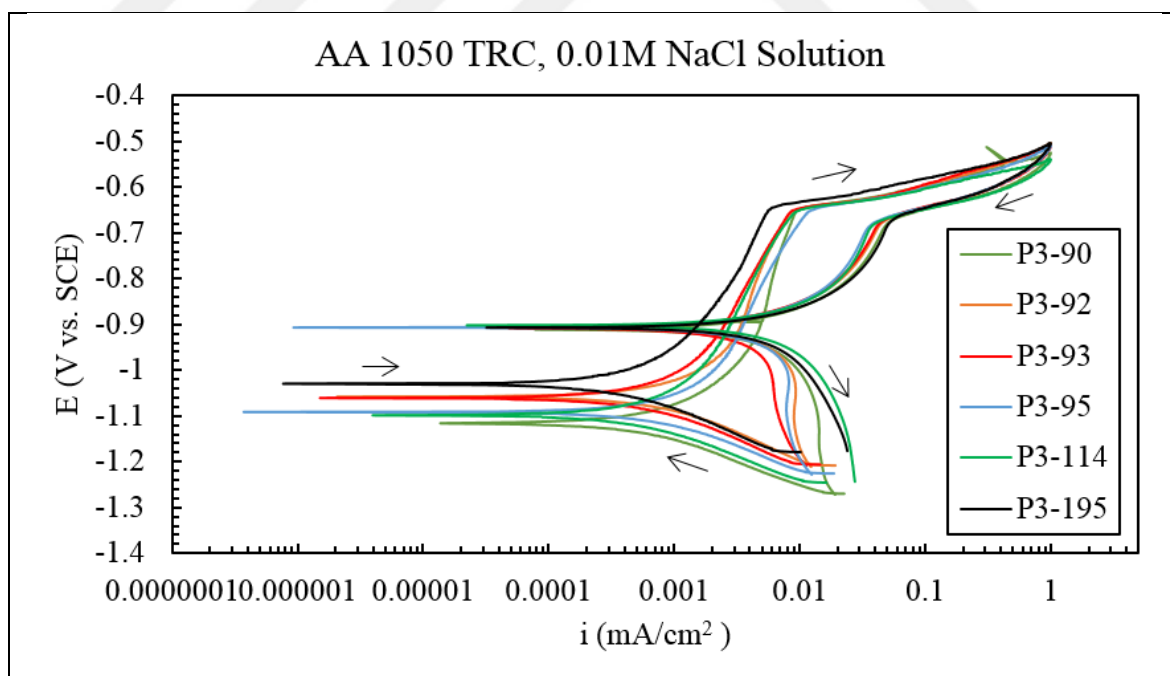


Figure A.6. Cyclic polarization measurement results for AA1050 TRC in 0.01M NaCl solution. The arrows show the sweep direction.

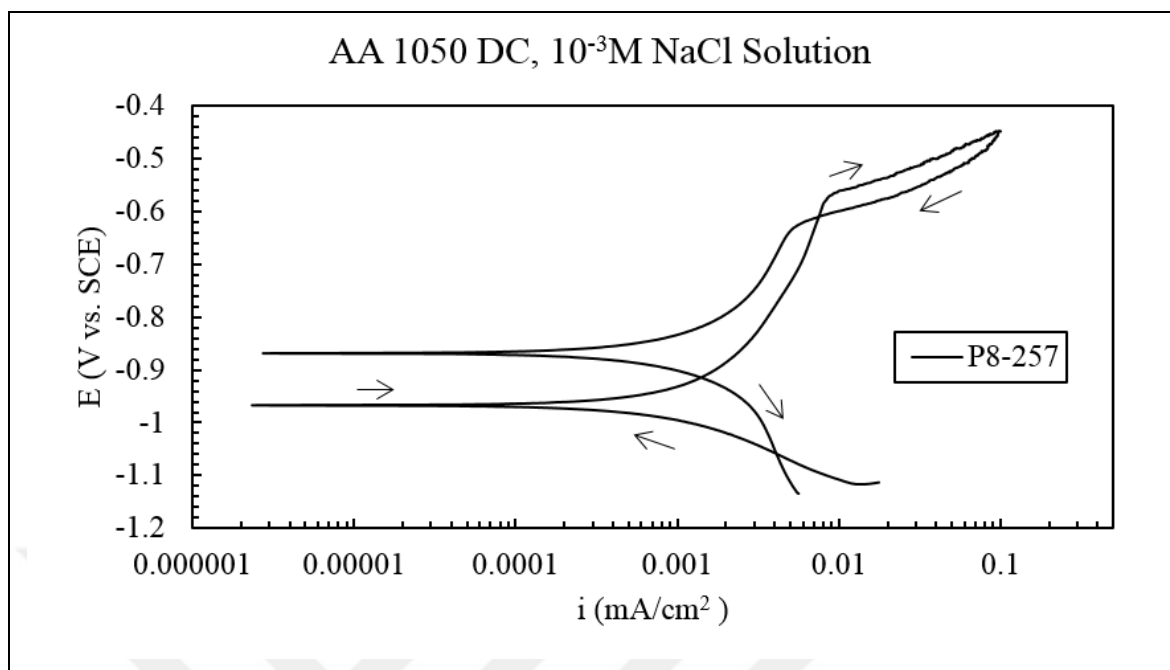


Figure A.7. Cyclic polarization measurement results for AA1050 DC in 0.001M NaCl solution. The arrows show the sweep direction.

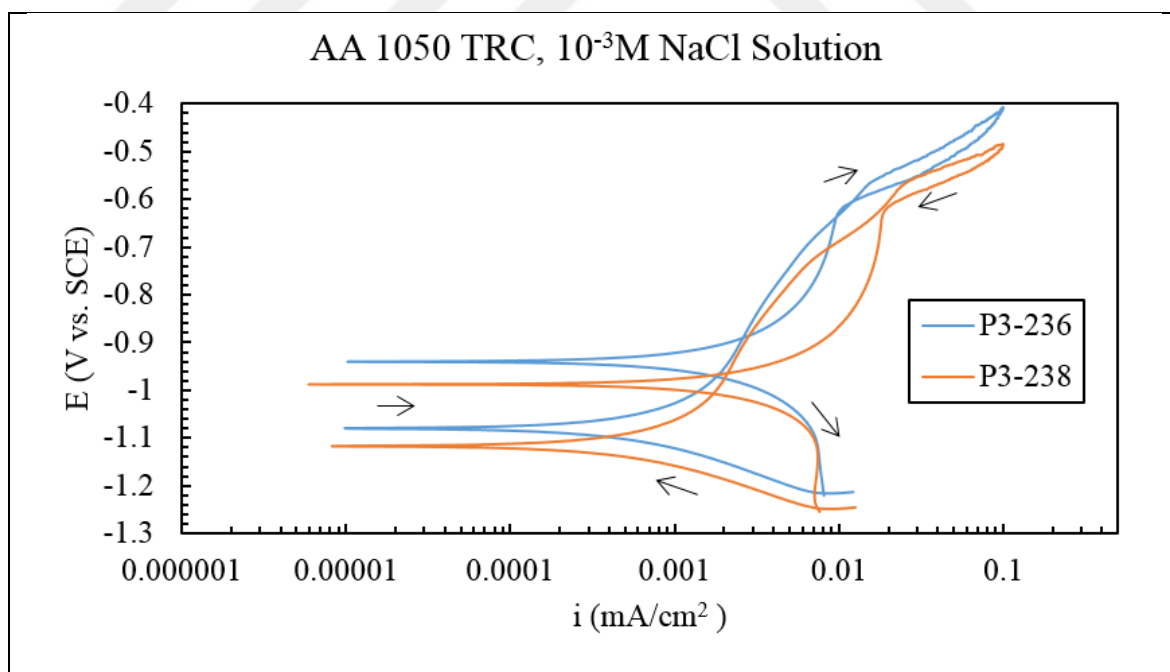
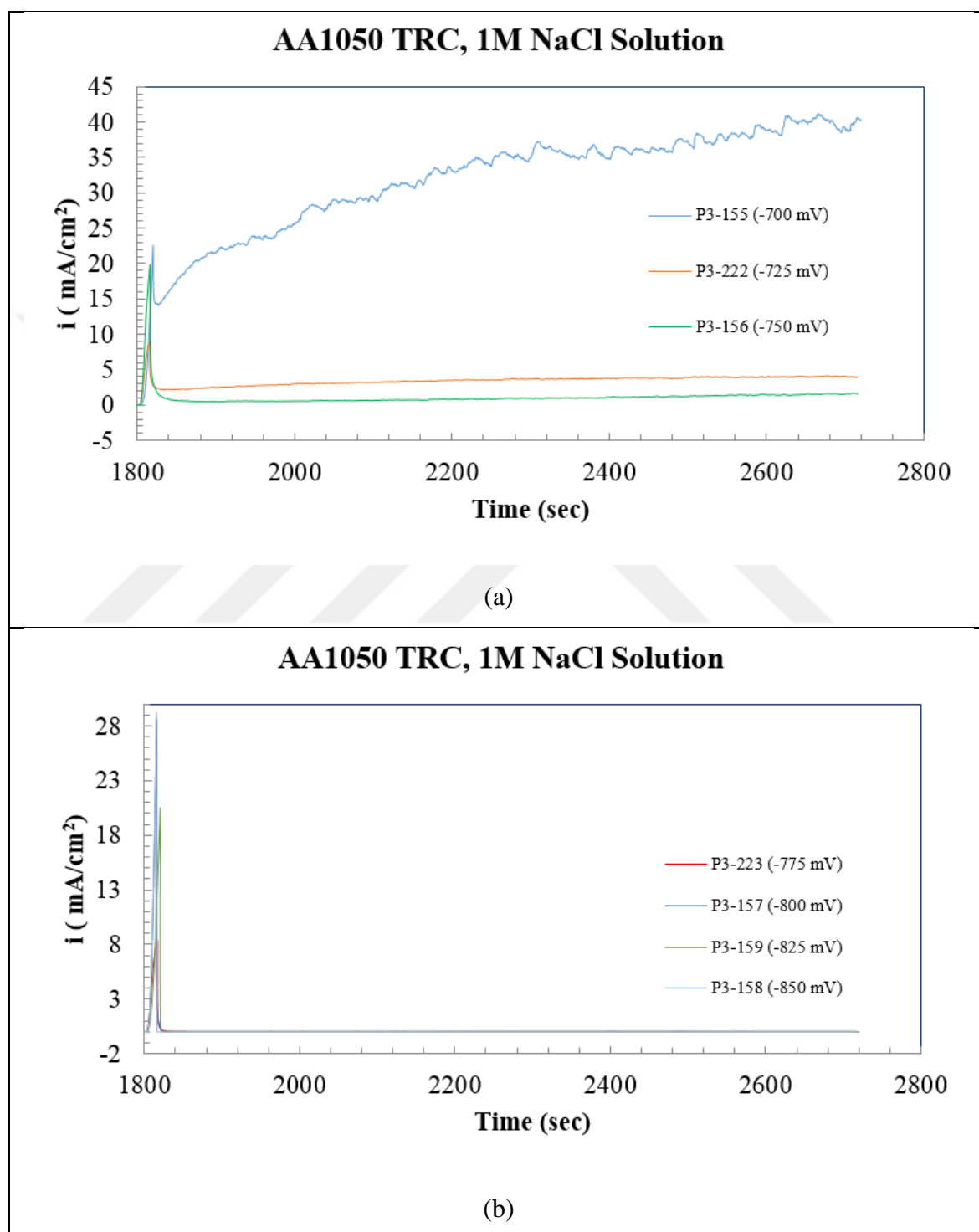


Figure A.8. Cyclic polarization measurement results for AA1050 TRC in 0.001M NaCl solution. The arrows show the sweep direction

APPENDIX B: RESULTS OF E_{repas} MEASUREMENT

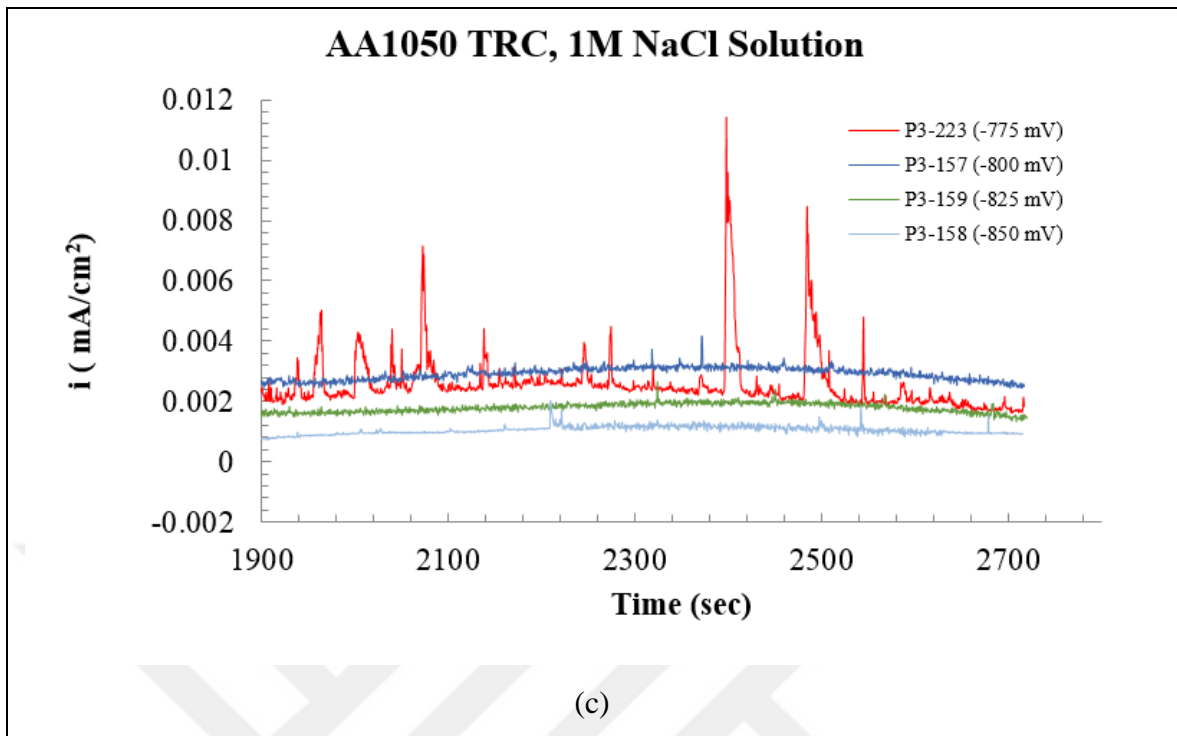
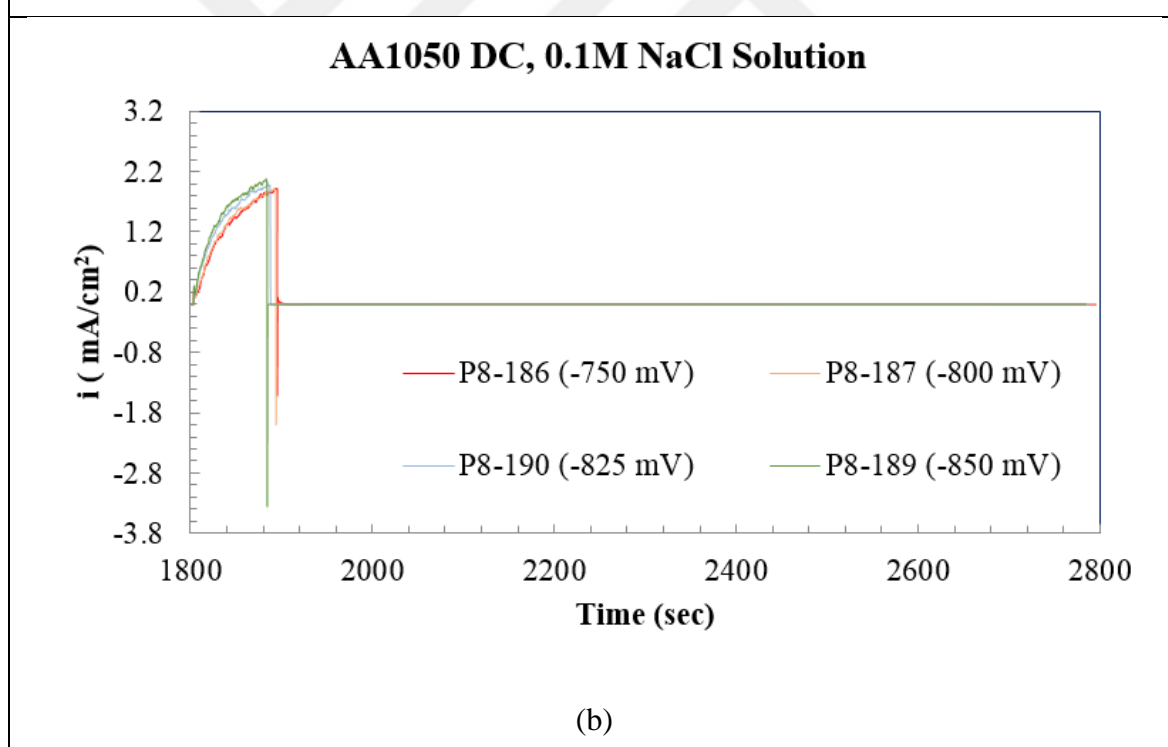
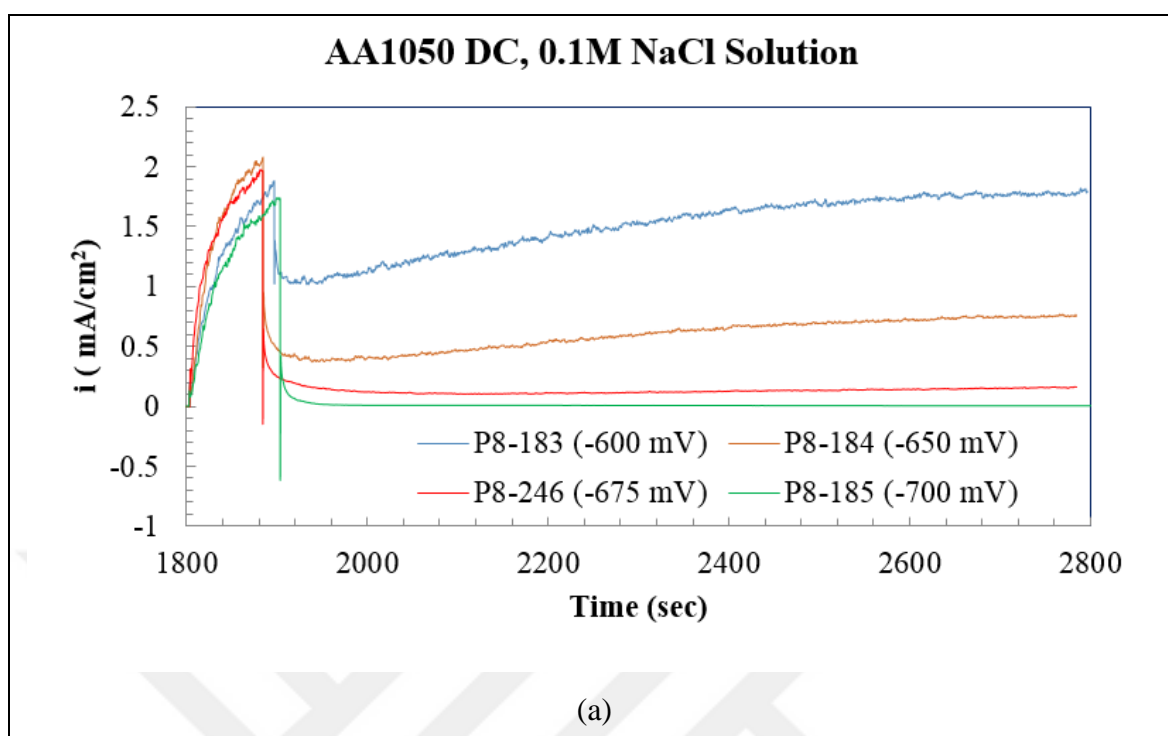


Figure B.1. Potentio-static repassivation potential graph for AA1050 TRC alloys in 1 M NaCl solution for between (a) -700 and -750 m, (b) between -775 and -850 mV and (c) magnified graph for between -775 and -850 mV potentials



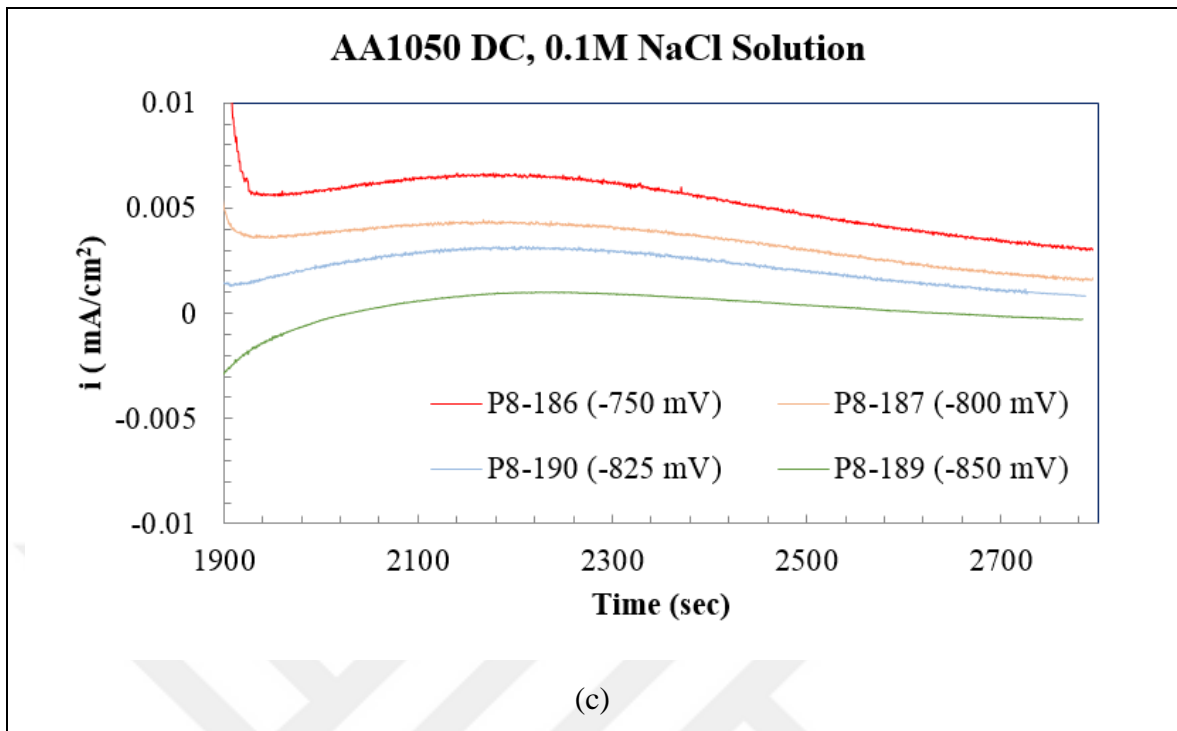
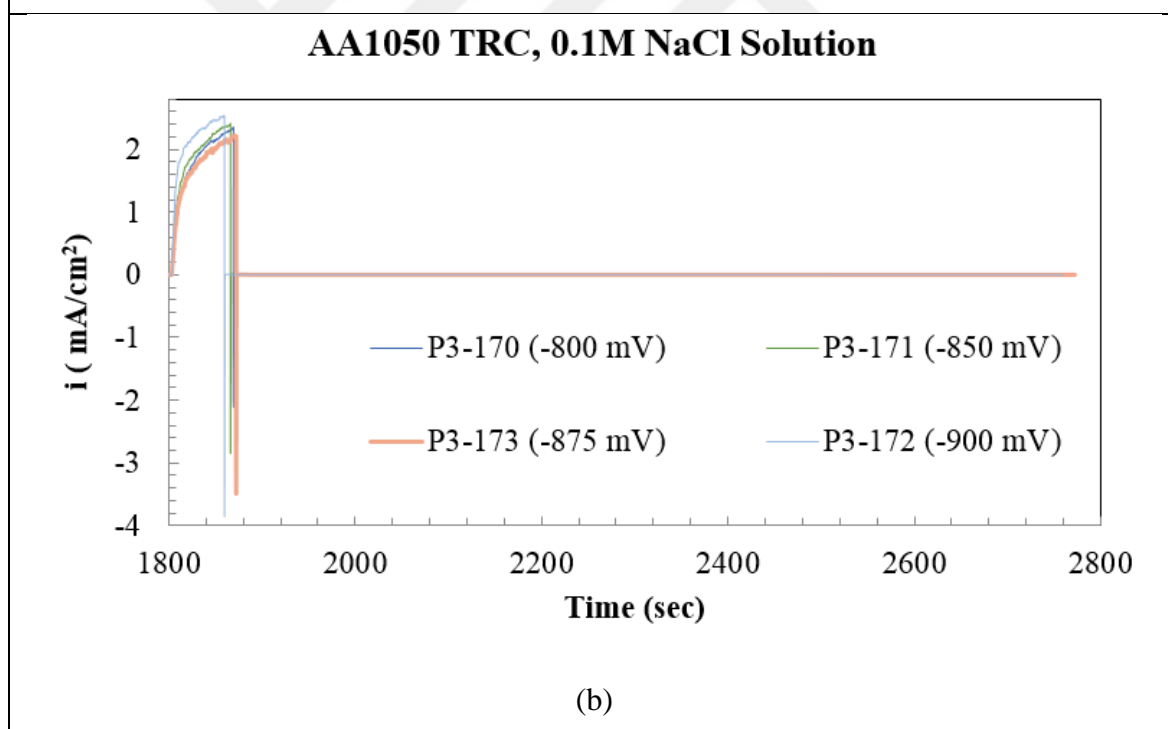
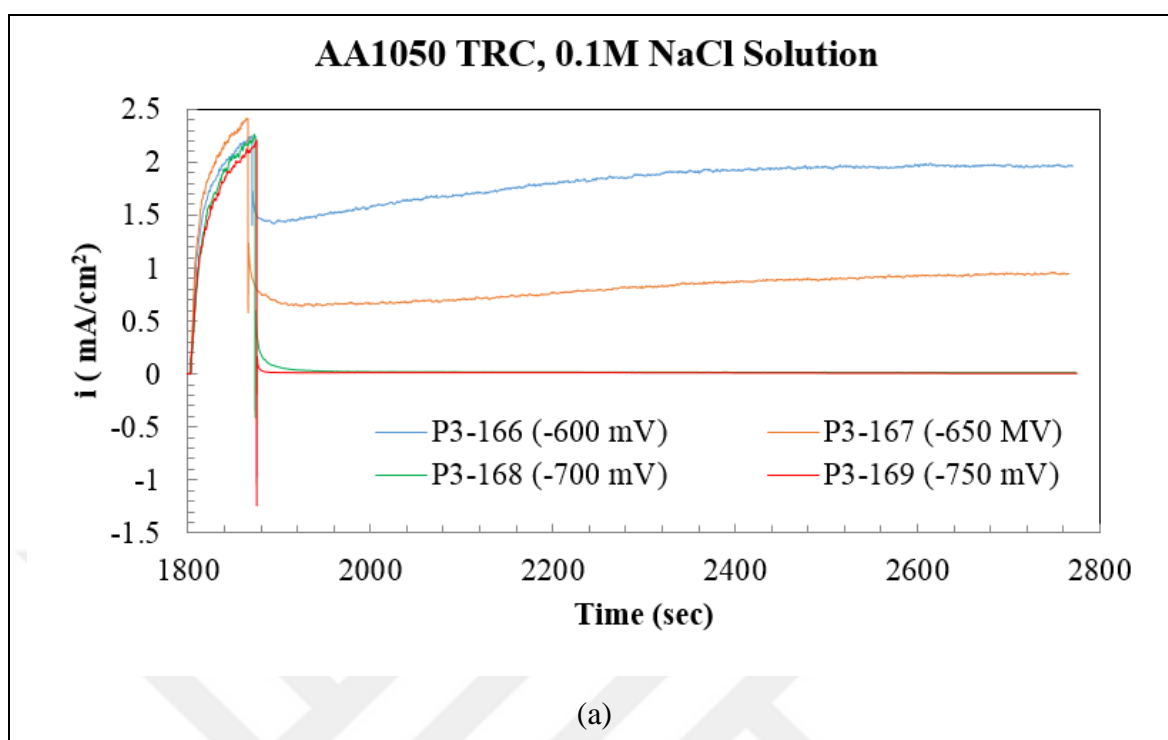


Figure B.2. Potentio-static repassivation potential graph for AA1050 DC alloys in 0.1 M NaCl solution for between (a) -600 and -700 mV, (b) between -750 and -850 mV and (c) magnified graph for between -750 and -850 mV potentials



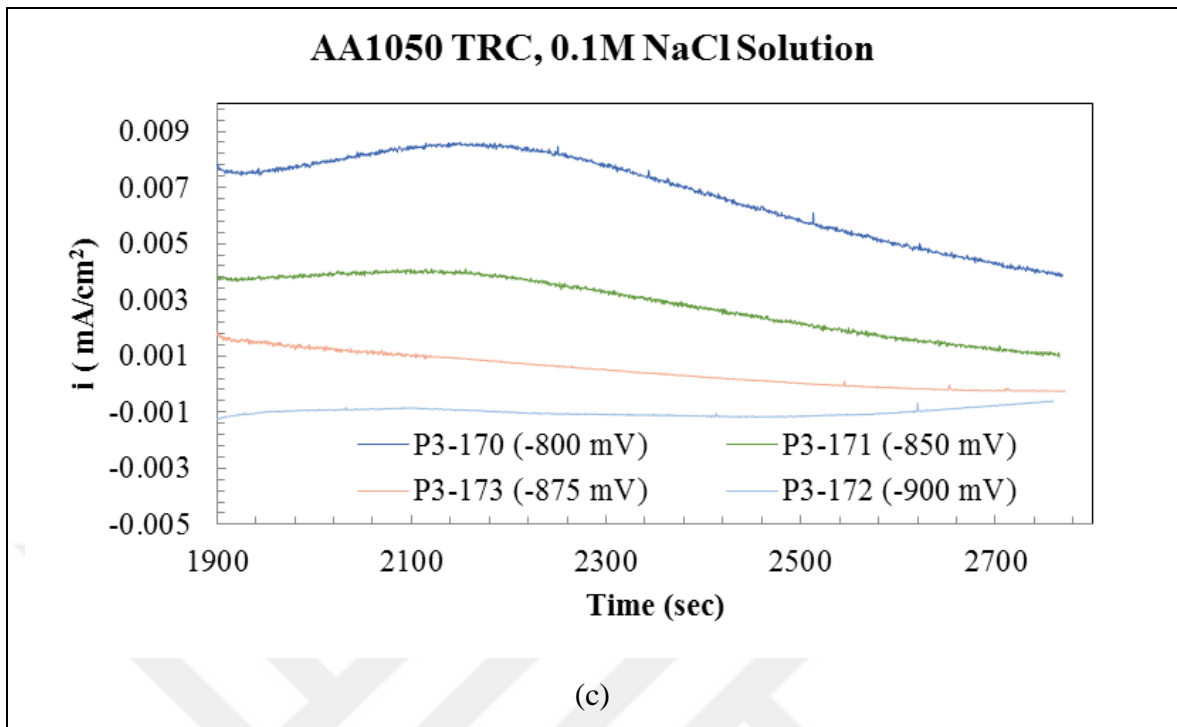
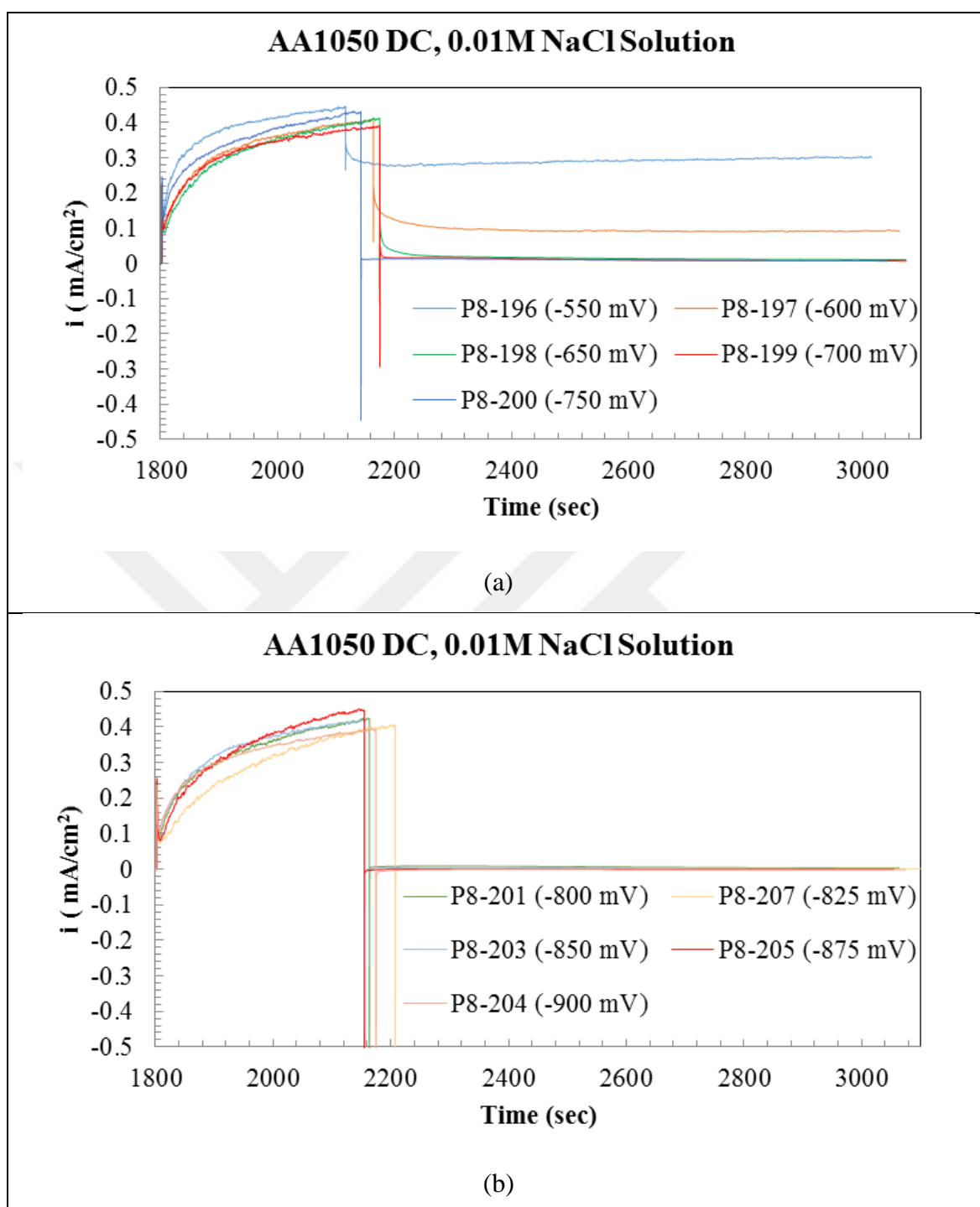


Figure B.3. Potentio-static repassivation potential graph for AA1050 TRC alloys in 0.1 M NaCl solution for between (a) -600 and -750 mV, (b) between -800 and -900 mV and (c) magnified graph for between -800 and -900 mV potentials



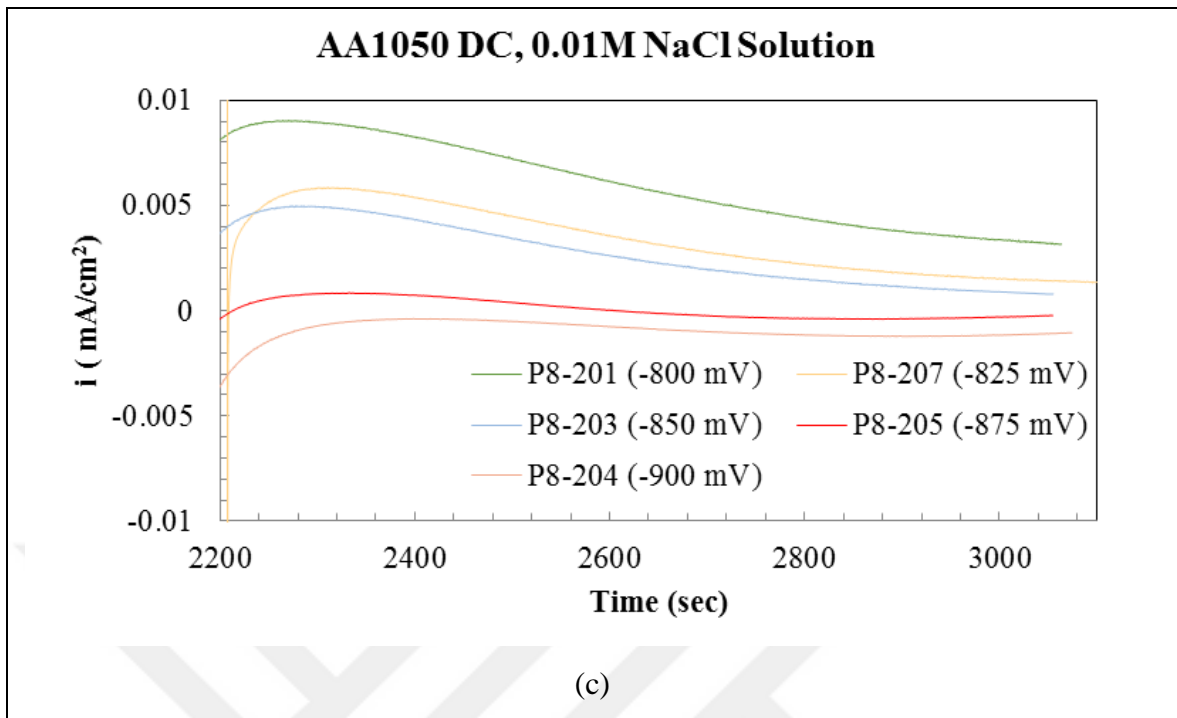
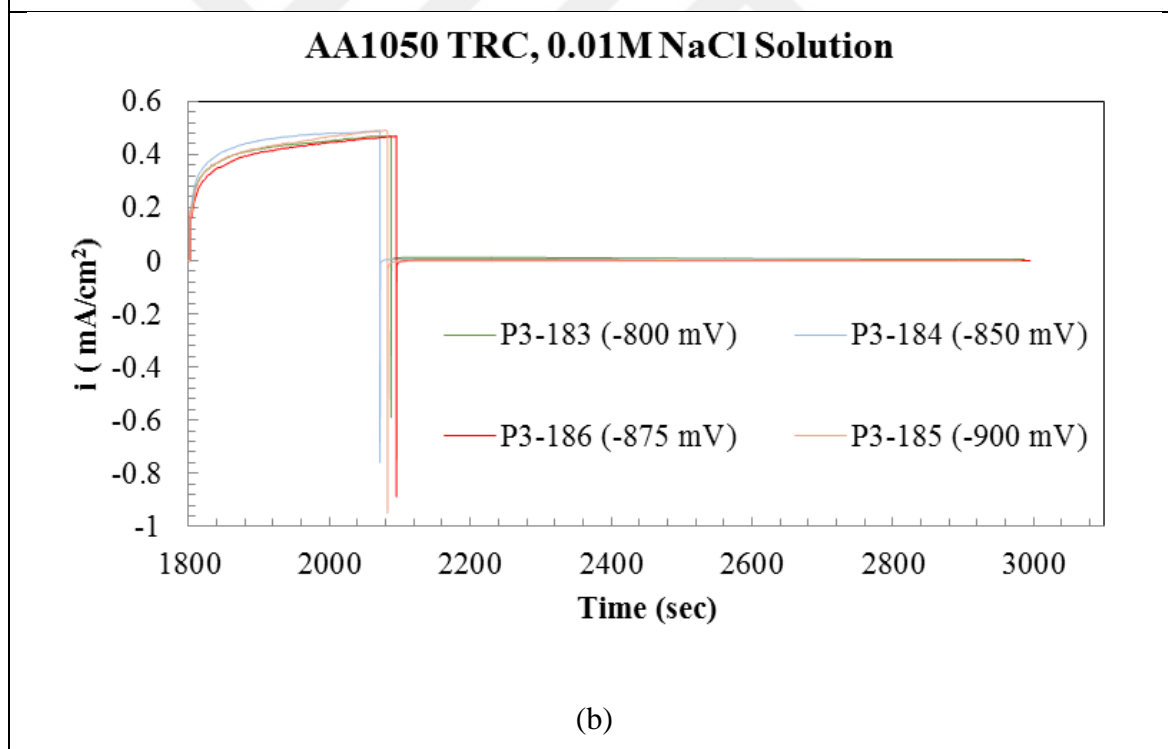
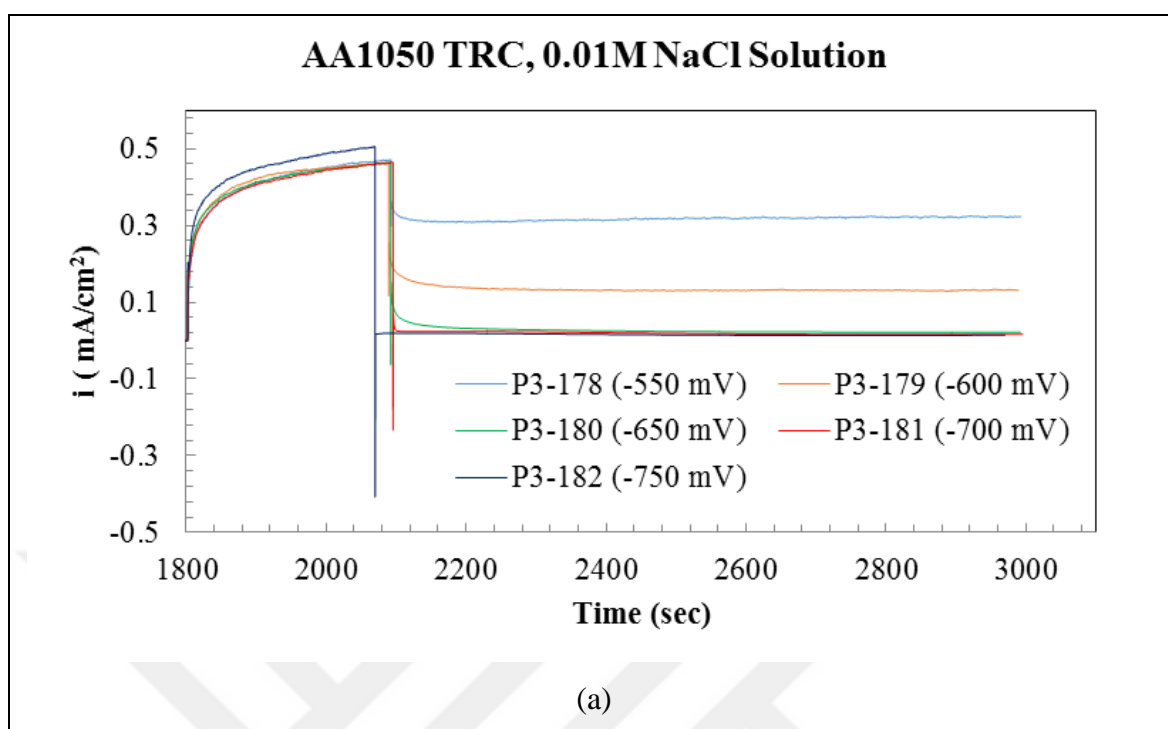


Figure B.4. Potentio-static repassivation potential graph for AA1050 DC alloys in 0.01 M NaCl solution for between (a) -550 and -750 mV, (b) between -800 and -900 mV and (c) magnified graph for between -800 and -900 mV potentials



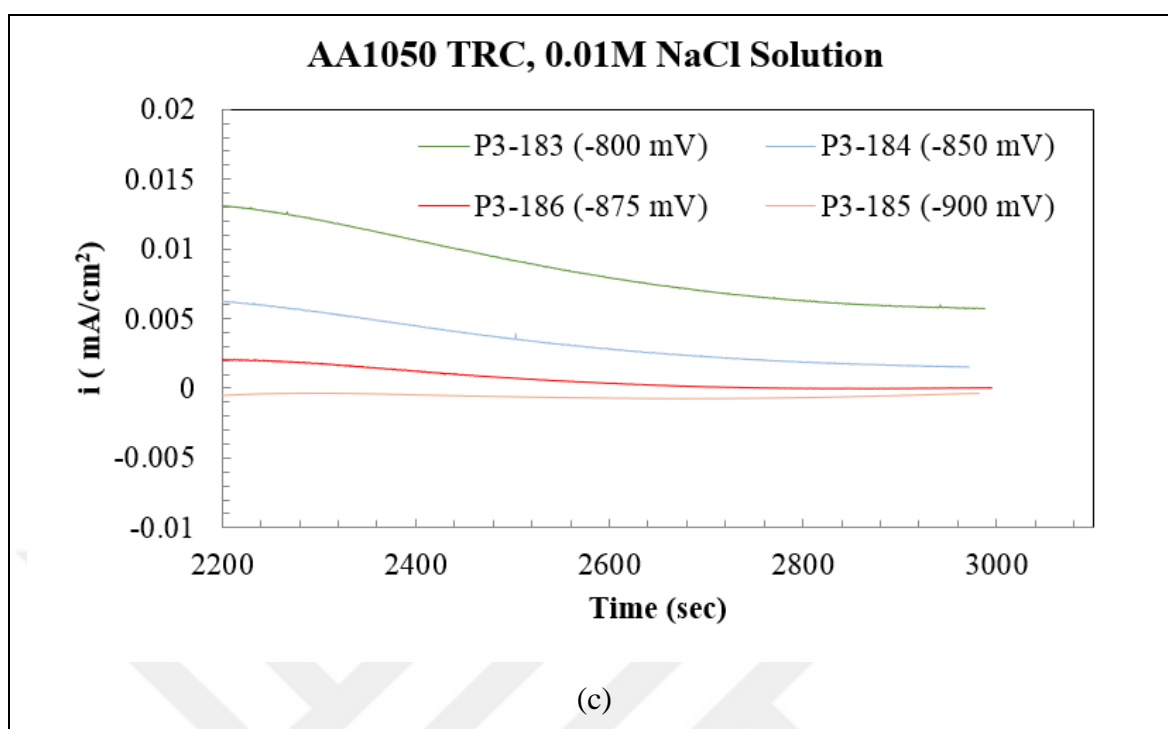


Figure B.5. Potentio-static repassivation potential graph for AA1050 TRC alloys in 0.01 M NaCl solution for between (a) -550 and -750 mV, (b) between -800 and -900 mV and (c) magnified graph for between -800 and -900 mV potentials

APPENDIX C: RESULTS OF GSCP MEASUREMENT

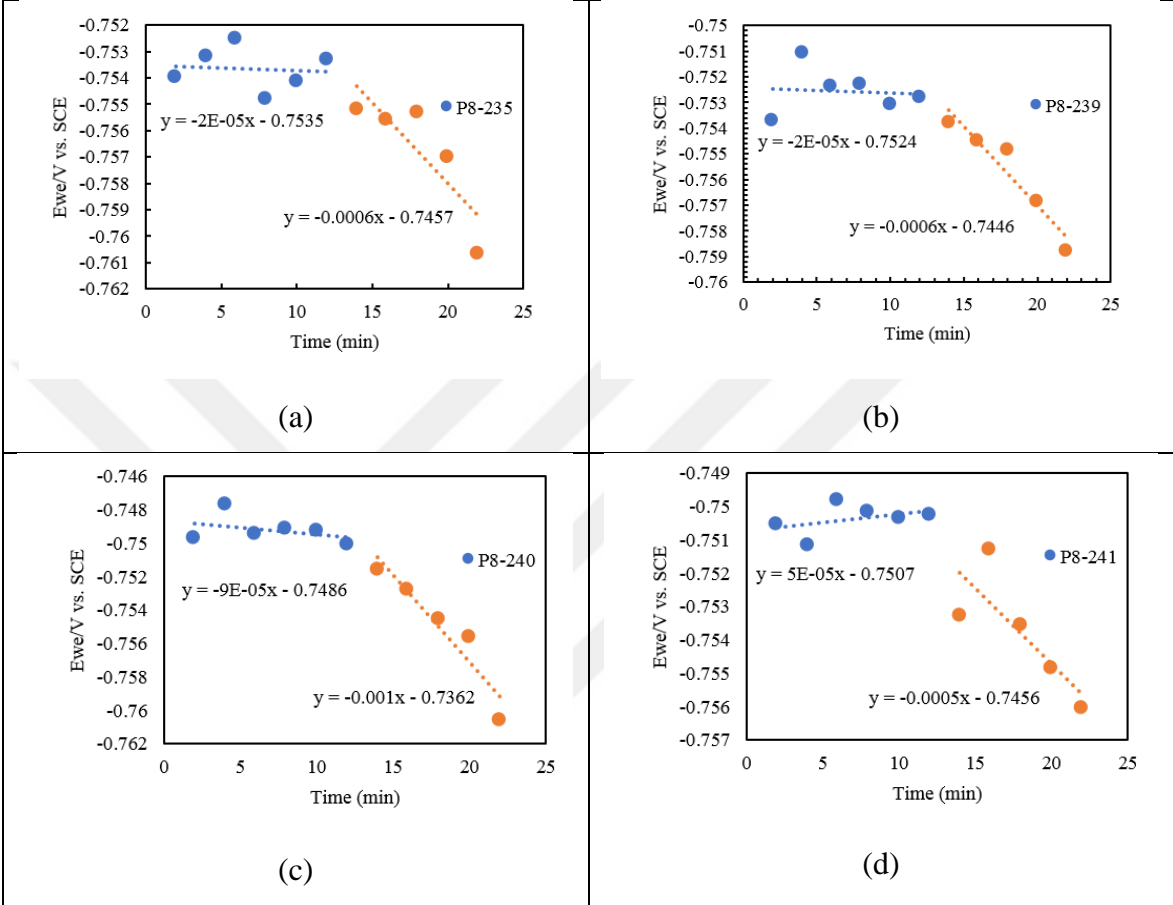


Figure C.1. GSCP result graphs for four different (a to d) 1M DC alloys

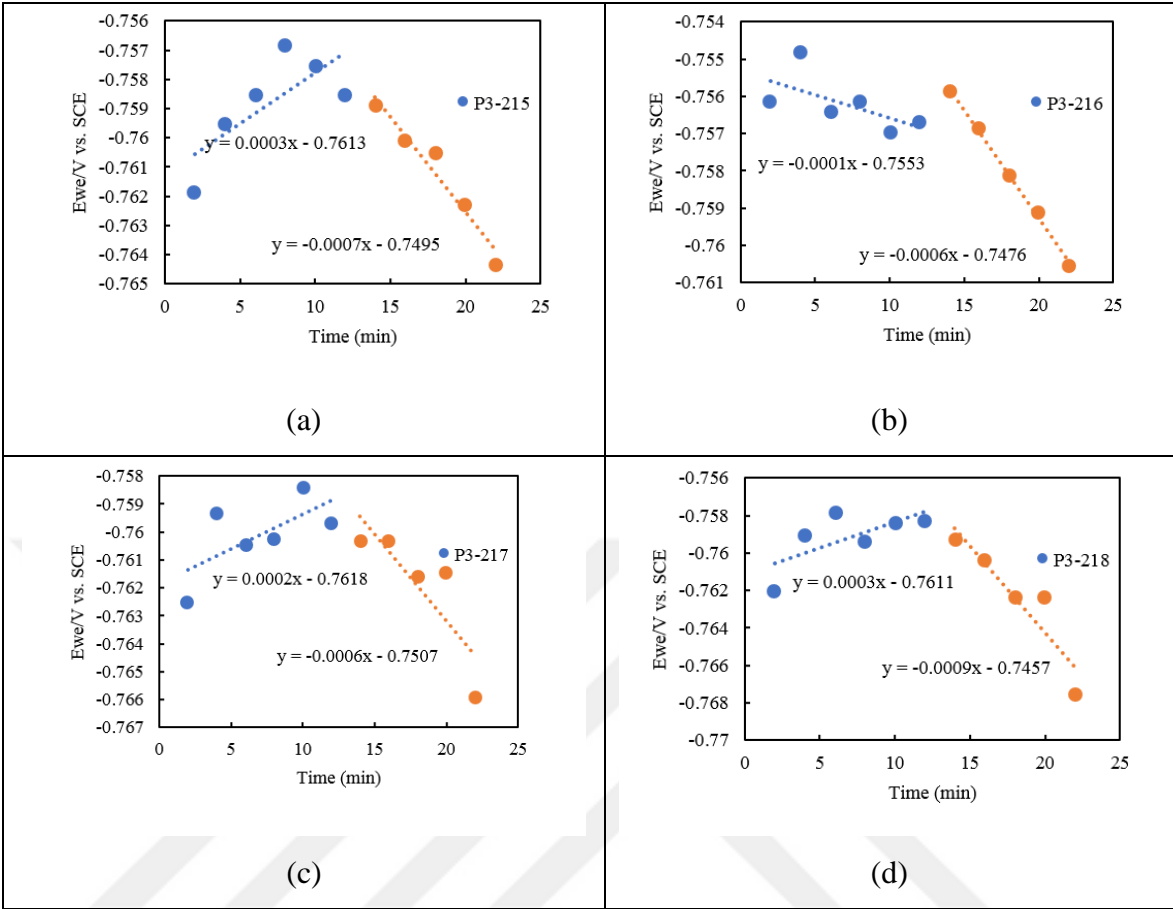


Figure C.2. GSCP result graphs for four different (a to d) 1M TRC alloys

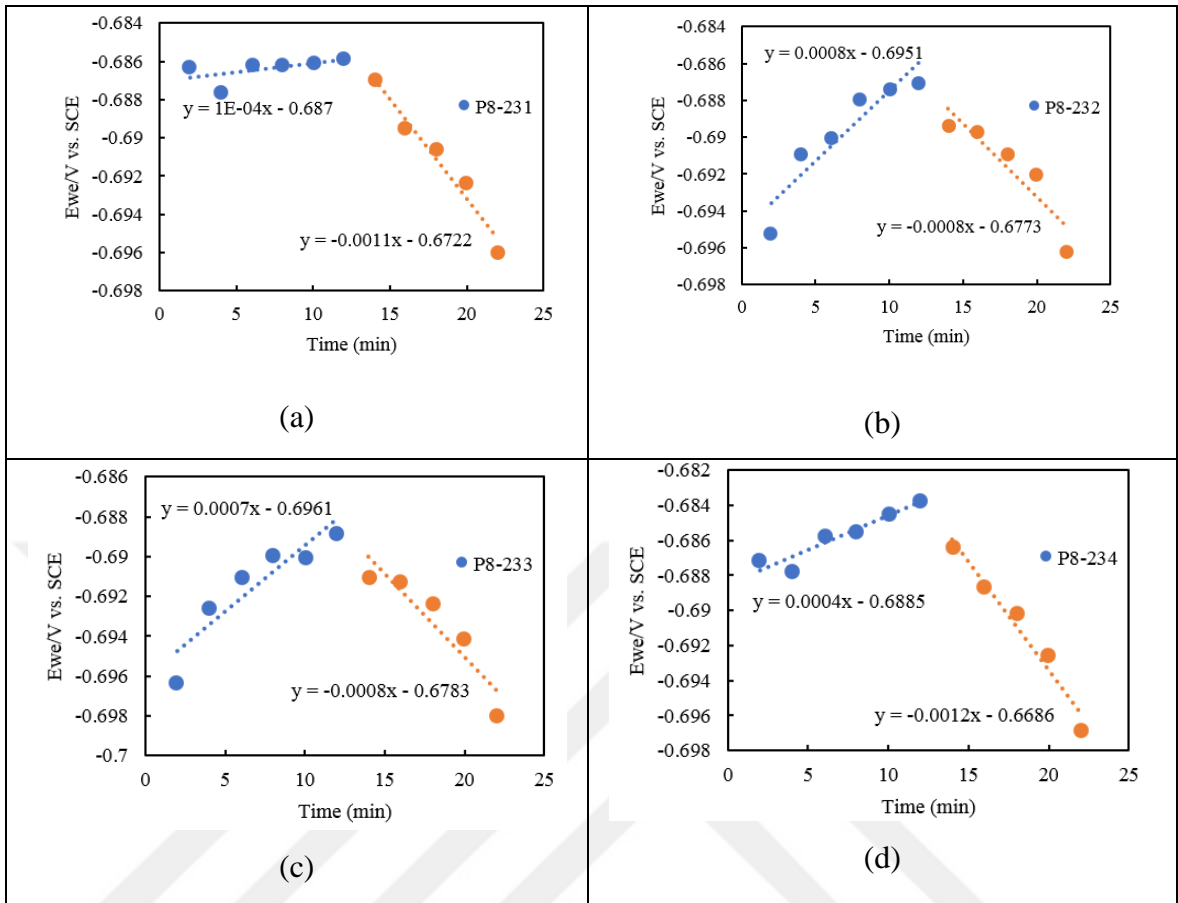


Figure C.3. GSCP result graphs for four different (a to d) 0.1M DC alloys

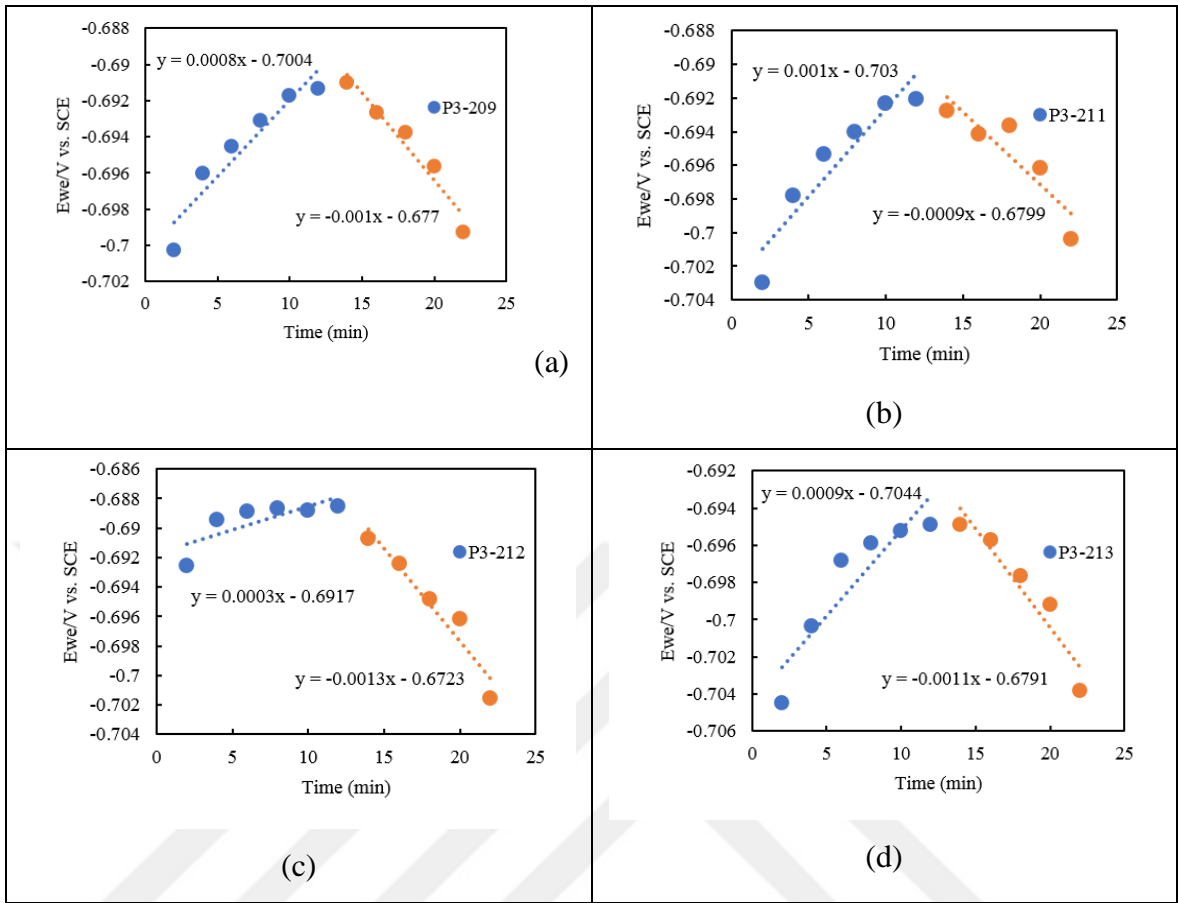


Figure C.4. GSCP result graphs for four different (a to d) 0.1M TRC alloys

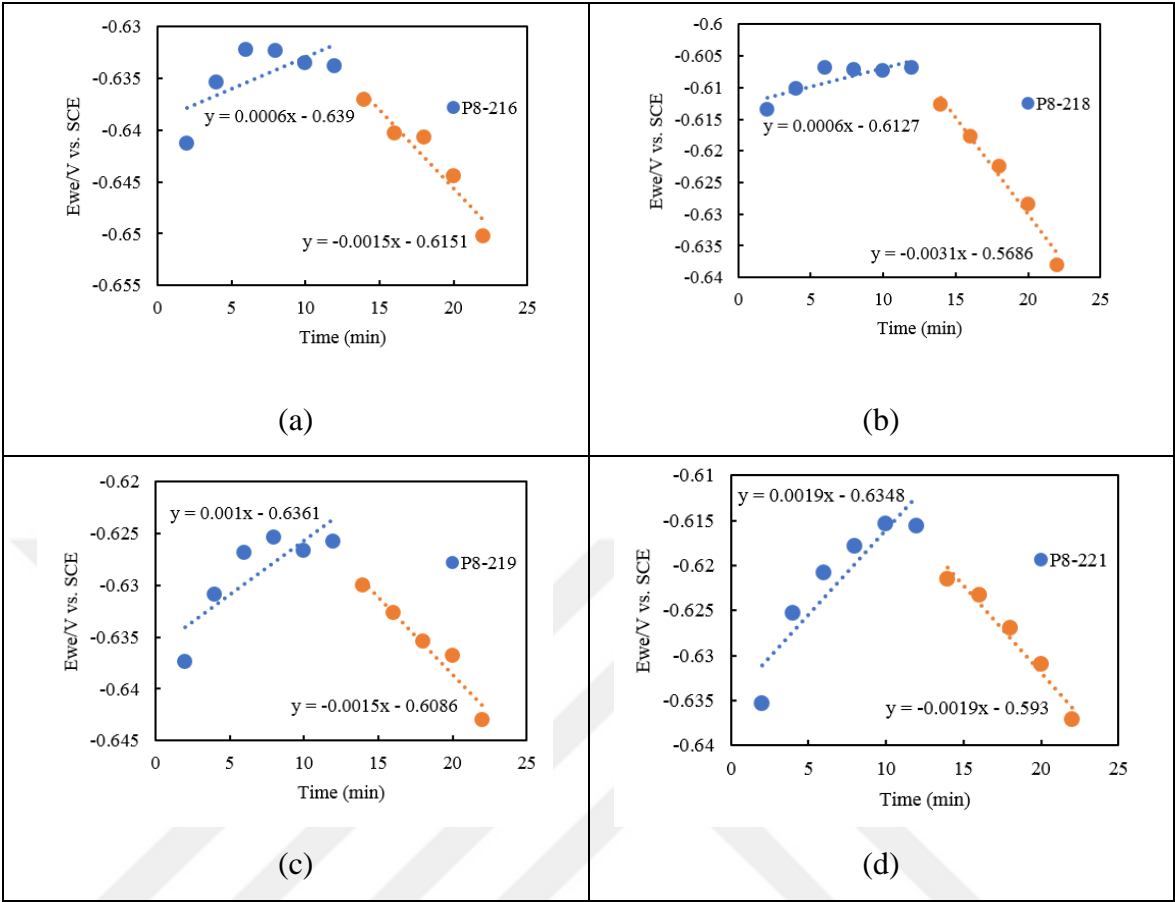


Figure C.5. GSCP result graphs for four different (a to d) 0.01M DC alloys

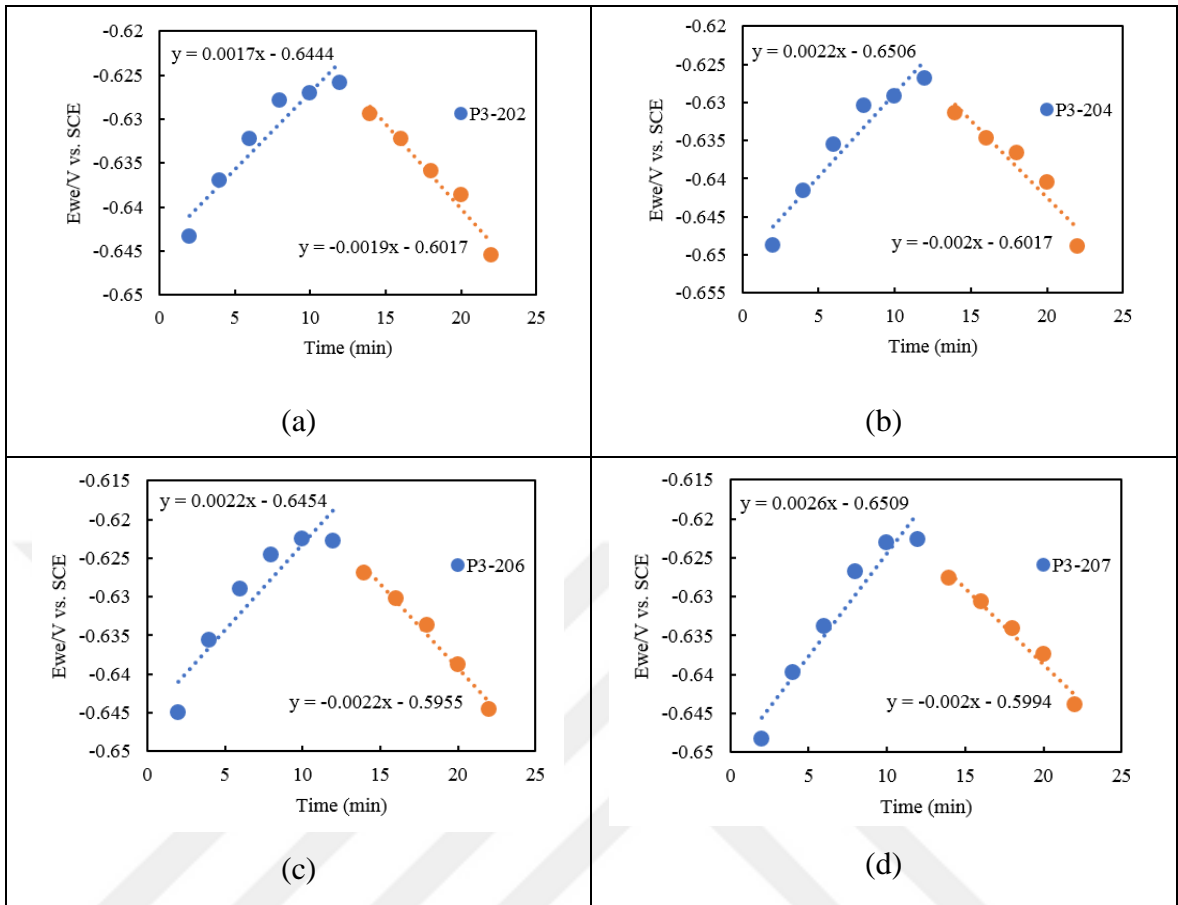


Figure C.6. GSCP result graphs for four different (a to d) 0.01M TRC alloys